A STUDY IN GPS-DENIED NAVIGATION USING SYNTHETIC APERTURE RADAR

by

Colton P. Lindstrom

A thesis submitted in partial fulfillment
of the requirements for the degree

of

MASTER OF SCIENCE

in

Electrical Engineering

Approved:

Randall S. Christensen, Ph.D. Major Professor	Jacob H. Gunther, Ph.D. Committee Member
Charles M. Swenson, Ph.D. Committee Member	D. Richard Cutler, Ph.D. Interim Vice Provost for Graduate Studies

UTAH STATE UNIVERSITY
Logan, Utah

2020

ABSTRACT

A Study in GPS-Denied Navigation Using Synthetic Aperture Radar

by

Colton P. Lindstrom, Master of Science

Utah State University, 2020

Major Professor: Randall S. Christensen, Ph.D.
Department: Electrical and Computer Engineering

GPS denied navigation solves the problem of precisely navigating a vehicle in the absence of a Global Navigation Satellite System such as GPS. Several methods of navigation without GPS have been proposed and studied. The research presented in this thesis furthers the work done in this field by investigating how synthetic aperture radar (SAR) could be used in a GPS denied navigation scenario.

A compilation of three academic papers is presented. Each paper explores an individual aspect of the proposed problem, and the results from each are reported. The results support the use of SAR in GPS denied navigation settings. Derivations, background theory, and validation methods are provided throughout this document.

The major contributions from this research are threefold. First, a system in implemented that synthesizes pseudo range and range rate measurements within an Inertial Navigation System (INS) architecture employing an extended Kalman filter (EKF). The system is tested in a GPS denied navigation setting to test the feasibility of using radar telemetry for navigation. Results suggest that navigation using radar telemetry in A GPS denied setting is feasible and results in converging and bounded navigation estimation errors.

Second, the relationship between navigation errors and SAR imaging errors is explored. Images are formed using the back-projection algorithm. This investigation is motivated by

the potential of inferring navigation errors from blurs and shifts within an improperly formed SAR image. Analytical expressions are derived and verified using both real and simulated navigation and radar data.

Third, a full flight and radar system is developed which investigates navigation from fully formed SAR images using the range-Doppler algorithm. The system is tested using both simulated and real flight and radar data. For both types of data, results show a system that accurately navigates in the absence of GPS with bounded and converging navigation estimation errors. Results for the case of simulated data are validated via Monte Carlo analysis.

(181 pages)

PUBLIC ABSTRACT

A Study in GPS-Denied Navigation Using Synthetic Aperture Radar

Colton P. Lindstrom

In modern navigation systems, GPS is vital to accurately piloting a vehicle. This is especially true in autonomous vehicles, such as UAVs, which have no pilot. Unfortunately, GPS signals can be easily jammed or spoofed. For example, canyons and urban cities create an environment where the sky is obstructed and make GPS signals unreliable. Additionally, hostile individuals can transmit personal signals intended to block or spoof GPS signals. In these situations, it is important to find a means of navigation that doesn't rely on GPS.

Navigating without GPS means that other types of sensors or instruments must be used to replace the information lost from GPS. Some examples of additional sensors include cameras, altimeters, magnetometers, and radar. The work presented in this thesis shows how radar can be used to navigate without GPS. Specifically, synthetic aperture radar (SAR) is used, which is a method of processing radar data to form images of a landscape similar to images captured using a camera.

SAR presents its own unique set of benefits and challenges. One major benefit of SAR is that it can produce images of an area even at night or through cloud cover. Additionally, SAR can image a wide swath of land at an angle that would be difficult for a camera to achieve. However, SAR is more computationally complex than other imaging sensors. Image quality is also highly dependent on the quality of navigation information available.

In general, SAR requires that good navigation data be had in order to form SAR images. The research here explores the reverse problem where SAR images are formed without good navigation data and then good navigation data is inferred from the images.

This thesis performs feasibility studies and real data implementations that show how SAR can be used in navigation without the presence of GPS. Derivations and background

materials are provided. Validation methods and additional discussions are provided on the results of each portion of research.

ACKNOWLEDGMENTS

I want to express my thanks to my major professor, Dr. Randall Christensen, and to my committee, Dr. Jacob Gunther and Dr. Charles Swenson. A huge thanks goes to my wife for her patience and support. A thanks also goes to Sandia National Laboratories, who funded a large portion of this research. I also thank the Space Dynamics Laboratory for providing flight and radar test data for this research.

Colton P. Lindstrom

CONTENTS

LIST OF TABLES

LIST OF FIGURES

ACRONYMS

BPA	back-projection algorithm
DOF	degrees of freedom
DTED	digital terrain elevation data
DTM	digital terrain model
EKF	extended Kalman filter
FFT	fast Fourier transform
FM	frequency modulated
GNSS	global navigation satellite system
GPS	global positioning system
IMU	inertial measurement unit
INS	inertial navigation system
LFM	linear frequency modulated
ned	north east down
RCM	range cell migration
RCMC	range cell migration correction
RDA	range-Doppler algorithm
ROC	range of closest approach
SAR	synthetic aperture radar
STM	state transition matrix
TOC	time of closest approach
UAV	unmanned aerial vehicle

CHAPTER 1

INTRODUCTION

GPS-denied navigation is the process of precisely navigating a vehicle in a region without any sort of Global Navigation Satellite System (GNSS). To successfully perform this type of navigation, the information lost through GPS denial must be supplied to the navigation system via other sensors and instruments. Current research is exploring the effectiveness of various sensors at providing this lost information. Example sensors include optical cameras, lidar, radar, and range finders.

Motivation for this field of study arises from the relative ease with which GPS can be jammed or spoofed. GPS Denial can occur as a result of the environment in areas such as natural canyons, urban canyons, other obstructed areas, and multipath environments. Denial can also occur as a result of hostile entities broadcasting falsified GPS or jamming signals.

The focus of this research is radar aided GPS-denied navigation. Radar aided navigation can be categorized into several subsections. These subsections are shown in Figure 1.1. Methods of radar aided navigation are first sorted into absolute navigation and relative navigation. Absolute navigation places a vehicle on a global coordinate system such as latitude, longitude, and altitude. Relative navigation places the vehicle on a local coordinate system originating from some feature or last known location.

Absolute and relative navigation are further split into subcategories. Absolute radar aided navigation has been explored using terrain matching methods and synthetic aperture radar (SAR) based methods. Relative radar aided navigation has been explored using generic radar odometry, using Simultaneous Localization and Mapping (SLAM), and again using SAR images. A detailed review of literature for each of these subcategories is presented separately in Chapters 3, 4, and 5.

This thesis adds to the field by further investigating absolute radar aided GPS-denied

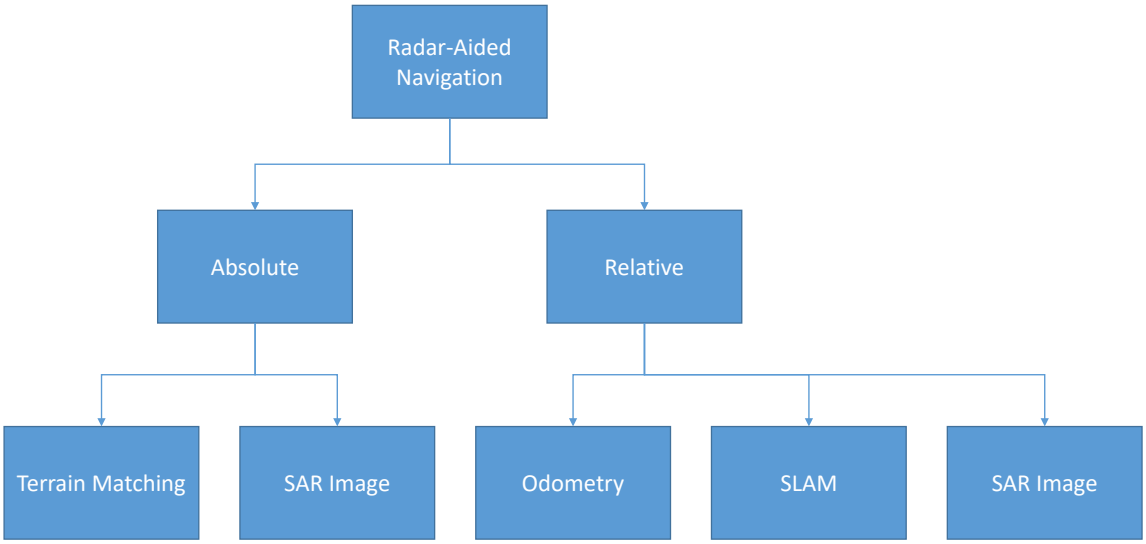

Fig. 1.1: Categorization of radar aided GPS-denied navigation.

navigation using synthetic aperture radar (SAR). SAR is the result of using radar data to form images of a landscape. Images produced by SAR are very similar to optical images but come with unique pros and cons. SAR is self-illuminating, meaning that image quality does not depend on the current lighting environment. As such, SAR can be used to form images at any time of day, including the middle of the night. The wavelength of SAR transmissions is such that they can penetrate cloud cover, rain, and snow, resulting in images that can be taken during inclement weather.

SAR operates by emitting sequential radar pulses with a specific waveform along a vehicle trajectory. Through a process of matched filtering, return signals from each emitted pulse are processed together to form an image. Several methods exist to filter SAR data. Two of the methods used and explored in this thesis are the back-projection algorithm (BPA) and the range-Doppler algorithm (RDA).

Using SAR in GPS-denied navigation has been proposed and researched in various forms. This research furthers the field of SAR based navigation. Contributions include a feasibility study using synthesized radar measurements to navigate, an in depth error analysis of how various navigation errors effect the SAR image formation process, and a full GPS-denied navigation implementation using both simulated and real radar and flight

data.

This thesis is written in a multiple paper format, where each chapter is an article at some stage of the publication process. One article is published, another is submitted for publication, and one is under revision and will soon be submitted for publication. The first paper explores the feasibility of using range, range-rate, and altitude measurements in an inertial navigation system (INS) with an extended Kalman filter (EKF) to perform navigation [1].

The second paper is an in-depth study of error characterization. It explores the specifics of how errors in the position, velocity, and attitude of a radar vehicle affect SAR image formation [2]. This study is motivated by previously performed research, which hypothesizes that SAR imaging errors can be used during GPS-denied navigation to infer navigation errors. This paper builds on the intuition and methods that would be needed to draw such inferences.

The third paper furthers work done in the first paper. In the first paper, measurements were synthesized from trajectory information. The third paper develops a technique to extract navigation information from SAR images. The technique is performed on both simulated and real radar and flight data. The measurement method is implemented within the INS structure developed in the first paper to fully realize a GPS-denied navigation system using SAR measurements.

This thesis is organized as follows. Chapter 2 provides background knowledge on navigation and SAR processing not otherwise included in the three academic papers. Chapter 3 is the presentation of the first paper on GPS-denied navigation feasibility. Chapter 4 is the presentation of the second paper on imaging error characterization given navigation error. Chapter 5 is the presentation of the third paper on a full GPS-denied navigation system using SAR image measurements. Chapter 6 summarizes the results from each paper and provides concluding discussion. An appendix is provided for derivations of crucial equations used in the research. A special appendix is also provided detailing copyright permissions of the three papers.

Abstracts and literature reviews are included on a chapter by chapter basis. References are not included chapter by chapter but are instead presented cumulatively after Chapter 6.

CHAPTER 2

BACKGROUND

This section covers background material on SAR processing and Kalman filtering not otherwise included in subsequent sections. Later chapters provide background material relevant to chapter specific topics. Material for this section is drawn mostly from [3] and [4].

2.1 Inertial Navigation System Structure

In this thesis, GPS denied navigation is performed using a 6DOF inertial navigation system (INS). An IMU corrupted by bias and noise is used to propagate the state of the aircraft. The navigation system uses an indirect EKF to estimate errors in the estimated vehicle state. This section provides a high-level overview of how the EKF is built into the INS. The material here is not meant to be exhaustive, as much of the finer details are included in later sections. Figure 2.1 shows a high-level system block diagram of the entire system.

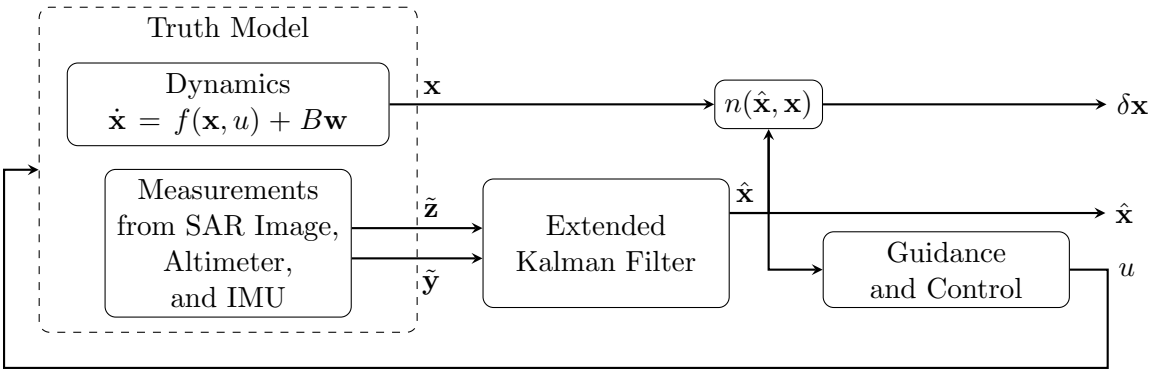

Fig. 2.1: Block diagram of the GPS-denied navigation system.

INS development begins by defining the truth state, estimated state, and error state shown as $\mathbf{x}$, $\hat{\mathbf{x}}$, and $\delta\mathbf{x}$, respectively. The truth state is the actual state of the vehicle. The estimated state, also known as the navigation state, is the INS's best guess of the

truth state. The error state is the error between the truth state and the navigation state. Associated with each state is a dynamics model. Details on the dynamics are given in later sections.

Because each type of state is related to each other, any two state types can be used to calculate the third. For example, the error state is calculated as the perturbation between the truth state and the navigation state. On the system block diagram, the mapping $n(\hat{\mathbf{x}}, \mathbf{x})$ captures this behavior.

The EKF processes measurements from the SAR imaging system together with an altimeter and produces an estimate of the truth state, which again is referred to as the navigation state $\hat{\mathbf{x}}$. The inclusion of Guidance and Control is a generalization of the navigation system and is included for completeness. However, for the purposes of this research, no guidance or control is used.

The structure of the EKF itself is shown in Figure 2.2. The EKF can be conceptually split into two sections; the propagate section and the update section. When no measurements are available to the EKF, the Navigation model produces a $\hat{\mathbf{x}}^-$, which is simply a propagation of the previous state estimate using the navigation dynamics. Additionally, the error state covariance is propagated using equations derived in later sections.

When a measurement is available, the EKF uses the previous state estimate to produce an updated state estimate, denoted $\hat{\mathbf{x}}^+$. This process is called a Kalman update. During the Kalman update, the following steps are performed.

1. Calculate a Kalman gain (K).
2. Use the Kalman gain to update the error state covariance (P^+).
3. Use the Kalman gain to update the estimate of the error state vector ($\delta\hat{\mathbf{x}}$).
4. Use the estimate of the error state vector to update the estimated state ($\hat{\mathbf{x}}^+$).

The Navigation Model block takes $\tilde{\mathbf{y}}$ as an input. These are continuous measurements from the accelerometer and gyroscope that help propagate the attitude and velocity states.

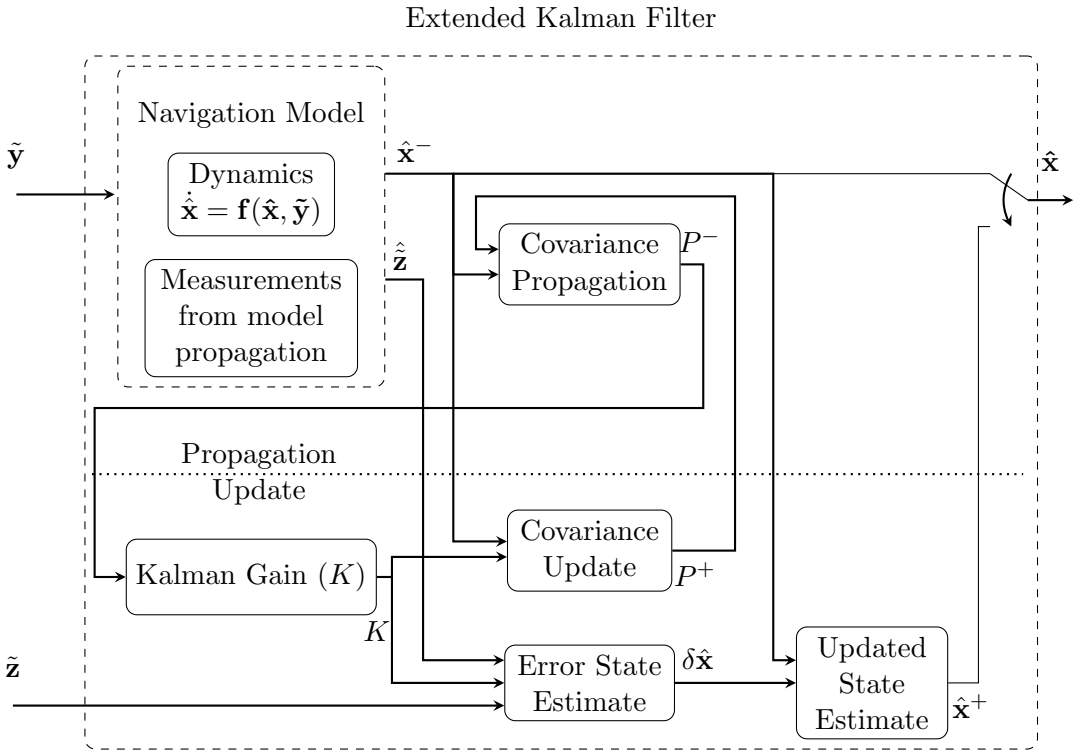

Fig. 2.2: Block diagram of the extended Kalman filter.

Because these sensors are not perfect representations, noise is introduced into the system at this stage.

There are two measurement vectors, $\tilde{\mathbf{z}}$ and $\hat{\tilde{\mathbf{z}}}$. The $\tilde{\mathbf{z}}$ vector is the measurement derived from SAR images and the altimeter. The $\hat{\tilde{\mathbf{z}}}$ vector is the INS's best estimate of what $\tilde{\mathbf{z}}$ should be using the navigation state. Both measurement vectors are used to estimate the error state of the vehicle.

2.2 Synthetic Aperture Radar Processing

In support of this research, SAR processing software is developed for both real and simulated data. The software is capable of simulating a flight path, injecting navigation errors into the trajectory, generating raw SAR data, performing range compression, forming SAR images on simulated and real data, and extracting measurements from fully formed images.

The process of forming an image using SAR starts with the signal transmission. Radar pulses are repeatedly transmitted along a vehicle trajectory. The rate at which the pulses are transmitted is called the pulse repetition frequency (PRF). Figure 2.3 illustrates how pulses are transmitted.

A single radar pulse is split into several sections as is shown in the figure. T_D is the duration of an individual radar pulse. T_w is the time of the sampling window. This is the window of time where the return pulses can be read and stored. The length of this window depends on several factors such as altitude, antenna beam pattern, and the pointing direction of the antenna.

T_N is a period of time immediately after the pulse is transmitted where no samples are taken. Generally, this time period is long enough to ignore the nadir bounce, which is the return signal of the pulse from immediately underneath the radar vehicle. This time period may also depend on the antenna footprint, which may create a period of time where valid return samples are not available.

T_M is much like T_N in that it is again a period of time where no received samples are taken. This period of time can be variable but is typically only large enough for the signal path on the antenna to change from receive to transmit (in the case of a monostatic system). In systems where a high PRF is not important, then T_M is simply the dead time between sampling a return pulse and transmitting a new pulse.

Radar pulses can have different shapes depending on specific objectives of a system. For SAR imaging, the most common waveform is a linear frequency modulated (LFM) pulse. This is a pulse that has a frequency that varies linearly in time according to a frequency modulation (FM) rate. Details on LFM pulses and their importance in SAR imaging are provided in subsequent sections.

The resolution of a SAR image in the range direction is related to the bandwidth of the LFM pulse. The bandwidth of a pulse is defined as the set of frequencies spanned by the significant energy of the LFM pulse. The pulse bandwidth is calculated as,

$$BW = |K|T \tag{2.1}$$

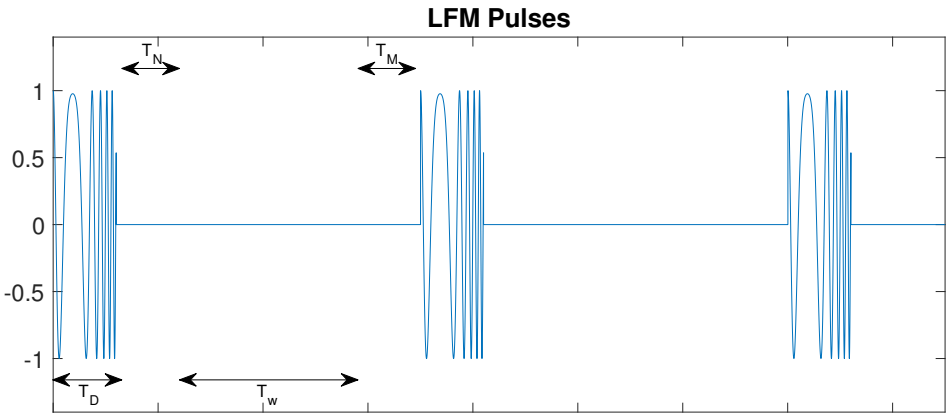

Fig. 2.3: Illustration of how radar pulses are transmitted according to a PRF.

where K is the FM rate and T is the total pulse duration

After calculating the pulse bandwidth, the range resolution can be shown to be approximately equal to

$$\rho_{rng} = \frac{c}{2 * BW} \tag{2.2}$$

The resolution in the azimuth direction is not dependent on the LFM pulse like range resolution. Instead, assuming the whole antenna azimuth swath has passed over the image area in question, then the azimuth resolution is a function of the physical length of the antenna, L_a.

$$\rho_{azm} = \frac{L_a}{2} \tag{2.3}$$

Forming SAR images from received radar pulses is a process of matched filtering. Collected data is processing through a matched filter in the range direction first, which results in range compressed data. The range compressed data is then processed again in the azimuth direction to form azimuth compressed data.

Compression in the azimuth direction is complicated by the fact that ground targets appear as hyperbolic curves in the range compressed data. This can be explained by the hyperbolic range equation, which is an expression for the instantaneous range between the radar vehicle and a ground target at any point in time. Denoted $R(\eta)$, the hyperbolic range

equation is defined as

$$R(\eta) = \sqrt{R_0^2 + V^2\eta^2} \tag{2.4}$$

where R_0 is the range of closest approach, V is the vehicle's forward velocity, and η is azimuth time.

The effect of the hyperbolic range equation is illustrated in Figure 2.4. This illustration shows a sequence of range compressed pulses with their peaks forming a hyperbolic curve. The eccentricity of the curve is exaggerated for illustration purposes.

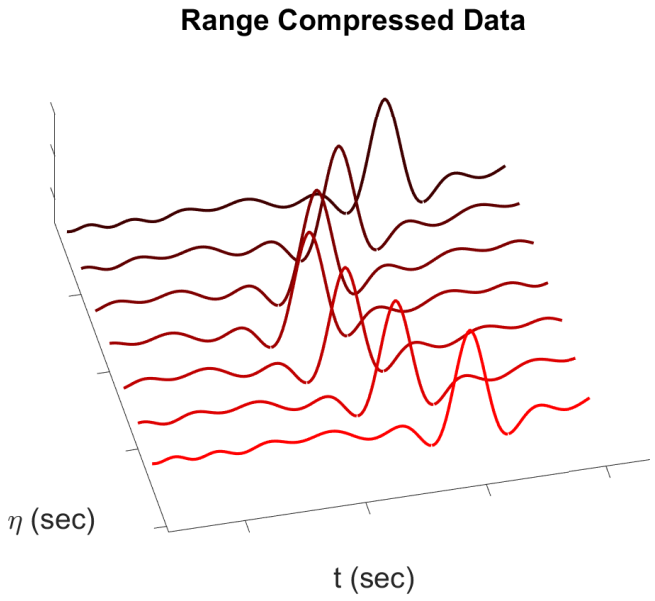

Fig. 2.4: Illustration of the hyperbolic shape of range compressed data where η is azimuth time and t is range time.

Different imaging algorithms use different methods to filter the data in the azimuth direction. For example, BPA using a time domain matched filter to compress the data in the azimuth direction. RDA uses a Fourier domain based method to compress the data. Specific details on imaging algorithms are provided in later sections.

CHAPTER 3
AN INVESTIGATION OF GPS-DENIED NAVIGATION USING AIRBORNE RADAR TELEMETRY

A supplementary sensor being explored in the field of GPS-denied navigation is Synthetic Aperture Radar (SAR) with its resulting images. In contrast to passive, camera-based methods, SAR provides illumination of a scene, direct measurement of range, and can operate day and night or through inclement weather. The research presented in this paper investigates the feasibility of using range and range-rate measurements from a SAR system to perform GPS-denied navigation. In support of this research, a 6DOF aircraft navigation and radar simulation is developed and presented. The core sensor used to propagate the navigation states is an inertial measurement unit, corrupted by bias and noise. An indirect extended Kalman filter (EKF) is developed and the covariance of estimation errors is validated via Monte Carlo analysis.

3.1 Introduction

GPS is a vital part of an INS. Without GPS, the system is forced to "Dead Reckon", which is to navigate without any external position update from GPS or radio link. Navigating without GPS is subject to drift and will result large inaccuracies over time. In situations where GPS is unavailable or unreliable, a UAV must perform "GPS-denied Navigation".

There are many examples that motivate GPS-denied navigation. In large cities, the buildings form what is called an "Urban Canyon". Because tall buildings obstruct the sky and reflect incoming signals, GPS signals in urban canyons are unreliable and sometimes unavailable. During military operations, GPS can be easily spoofed or jammed. These and other such examples have motivated researchers to find efficient and reliable forms of GPS-denied navigation.

Of the many different methods, one supplementary sensor being explored in GPS-denied

navigation is Synthetic Aperture Radar (SAR). SAR is a method of producing images of an area using sequential radar pulses as an air/space craft flies along a given trajectory. This project explores using range measurements and range-rate measurements from a radar system in conjunction with an INS to estimate the trajectory of a UAV.

3.2 Literature Review

Historically, some major disadvantages of implementing a radar system are the size, weight, and power requirements of the system. This would cause radar to be infeasible for smaller UAVs; however, significant research has been performed to miniaturize radar systems for UAV applications. Currently, flexible, light weight radar systems are available commercially through IMST Radar that weigh as little as 164 grams [5].

GPS-denied navigation using radar can be split into two types: absolute navigation and relative navigation. Absolute navigation finds the location of the UAV on a global coordinate system, such as latitude, longitude, altitude. Relative navigation finds the location of the UAV relative to some previously known location or target location.

Absolute navigation typically involves comparing collected data to an on-board terrain map, elevation map, or satellite image. This kind of approach was performed by Nitti et al in [6] using interferometric SAR. Greco et al used a similar method in [7].

Relative navigation does not try to determine an absolute position for the UAV, but instead estimates the location of the UAV relative to the point where GPS was lost. This is typically accomplished by associating radar data to prominent ground targets and tracking those targets throughout the UAV's trajectory. Scannapieco et al [8] performs this type of navigation using a constant false alarm rate to detect prominent targets and then using a global nearest neighbor approach to track targets.

In [9] and [10], Quist, Beard, and Niedfeldt detected and tracked targets using the Hough transform. Unfortunately, the Hough transform is computationally expensive, which is not feasible on some light UAV systems. In later papers, Quist et al proposed and tested the Recursive RANSAC algorithm as a replacement of the Hough transform [11], [12].

Similar research has been performed by Kauffman et al using a method called Simultaneous Localization and Mapping (SLAM) [13].

Radar data can be kept as either raw collected data, range compressed data, or fully formed SAR images. Many of the absolute navigation methods use full SAR images in conjunction with raw data and DTMs. Each type of data set has an associated computational complexity, where raw data is the simplest form and fully formed images are the most complex. To form a SAR image means filtering the raw data using matched filters. Filtering once in the range dimension produces range compressed data. After range compression, filtering in the azimuth dimension produces images [3].

To form high quality SAR images, the position of the aircraft at any given time must be known with high accuracy. Errors in position will manifest themselves in the final image as translations and blurrings of an imaged target. Research performed at Utah State University has explored the effects of navigation errors on formed SAR images and has explored methods of performing navigation based on the characteristics of the imaging errors [14].

Several methods exist to form SAR images. One of the most computationally expensive, but also one of the most accurate methods is the Back-Projection Algorithm (BPA). The previously mentioned research at Utah State University was performed using BPA SAR images to extract navigation errors. Other image formations with less computation complexity exist, such as the Range-Doppler Algorithm (RDA). This algorithm sacrifices image quality for a drastic reduction in computational complexity by using the FFT.

3.3 Method

This research could fall into the categories of either absolute or relative navigation, depending on the knowledge of the target in the radar scene. To achieve GPS-denied navigation, this research implements an INS and EKF system structure supplemented with radar telemetry. Beginning with single point targets, necessary navigation data is extracted from the radar data and processed within the EKF to produce estimates of the UAV state.

There exists an ambiguity between cross-track estimation errors and elevation estimation errors. To help resolve the ambiguity, an additional altitude measurement is provided to the EKF to help estimate the UAV state. This potential ambiguity exists due to several different combinations of cross-track and elevation trajectory errors that could produce an identical error pattern in the collected and processed radar data. This is illustrated in Figure 3.1, which shows a continuum of cross-track and elevation positions that have a constant range in relation to a target on the ground. This constant range to the target leads to constant range of closest approach as extracted from radar telemetry for a given target.

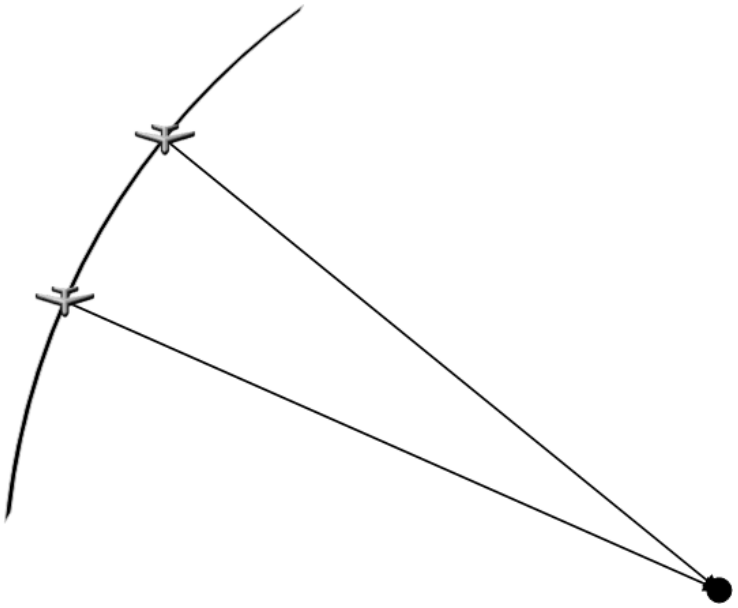

Fig. 3.1: Cross-track and elevation estimates are not unique given a slant range to target.

Measuring the altitude is most easily performed using an altimeter; however, this could also be measured using a nadir bounce coupled with a Digital Terrain Elevation Data (DTED) set. Using the nadir bounce and DTED does introduce another source of estimation error, as now the UAV location in relation to the DTED must be known to get accurate elevation data.

Figure 3.2 helps visualize the geometry of the UAV in relation to the target and how

it relates to radar telemetry. In the figure, the time varying range and the range of closest approach are shown. The range measurement is equivalent to the time varying range in the figure.

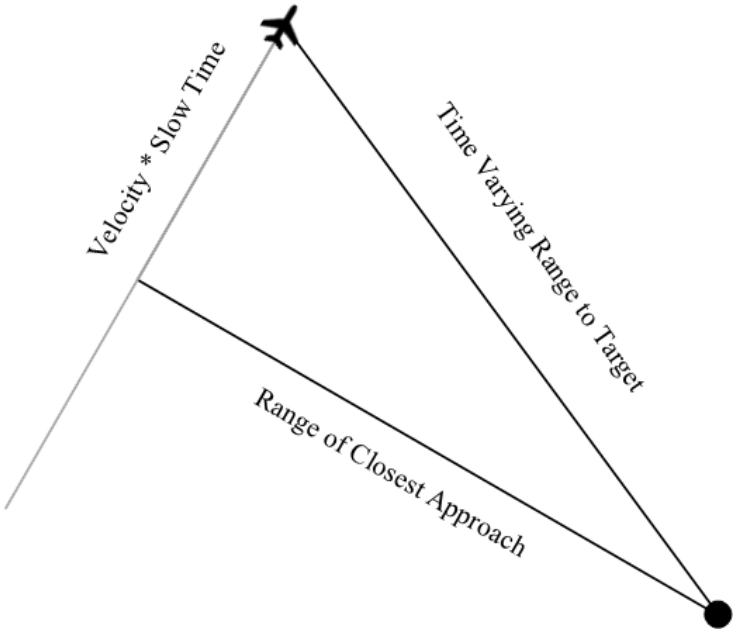

Fig. 3.2: Geometry of the UAV relative to the ground target.

Range to target, range-rate, and altitude measurements are combined in the EKF to enable navigation independent of GPS. Once the INS and EKF structure is defined and validated, further research will explore the effectiveness and sensitivity of the implementation. This will be done by analyzing changes in results due to different grades of IMUs, different types and levels of measurement noise, and different locations for radar ground targets.

3.4 State and Model Definitions

The EKF development begins by defining the truth state, estimated state, and error state with their associated dynamics. Before defining state vectors and state models, coordinate systems are defined. This research uses the flat earth model as a reference frame. There are three coordinate systems of interest. These are: 1) The North-East-Down frame (ned) with the origin attached to the body of the UAV, 2) The inertial frame (i) aligned

with the North-East-Down frame with its origin fixed on the Flat Earth model, and 3) The body frame (b) attached to the body of the UAV with the x axis pointing out the nose of the UAV, the y axis pointing out the right wing, and the z axis pointing out the belly of the UAV.

With a defined coordinate system, state vectors and models can be defined. The truth state vector is governed by the truth model, denoted $\mathbf{x}$, the estimated state vector is governed by the navigation model, denoted $\hat{\mathbf{x}}$, and the error state vector is governed by a linear perturbation model, denoted $\delta\mathbf{x}$.

The truth state and associated dynamics are defined as

$$\dot{\mathbf{x}} = \begin{bmatrix} \dot{\mathbf{p}}^{ned} \\ \dot{\mathbf{v}}^{ned} \\ \dot{q}_b^{ned} \\ \dot{\mathbf{b}}_{accel} \\ \dot{\mathbf{b}}_{gyro} \\ \dot{b}_{alt} \\ \dot{b}_{range} \\ \dot{b}_{rate} \end{bmatrix} = \begin{bmatrix} \mathbf{v}^{ned} \\ R_b^{ned}\nu^b + g^{ned} \\ q_b^{ned} \otimes \frac{1}{2}\begin{bmatrix} 0 \\ \omega^b \end{bmatrix} \\ -\frac{1}{\tau_{accel}}\mathbf{b}_{accel} + \mathbf{w}_{accel} \\ -\frac{1}{\tau_{gyro}}\mathbf{b}_{gyro} + \mathbf{w}_{gyro} \\ -\frac{1}{\tau_{alt}}b_{alt} + w_{alt} \\ -\frac{1}{\tau_{range}}b_{range} + w_{range} \\ -\frac{1}{\tau_{rate}}b_{rate} + w_{rate} \end{bmatrix} \tag{3.1}$$

where the elements of the state vector are respectively the position vector as expressed in the *ned* frame, velocity vector as expressed in the *ned* frame, attitude quaternion between the b and *ned* frames, accelerometer bias vector, gyroscope bias vector, altimeter bias, radar range bias, and radar range-rate bias. Additionally, the $\otimes$ symbol represents quaternion multiplication, R_b^{ned} is the rotation matrix that rotates vectors from the UAV body frame to the *ned* frame, ν^b is a measurement from the accelerometer, g^{ned} is the gravitational constant, and ω^b is a measurement from the gyroscope.

Note that each bias state is governed by a first order Markov model. Each Markov model contains a time constant term ($\frac{1}{\tau_i}$) and a process noise term ($\mathbf{w}_i$). There are Markov models for the accelerometer bias, gyroscope bias, altimeter bias, radar range bias, and

range rate bias states.

The estimated state and navigation model are nearly identical to the truth state and truth model apart from the velocity state and the attitude state. In the navigation model, the velocity state and attitude state are propagated using measurements of specific force and angular rate, compensated by the current estimate of the corresponding bias.

$$\begin{bmatrix} \dot{\hat{\mathbf{v}}}^{ned} \\ \dot{q}_{\hat{b}}^{ned} \end{bmatrix} = \begin{bmatrix} R_{\hat{b}}^{ned}(\tilde{\nu}^b - \hat{\mathbf{b}}_{\mathbf{accel}}) + g^{ned} \\ q_{\hat{b}}^{ned} \otimes \frac{1}{2} \begin{bmatrix} 0 \\ \tilde{\omega}^b - \hat{\mathbf{b}}_{gyro} \end{bmatrix} \end{bmatrix} \tag{3.2}$$

Another key difference between the truth model and the navigation model is the absence of noise terms in the navigation model. The navigation model has no knowledge of noise. Consequently, noise cannot be subtracted off of sensor measurements and bias states. As such, the navigation model attempts to remove the bias from the accelerometer and gyroscope measurements but cannot be completely successful.

It is important to clarify that ν^b and ω^b are both truth measurements from the accelerometer and gyroscope, respectively. An actual measurement from either instrument will be corrupted by noise and bias. The resulting accelerometer measurement, $\tilde{\nu}^b$, and gyroscope measurement, $\tilde{\omega}^b$, are,

$$\tilde{\nu}^b = \nu^b + \mathbf{b}_{accel} + \mathbf{n}_\nu \tag{3.3}$$

$$\tilde{\omega}^b = \omega^b + \mathbf{b}_{gyro} + \mathbf{n}_\omega \tag{3.4}$$

where $\mathbf{n}_\nu$ and $\mathbf{n}_\omega$ are sensor noise vectors. Note the $\hat{}$ over each state variable and real measurement. This notation is used throughout the paper and indicates an estimate.

The error state and perturbation model require more work to define. To do so, the truth states are defined as a small perturbation from the estimated states. The truth model is then expanded about the estimated state, after which the estimated state and nonlinear terms are discarded. This results in a linear error model describing the dynamics of the error state.

Because the error model is a linear model, it can be written in matrix notation in the form

$$\delta\dot{\mathbf{x}} = \hat{F}\delta\mathbf{x} + B\mathbf{w} \tag{3.5}$$

where $\hat{F}$ is defined as

$$\hat{F} = \begin{bmatrix} F_{11} & F_{12} \\ 0_{9\times 9} & F_{22} \end{bmatrix} \tag{3.6}$$

where

$$F_{11} = \begin{bmatrix} 0 & I & 0 \\ 0 & 0 & [R_{\hat{b}}^{ned}(\tilde{\nu}^b - \hat{\mathbf{b}}_{accel})]\times \\ 0 & 0 & 0 \end{bmatrix} \tag{3.7}$$

$$F_{21} = \begin{bmatrix} 0 & 0 & 0 & 0 & 0 \\ -R_{\hat{b}}^{ned} & 0 & 0 & 0 & 0 \\ 0 & R_{\hat{b}}^{ned} & 0 & 0 & 0 \end{bmatrix} \tag{3.8}$$

$$F_{22}\begin{bmatrix} -\frac{1}{\tau_{accel}}I & 0 & 0 & 0 & 0 \\ 0 & -\frac{1}{\tau_{gyro}}I & 0 & 0 & 0 \\ 0 & 0 & -\frac{1}{\tau_{alt}} & 0 & 0 \\ 0 & 0 & 0 & -\frac{1}{\tau_{range}} & 0 \\ 0 & 0 & 0 & 0 & -\frac{1}{\tau_{rate}} \end{bmatrix} \tag{3.9}$$

In equation 3.7, the "cross" operator, $\times$ is defined as

$$\times : \mathbb{R}^{3x1} \rightarrow \mathbb{R}^{3x3}, \text{ s.t. } (\mathbf{a}\times) = \begin{bmatrix} 0 & -a_3 & a_2 \\ a_3 & 0 & -a_1 \\ -a_2 & a_1 & 0 \end{bmatrix}$$

where $\mathbf{a} = [a_1, a_2, a_3]^T$.

B is defined as

$$B = \begin{bmatrix} B_{11} & 0_{9\times 9} \\ 0_{9\times 9} & I_{9\times 9} \end{bmatrix} \tag{3.10}$$

where

$$B_{11} = \begin{bmatrix} 0 & 0 \\ -R_{\hat{b}}^{ned} & 0 \\ 0 & R_{\hat{b}}^{ned} \end{bmatrix} \tag{3.11}$$

and $\mathbf{w}$ is the noise vector.

$$\mathbf{w} = [\mathbf{n}_\nu, \mathbf{n}_\omega, \mathbf{w}_{accel}, \mathbf{w}_{gyro}, w_{alt}, w_{range}, w_{rate}]^T \tag{3.12}$$

3.5 Measurement Model

At each Kalman update time, measurements from the SAR image and altimeter must be taken. Specifically, three measurements will be extracted from the data: Range to target, range rate with respect to target, and altitude. For the purposes of this project, the location of a given ground target is known. Knowledge of the target can be either global (latitude-longitude) or relative (with respect to time of GPS loss).

The measurement functions can be constructed intuitively using Figure 3.3. In the figure, $\mathbf{r}$ is the known position of a ground target in the inertial frame i as expressed in the *ned* frame. $\mathbf{p}^{ned}$ is the position of the UAV in the i frame as expressed in the *ned* frame. The range from the UAV to the target is the magnitude of the difference of the two position vectors, $||\mathbf{r} - \mathbf{p}^{ned}||$. The range rate is velocity of the aircraft, $\mathbf{v}^{ned}$, projected into the direction of $\mathbf{r} - \mathbf{p}^{ned}$.

There are two measurement models of importance. The first model is the measurement taken from the onboard sensors denoted $\tilde{\mathbf{z}}$. $\tilde{\mathbf{z}}$ is defined as

$$\tilde{\mathbf{z}} = \begin{bmatrix} \tilde{\mathbf{z}}_{alt} \\ \tilde{\mathbf{z}}_{range} \\ \tilde{\mathbf{z}}_{rate} \end{bmatrix} = \begin{bmatrix} -p_z + b_{alt} + n_{alt} \\ ||\mathbf{r} - \mathbf{p}^{ned}|| + b_{range} + n_{range} \\ -(\mathbf{v}^{ned})^T \frac{\mathbf{r}-\mathbf{p}^{ned}}{||\mathbf{r}-\mathbf{p}^{ned}||} + b_{rate} + n_{rate} \end{bmatrix} \tag{3.13}$$

where n is measurement noise and p_z is the *down* component of the position state.

For the purposes of this project, these measurements are synthesized using the truth state vector of the UAV. In reality, these measurements would come from the SAR images

and altimeter. The second function is the estimated measurement denoted $\hat{\tilde{\mathbf{z}}}$. This is the value produced by propagation of the navigation model just before the Kalman update. $\hat{\tilde{\mathbf{z}}}$ identical to $\tilde{\mathbf{z}}$ except that it is evaluated using the current estimated state rather than the truth state.

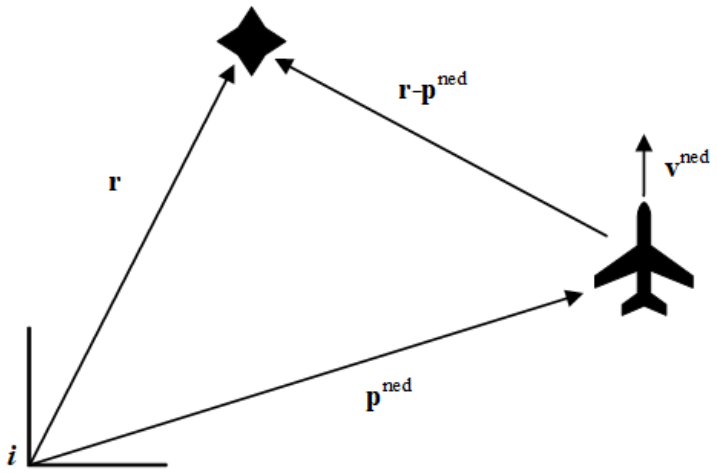

Fig. 3.3: Geometry of range, range rate, and altitude measurements.

The measurement model must be linearized for processing in the EKF. This yields a matrix H. This matrix H will be used in calculating the Kalman gain K and the updated covariance value P^+.

The linear measurement model is of the form

$$\delta\tilde{\mathbf{z}} = H\delta\mathbf{x} + G\nu \tag{3.14}$$

where ν is a measurement noise vector.

$$\nu = [n_{range}, n_{rate}, n_{alt}]^T \tag{3.15}$$

The matrix H is found by forming the Jacobian of the measurement model and evaluating at $\hat{\mathbf{x}}$.

$$H = \begin{bmatrix} H_1 & 0_{3\times 9} & I \end{bmatrix} \tag{3.16}$$

where

$$H_1 = \begin{bmatrix} [0,0,-1] & 0_{1\times 3} \\ \frac{-\mathbf{d}^T}{||\mathbf{d}||} & 0_{1\times 3} \\ \frac{(\hat{\mathbf{v}}^{ned})^T}{||\mathbf{d}||} - \frac{(\hat{\mathbf{v}}^{ned})^T \mathbf{d}\mathbf{d}^T}{||\mathbf{d}||^3} & \frac{-\mathbf{d}^T}{||\mathbf{d}||} \end{bmatrix} \tag{3.17}$$

and where $\mathbf{d} = \mathbf{r} - \mathbf{p}^{ned}$.

3.6 Covariance Propagation

The objective of this section is to develop the individual components of the error state covariance propagation equation, where the error state covariance is denoted P. The covariance propagation can be shown to be

$$\dot{P} = \hat{F}P + P\hat{F} + BQB^T \tag{3.18}$$

where $\hat{F}$ and B are defined in Section 3.4.

The Q matrix in the covariance propagation equation is defined as the power spectral density of the noise vector $\mathbf{w}$ defined in equation 3.12. Assuming each noise component is zero mean, gaussian, and independent, Q is a diagonal equal to

$$\begin{aligned} Q = diag(&\sigma^2_{vrw} I_{3\times 3}, \sigma^2_{arw} I_{3\times 3}, \frac{2\sigma^2_{ss,b_{accel}}}{\tau_{accel}} I_{3\times 3}, \\ &\frac{2\sigma^2_{ss,b_{gyro}}}{\tau_{gyro}} I_{3\times 3}, \frac{2\sigma^2_{ss,b_{alt}}}{\tau_{alt}}, \frac{2\sigma^2_{ss,b_{range}}}{\tau_{range}}, \frac{2\sigma^2_{ss,b_{rate}}}{\tau_{rate}}) \end{aligned} \tag{3.19}$$

3.7 Kalman Update

When a measurement is available to the EKF, a Kalman update is performed.

The equation for the Kalman gain is given by

$$K = P^- H^T(\hat{\mathbf{x}}^-)[H(\hat{\mathbf{x}}^-)P^- H^T(\hat{\mathbf{x}}^-) + GRG^T]^{-1} \tag{3.20}$$

where P^- is the error state covariance before the Kalman update, $H(\hat{\mathbf{x}}^-)$ is the measurement sensitivity matrix, G is the noise coupling matrix, and R is the covariance of the

measurement noise vector.

The error state covariance is updated using the Joseph form, which is given by

$$P^{+} = [I - KH(\hat{\mathbf{x}}^{-})]P^{-}[I - KH(\hat{\mathbf{x}}^{-})]^{T} + KGRG^{T}K^{T} \tag{3.21}$$

The estimate of the error state is given by

$$\delta\hat{\mathbf{x}}^{+} = K[\tilde{\mathbf{z}} - \hat{\tilde{\mathbf{z}}}] \tag{3.22}$$

After calculating an estimate of the error state vector, the estimate is applied to the estimated state, which forms an updated estimated state vector. This is done using the mapping,

$$\hat{\mathbf{x}}^{+} = \begin{bmatrix} (\hat{\mathbf{p}}^{ned})^{-} + \delta\mathbf{p}^{ned} \\ (\hat{\mathbf{v}}^{ned})^{-} + \delta\mathbf{v}^{ned} \\ \begin{bmatrix} 1 \\ -\frac{1}{2}\delta\theta_{b}^{ned} \end{bmatrix} \otimes (q_{b}^{ned})^{-} \\ (\hat{\mathbf{b}}_{accel})^{-} + \delta\mathbf{b}_{accel} \\ (\hat{\mathbf{b}}_{gyro})^{-} + \delta\mathbf{b}_{gyro} \\ (\hat{b}_{alt})^{-} + \delta b_{alt} \\ (\hat{b}_{range})^{-} + \delta b_{range} \\ (\hat{b}_{rate})^{-} + \delta b_{rate} \end{bmatrix} \tag{3.23}$$

3.8 Filter Validation

This section validates the equations and definitions of the extended Kalman filter. Before validation, an R matrix is selected, which determines the noise variances of the radar and altimeter measurements. For this section, R is equal to

$$R = \begin{bmatrix} \sigma^{2}_{\tilde{z}_{range}} & 0 & 0 \\ 0 & \sigma^{2}_{\tilde{z}_{rate}} & 0 \\ 0 & 0 & \sigma^{2}_{\tilde{z}_{alt}} \end{bmatrix} \tag{3.24}$$

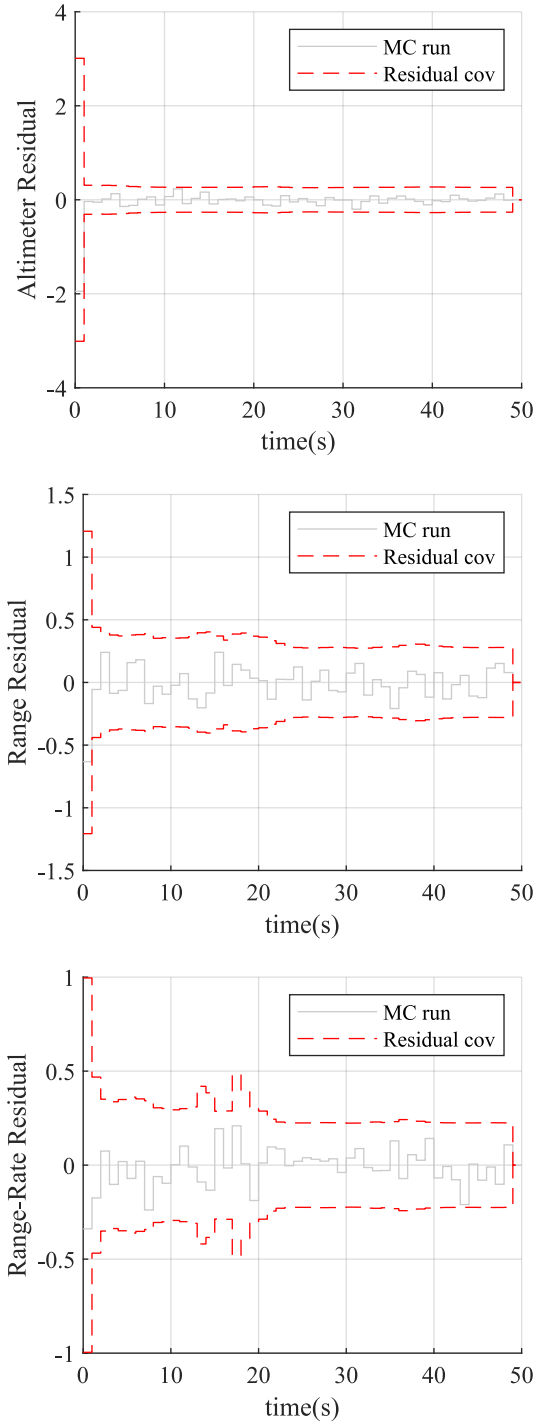

Fig. 3.4: Residual measurements after implementation of Kalman updates. From top to bottom: Altimeter residual, range residual, range-rate residual.

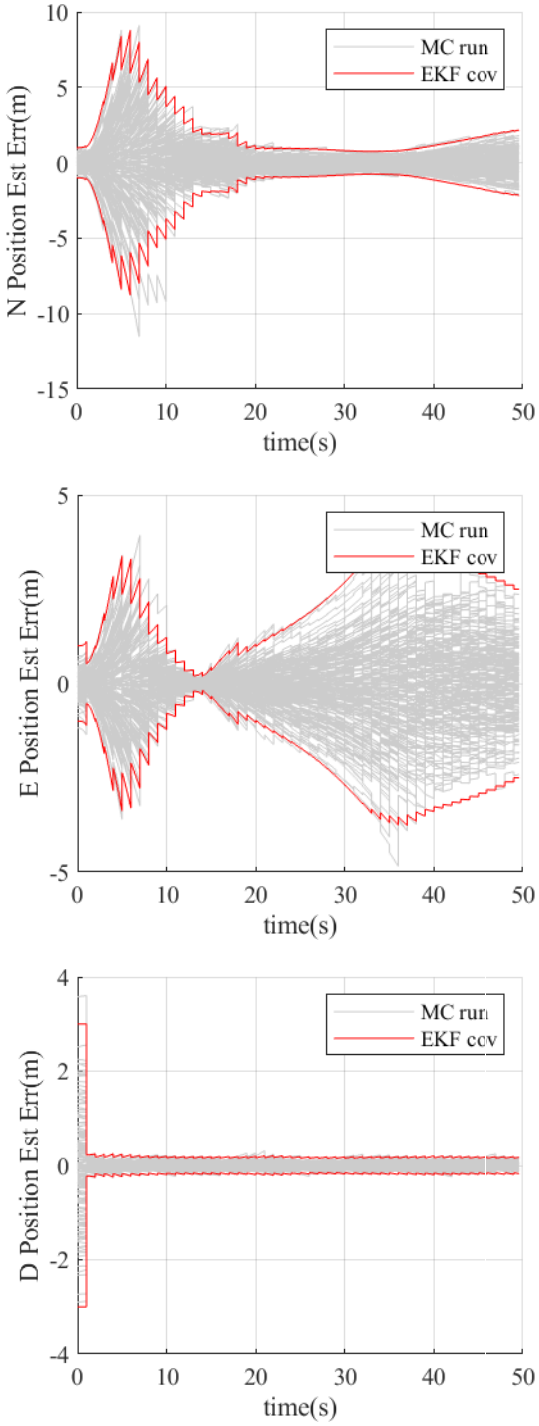

Fig. 3.5: Monte Carlo simulation with filtered covariance bounds. From top to bottom: North position east position, down position.

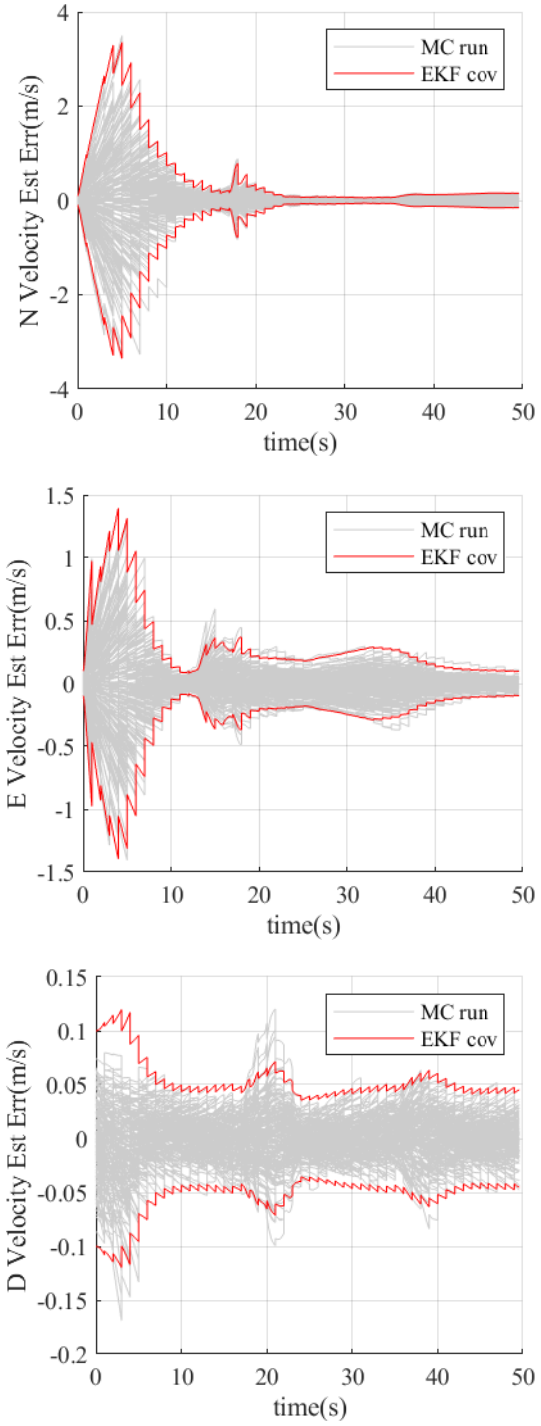

Fig. 3.6: Monte Carlo simulation with filtered covariance bounds. From top to bottom: North velocity east velocity, down velocity.

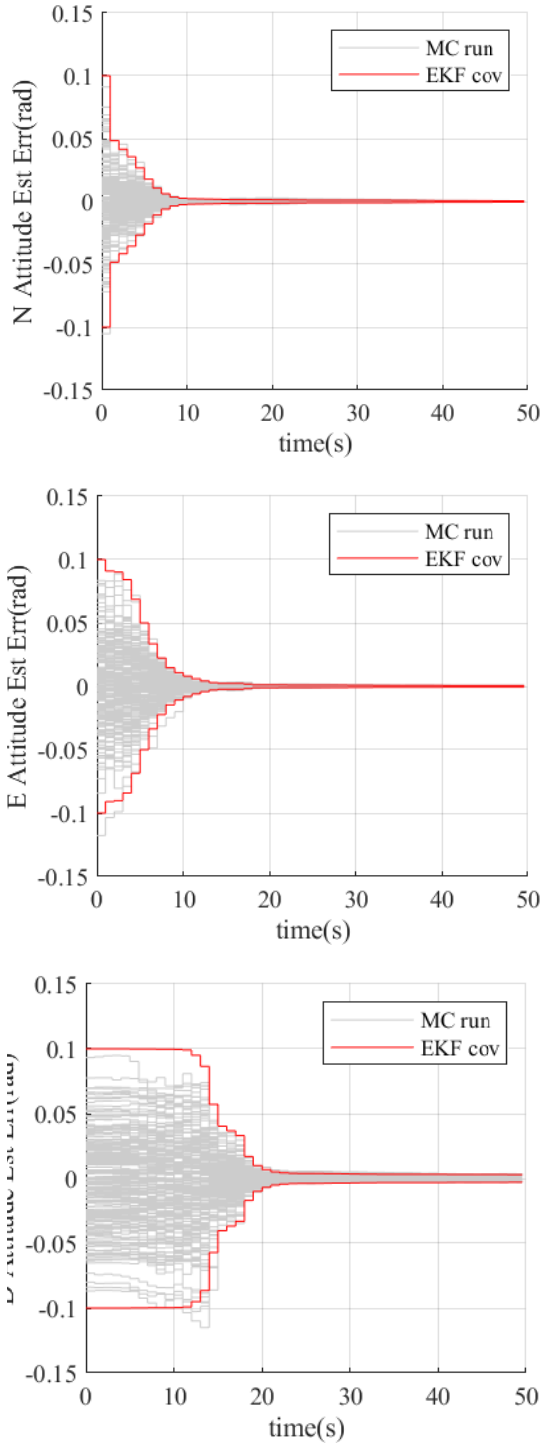

Fig. 3.7: Monte Carlo simulation with filtered covariance bounds. From top to bottom: North attitude east attitude, down attitude.

where the $\sigma_{\tilde{z}_i}$ are selected by the user and are defined in Table 3.1.

Table 3.1: Noise standard deviations used for SAR and altimeter measurement noises.

3σ (Measurement)	Values
$\sigma_{\tilde{z}_{radar}}$	0.2 (m)
$\sigma_{\tilde{z}_{rate}}$	0.2 (m/s)
$\sigma_{\tilde{z}_{alt}}$	0.2 (m)

If implemented correctly, the Kalman filter should produce residual measurements that are zero-mean and white. After a single Monte Carlo run, the residual measurements with their associated covariances are plotted. These plots are shown in Figure 3.4. In the figure, the solid line represents the residual from a single Monte Carlo run and the dotted line represents the 3σ bounds of the measurement residual.

It is observed that the measurement residuals satisfy the zero-mean and white conditions. To further validate correct implementation of the Kalman update equations, a Monte Carlo simulation with 200 runs is performed. Results of this validation are 3σ error state covariance bounds that shrink as time goes on with each Kalman update. The results of these tests are shown in Figures 3.5, 3.6, and 3.7.

After EKF implementation, the covariance of the estimation error diminishes. This further implies correct definition and implementation of the Kalman update equations.

3.9 Results

This section documents the studies and contributions performed by this project. Three separate studies were performed. One on the sensitivity of estimation errors to changes in IMU grade. The second on the sensitivity to measurement noise strength. The third on the sensitivity to the geometric relationship between the platform and target is studied.

3.9.1 Sensitivity to IMU Grade

To test the sensitivity of the INS to IMU grade, a single iteration of the Monte-Carlo simulation is run with noise typical of consumer grade, tactical grade, and navigation grade

IMUs.

Table 3.2 shows the different parameters chosen for the IMU grade study. Values in the table are reported as 3σ values. In the table, note that vrw and arw stand for velocity random walk and angular random walk, respectively.

Table 3.2: Different IMU grades used in investigation expressed as 3σ values.

IMU Grade	$\sigma_{3s,vrw}$	$\sigma_{3s,accel}$	$\sigma_{3s,arw}$	$\sigma_{3s,gyro}$
Consumer	0.6	0.01	0.7	10
Tactical	0.06	0.001	0.07	1
Navigation	0.006	0.0001	0.007	0.1

The results of the study are shown in Figure 3.8. The three plots shown show the north, east, and down position estimation errors expressed as 3σ covariance bounds.

Improvements in state estimates are evident with each IMU upgrade, but the difference between navigation grade and tactical grade is much smaller than the difference between tactical grade and consumer grade. This is most evident in the north and east position states. Down position states are less affected by IMU grade because of available direct altitude measurements from the altimeter.

3.9.2 Sensitivity to SAR Measurement Noise

This section studies the effects of different measurement noise variances on the accuracy of the state estimations. Table 3.3 shows the different measurement noise strengths used for each test in this study. The measurement noise strengths are expressed in the table as 3σ values. The noise strength is changed one measurement at a time in order to isolate how the uncertainty of a single measurement affects the state estimations.

As in the IMU grade study, plots of position estimation error covariance bounds are given. These plots are shown in Figure 3.9

The figure shows that altimeter measurement noise strongly affects the down position and down velocity state estimates. Range-rate and range measurement noise affected the north and east positions but had little effect on the down position.

Table 3.3: Levels of measurement noise used in investigation expressed as 3σ values.

Test #	$\sigma_{3s,n_{range}}$ (m)	$\sigma_{3s,n_{rate}}$ (m/s)	$\sigma_{3s,n_{alt}}$ (m)
1	0.2	0.2	0.2
2	2	0.2	0.2
3	0.2	2	0.2
4	0.2	0.2	2

3.9.3 Sensitivity to Platform/Target Geometry

This section studies how the positioning of the ground target affects state estimation. Table 3.4 lists the different locations of the ground target in the local cartesian coordinate system. Note that in the local coordinate system, the flight trajectory begins as the point [0, -200, 0] and travels directly north.

Table 3.4: Different locations of the ground target relative to the flight trajectory used in investigation.

Test #	r^n (m)	r^e (m)	r^d (m)
1	500	0	0
2	500	500	0
3	500	1000	0
4	500	1500	0
5	1000	0	0
6	1000	500	0
7	1000	1000	0
8	1000	1500	0

Results of this study are shown in Figures 3.10 and 3.11. Each of the plots in the figure are of the same format as previous studies. That is to say that each plot shows 3σ covariance bounds of the position estimation error. For this study, only north and east position estimation errors are shown, because altitude errors are invariant to ground target location due to the availability of altitude measurements.

The location of the ground target dramatically affects the convergence rates of the north and east state estimates. Convergence behavior improves as the ground target grows closer to the flight trajectory and as the ground target moves closer to the beginning of the flight trajectory.

3.10 Conclusion

This research studies the estimation performance of an INS aided by an altimeter and radar telemetry. Radar measurements are derived from range and range rate to ground targets. The studies performed explored how noise strength, measurement fidelity, and target location affect state estimation error.

The simulation results suggest that GPS-denied navigation using radar telemetry is most feasible when using either a tactical or navigation grade IMU and when using a SAR system with high fidelity range measurements. The simulation also demonstrates that the location of the ground target significantly influences estimation performance. Overall, targets close to the flight trajectory yielded better estimation performance. The results further suggest that no substantial benefit is achieved when upgrading from tactical to navigation grade, which motivates the use of the tactical grade IMU.

In general, the estimates with the most error were the north and east position estimates. Down position estimates were small due to the presence of altimeter measurements.

3.11 Acknowledgments

This research was funded in part by Sandia National Laboratories, whom we thank.

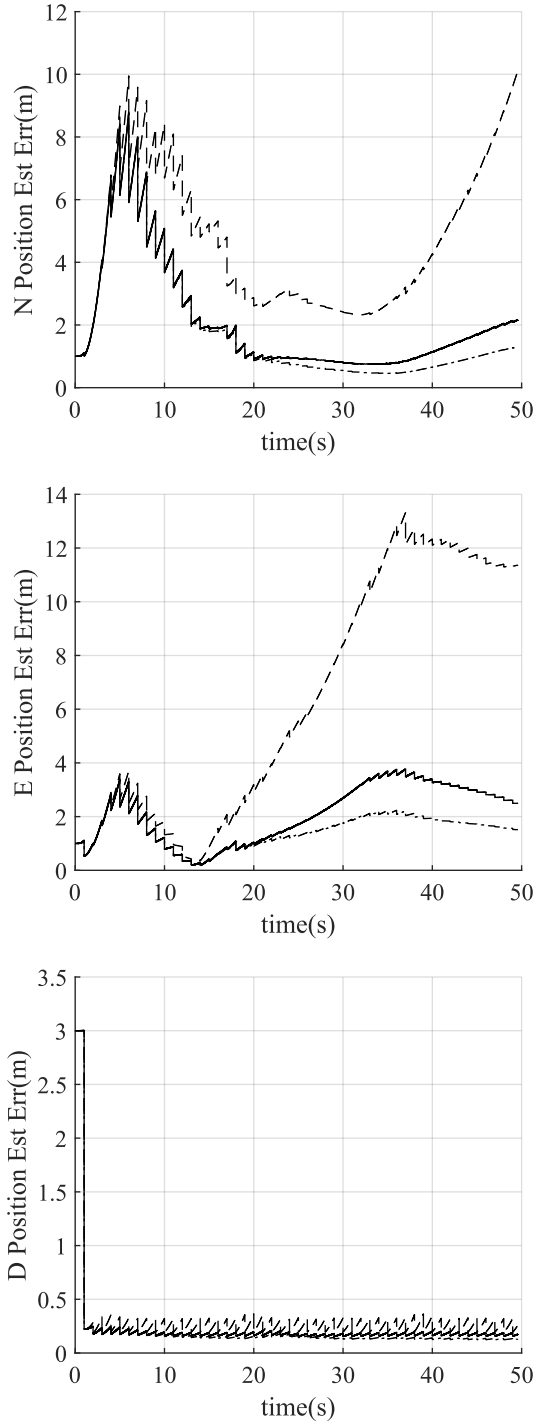

Fig. 3.8: Position estimation errors expressed as covariance bounds to illustrate IMU grade differences. From top to bottom: North position, east position, down position. By line type: Dashed line represents consumer grade, solid line represents tactical grade, and dot-dash line represents navigation grade.

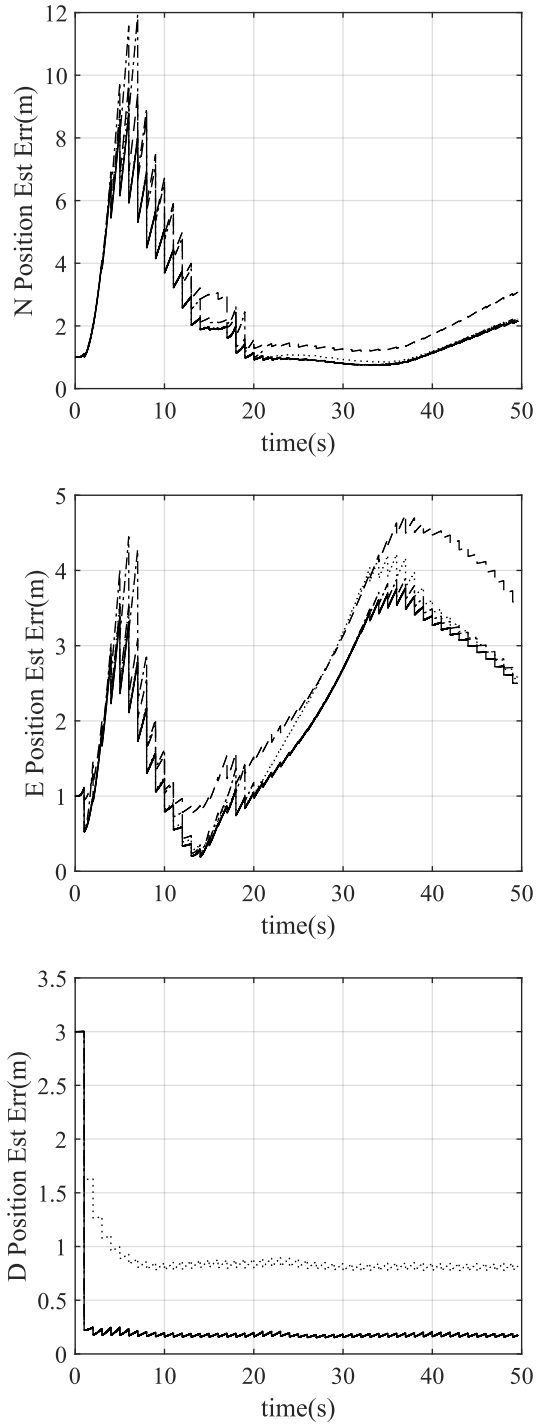

Fig. 3.9: Position estimation errors expressed as covariance bounds to illustrate measurement error differences. From top to bottom: North position, east position, down position. By line type: Dashed line represents increased range error, dot-dash line represents increased range-rate error, dotted line represents increased altitude error, and solid line represents no increased error.

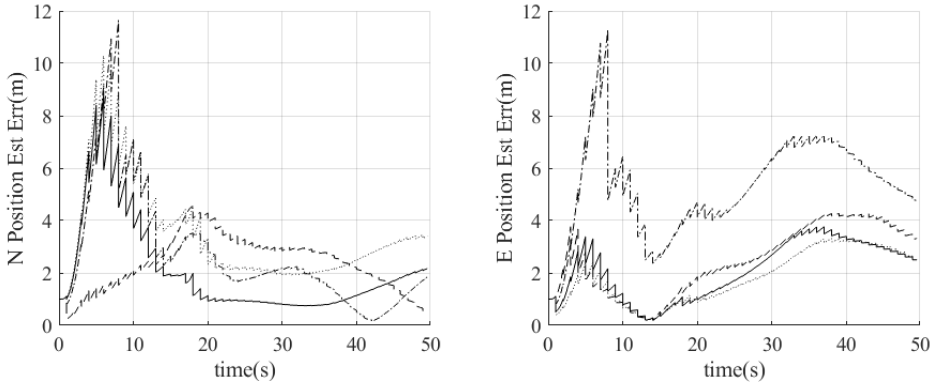

Fig. 3.10: Position estimation errors expressed as covariance bounds to illustrate ground target placement. From right to left: North position, east position. Line types: Dashed line for target at (500, 0, 0), dot-dash line for target at (500, 500, 0), solid line for target at (500, 1000, 0), and dotted line for target at (500, 1500, 0).

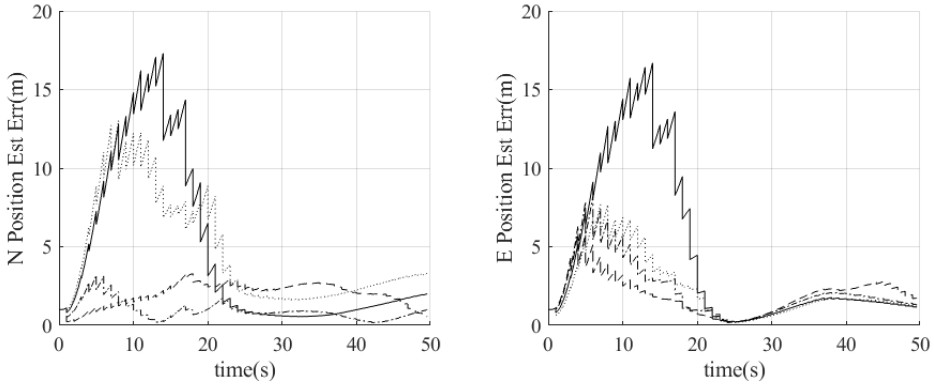

Fig. 3.11: Position estimation errors expressed as covariance bounds to illustrate ground target placement. From right to left: North position, east position. Line types: Dashed line for target at (1000, 0, 0), dot-dash line for target at (1000, 500, 0), solid line for target at (1000, 1000, 0), and dotted line for target at (1000, 1500, 0).

CHAPTER 4

SENSITIVITY OF BPA SAR IMAGE FORMATION TO INITIAL POSITION, VELOCITY, AND ATTITUDE NAVIGATION ERRORS

The Back-Projection Algorithm (BPA) is a time domain matched filtering technique to form synthetic aperture radar (SAR) images. To produce high quality BPA images, precise navigation data for the radar platform must be known. Any error in position, velocity, or attitude results in improperly formed images corrupted by shifting, blurring, and distortion. This paper develops analytical expressions that characterize the relationship between navigation errors and image formation errors. These analytical expressions are verified via simulated image formation and real data image formation.

4.1 Introduction

Synthetic aperture radar (SAR) is a class of radar processing that uses the flight path of a spacecraft or aircraft, referred to as a radar platform, to create a synthetic imaging aperture. Through a collection of matched filters, raw radar data is processed into images. Many efficient matched filtering algorithms have been developed that employ the frequency domain, such as the range-Doppler algorithm, the chirp scaling algorithm, the omega-K algorithm, and more [3]. Time domain algorithms also exist, such as the Back-Projection Algorithm (BPA) [15].

This paper explores the sensitivity of BPA images to navigation errors. This is done first analytically using the range equation and back-projection equation, which are both defined in Section 4.2. Secondly the analysis is verified by injecting error into a flight trajectory estimate of an aircraft and using the corrupted trajectory estimate to form BPA images. This process is performed on both simulated and real data.

4.1.1 Motivation

The research in this paper is primarily motivated by the field of GPS denied navigation but may be of interest to other fields relating to SAR image quality or image autofocusing. GPS denied navigation is a field of research that involves estimating the state of a vehicle in the absence of Global Navigation Satellite Systems (GNSS) such as GPS. Typical approaches utilize an inertial navigation system (INS) as the core sensor, aided by measurements from auxiliary sensors, in the framework of an extended Kalman filter. Such auxiliary sensors may include cameras, lidar, radar, etc, [16].

When forming a SAR image using back-projection, navigation data and raw radar data are processed to form an image. Obtaining precise navigation data in an ideal application requires the use of GPS. However, in a GPS denied environment, navigation errors may be present, which result in distorted SAR images. This research is motivated by the potential of inferring navigation errors from induced image errors during BPA image formation [17]. This paper works toward building the foundation and intuition needed to achieve such a potential.

4.1.2 Literature Review

BPA is more sensitive to navigation errors than other types of SAR image formation techniques. This can be inferred from Duersch and Long who explore some of the sensitivities inherent in forming images using back-projection [15]. This research expands the sensitivity analysis to motion errors as seen from a navigation point of view with a more complete navigation state.

BPA is essentially a matched filter along a hyperbolic curve within a set of range compressed data. Integrating along a curve requires that each data sample be precisely selected in correspondence with the current position of the vehicle. Any error in navigation data results in integrating data on an incorrect curve with an incorrect phase. Very precise navigation data is therefore necessary to form accurate BPA images [15]. Further details on BPA are discussed in Section 4.2.

Errors in navigation data manifest themselves in a SAR image as shifts and distortions

of a given target. Research performed by Christensen et al explores the effects of navigation errors on fully formed SAR images and hypothesizes that navigation errors can be determined by comparing degraded SAR images to a reference SAR map [17].

Many types of errors can affect the quality of SAR images. As such a comprehensive analysis of image errors is difficult and requires further investigation. Current efforts in analyzing image errors include research performed by Bamler [18] and Farrel et al [19]. They explore image errors caused by servo transients, quantization, range uncertainty, range-rate uncertainty, and focusing algorithm selection. Additionally, Chen explores image errors caused by moving targets in the illuminated scene [20].

In previous literature, navigation errors have been expressed as range displacement, line of sight displacement, and forward velocity error. Moreira and Xing et al adjust the SAR pulse repetition frequency (PRF) to compensate for forward velocity errors [21], [22]. Moreira further adjusts phase and range delays to compensate for line of sight displacement errors. Velocity errors in particular have been shown to affect the Doppler parameters of the SAR data, which cause target location errors and image degradation in the final image [22], [23].

4.1.3 Contributions

A comprehensive study of BPA SAR image errors in the context of the full navigation state has not been performed to date. The research seeks to fill this void by developing relationships between image shifts, blurs, and distortions and all components of navigation state, specifically position, velocity, and attitude errors.

Section 4.2 begins by providing necessary background knowledge concerning inertial navigation and BPA processing. Section 4.3 develops the math necessary to predict how navigation errors affect the final SAR image. Sections 4.4 and 4.5 demonstrate the application of the error analysis to simulated and real data, respectively. Section 4.6 provides concluding discussion and summary.

4.2 Background

4.2.1 Inertial Navigation

The purpose of this section is to define an inertial navigation framework applicable to the short data collection times typical of SAR imagery. The framework is then used to develop analytical expressions of position estimation error growth.

Inertial navigation is a large field with an equally-large body of literature dating back to the 1930's. An excellent overview of the history and motivating factors behind the development of this field is provided in [24]. The navigation framework developed in this section utilizes concepts discussed in [24–26]. The developed framework is most directly related to the so-called "Tangent Frame" kinematic model [25], with the assumptions of constant gravity and a non-rotating earth, both of which are applicable over the short time frame typical of an airborne SAR data collection. In the development that follows, the truth and navigation states are defined, with the associated differential equations. Consistent with an extended Kalman filter framework, the truth state differential equations are linearized about the estimated navigation state to derive the differential equations of the estimation errors, or error states.

The truth state vector comprises the true position ($\boldsymbol{p}^n$), velocity ($\boldsymbol{v}^n$), and attitude quaternion (q_b^n) of the vehicle

$$\boldsymbol{x} = \begin{bmatrix} \boldsymbol{p}^n & \boldsymbol{v}^n & q_b^n \end{bmatrix}^T \tag{4.1}$$

where n and b refer to the navigation and body frame, respectively. The body frame origin is coincident with the navigation center of the inertial measurement unit (IMU), with the axes aligned and rotating with the vehicle body axes. Out of convenience for the subsequent analysis, and without loss of generality, the navigation frame is defined with the x-axis parallel to the velocity of the vehicle, the z-axis in the direction of gravity, and the y-axis defined by the right-hand-rule. The x, y, and z axes, therefore, correspond to the along-track, cross-track, and down directions typical of radar imaging conventions. Consistent with Ferell's definition of the "Tangent Frame" [25], the position and velocity are defined relative to a fixed origin, whose location is the position of the vehicle at the beginning of the

SAR data collection. The differential equations of the truth states are defined as follows[1]

$$\begin{bmatrix} \dot{\boldsymbol{p}}^n \\ \dot{\boldsymbol{v}}^n \\ \dot{q}_b^n \end{bmatrix} = \begin{bmatrix} \boldsymbol{v}^n \\ T_b^n \boldsymbol{\nu}^b + \boldsymbol{g}^n \\ \frac{1}{2} q_b^n \otimes \begin{bmatrix} 0 \\ \boldsymbol{\omega}^b \end{bmatrix} \end{bmatrix} \tag{4.2}$$

The strapdown inertial navigation system comprises a three-axis accelerometer and gyro, which provide measurements of specific force $\left(\tilde{\boldsymbol{\nu}}^b\right)$ and angular rate $\left(\tilde{\boldsymbol{\omega}}^b\right)$ in the body frame, corrupted by noise

$$\begin{bmatrix} \tilde{\boldsymbol{\nu}}^b \\ \tilde{\boldsymbol{\omega}}^b \end{bmatrix} = \begin{bmatrix} \boldsymbol{\nu}^b \\ \boldsymbol{\omega}^b \end{bmatrix} + \begin{bmatrix} \boldsymbol{n}_\nu \\ \boldsymbol{n}_\omega \end{bmatrix} \tag{4.3}$$

The navigation states are defined identical to the truth states but are propagated using noisy accelerometer and gyro measurements

$$\begin{bmatrix} \dot{\hat{\boldsymbol{p}}}^n \\ \dot{\hat{\boldsymbol{v}}}^n \\ \dot{\hat{q}}_b^n \end{bmatrix} = \begin{bmatrix} \hat{\boldsymbol{v}}^n \\ \hat{T}_b^n \tilde{\boldsymbol{\nu}}^b + \boldsymbol{g}^n \\ \frac{1}{2} \hat{q}_b^n \otimes \begin{bmatrix} 0 \\ \tilde{\boldsymbol{\omega}}^b \end{bmatrix} \end{bmatrix} \tag{4.4}$$

The estimation error, or error state vector,

$$\delta \boldsymbol{x} = \begin{bmatrix} \delta \boldsymbol{p}^n & \delta \boldsymbol{v}^n & \delta \boldsymbol{\theta}^n \end{bmatrix}^T \tag{4.5}$$

is defined as the difference between the truth states and the navigation states. For all but the attitude states, the difference is defined by a simple subtraction. For the attitude quaternion the difference is defined by a quaternion product.

$$\delta \boldsymbol{p}^n = \boldsymbol{p}^n - \hat{\boldsymbol{p}}^n \tag{4.6}$$

[1] In this work, the quaternion is interpreted as a "left-handed" quaternion, and the $\otimes$ operator is the Hamiltonian quaternion product [27].

$$\delta \boldsymbol{v}^n = \boldsymbol{v}^n - \hat{\boldsymbol{v}}^n \tag{4.7}$$

$$\begin{bmatrix} 1 \\ -\frac{1}{2}\delta\boldsymbol{\theta}^n \end{bmatrix} = q_b^n \otimes (\hat{q}_b^n)^* \tag{4.8}$$

It is also convenient to define the attitude errors in terms of the true and estimated transformation matrices

$$[I - (\delta\boldsymbol{\theta}^n \times)] = T_b^n \left(\hat{T}_b^n\right)^T \tag{4.9}$$

Linearization of (4.2) about the estimated state results in the error state differential equation

$$\delta\dot{\boldsymbol{x}} = F\delta\boldsymbol{x} + B\boldsymbol{w} \tag{4.10}$$

where the state dynamics matrix, F, and noise coupling matrix, B, are defined respectively as

$$F = \begin{bmatrix} 0_{3\times3} & I_{3\times3} & 0_{3\times3} \\ 0_{3\times3} & 0_{3\times3} & \left[\hat{T}_b^n \tilde{\boldsymbol{\nu}}^b\right] \times \\ 0_{3\times3} & 0_{3\times3} & 0_{3\times3} \end{bmatrix} \tag{4.11}$$

$$B = \begin{bmatrix} 0_{3\times3} & 0_{3\times3} \\ -\hat{T}_b^n & 0_{3\times3} \\ 0_{3\times3} & \hat{T}_b^n \end{bmatrix} \tag{4.12}$$

and where the white noise ($\boldsymbol{w}$) consists of the accelerometer and gyro measurement noise

$$\boldsymbol{w} = \begin{bmatrix} \boldsymbol{n}_\nu & \boldsymbol{n}_\omega \end{bmatrix}^T \tag{4.13}$$

The focus of this paper is to analyze the sensitivity of the BPA image to errors in position, velocity, and attitude at the beginning of the synthetic aperture. The effect of $\boldsymbol{w}$ is therefore ignored, and the analysis is facilitated by determining the homogenous solution to (4.10)

$$\delta\boldsymbol{x}_k = \Phi\left(t_k, t_{k-1}\right)\delta\boldsymbol{x}_{k-1} \tag{4.14}$$

where $\Phi(t_k, t_{k-1})$ is the state transition matrix (STM) from the t_{k-1} to t_k. The STM is defined as the matrix which satisfies the differential equation and initial condition

$$\dot{\Phi}(t_{k+1}, t_k) = F(t)\,\Phi(t_{k+1}, t_k) \tag{4.15}$$

$$\Phi(t_k, t_k) = I_{n\times n} \tag{4.16}$$

For the case of straight-and-level flight, the dynamic coupling matrix of (4.11) is constant,

$$F = \begin{bmatrix} 0_{3\times3} & I_{3\times3} & 0_{3\times3} \\ 0_{3\times3} & 0_{3\times3} & (\boldsymbol{\nu}^n)\times \\ 0_{3\times3} & 0_{3\times3} & 0_{3\times3} \end{bmatrix} \tag{4.17}$$

Where the accelerometer measurements are expressed in the n frame as

$$\boldsymbol{\nu}^n = \begin{bmatrix} 0 & 0 & -g \end{bmatrix}^T \tag{4.18}$$

Since F is constant, the STM is derived using the matrix exponential ([4], page 42)

$$\Phi(t_{k+1}, t_k) = \begin{bmatrix} I_{3\times3} & I_{3\times3}\Delta t & (\boldsymbol{\nu}^n\times)\,\frac{\Delta t^2}{2!} \\ 0_{3\times3} & I_{3\times3} & (\boldsymbol{\nu}^n)\times\Delta t \\ 0_{3\times3} & 0_{3\times3} & I_{3\times3} \end{bmatrix} \tag{4.19}$$

The desired analytical expression for position errors is obtained from the first row of the STM to yield

$$\delta\boldsymbol{p}^n(t) = \delta\boldsymbol{p}_0^n + \delta\boldsymbol{v}_0^n\Delta t + \boldsymbol{\nu}^n\times\delta\boldsymbol{\theta}_0^n\frac{\Delta t^2}{2} \tag{4.20}$$

In all subsequent sections, the variables representing positions, velocities, and attitudes are all assumed to be in the n frame. As such, the n superscript on all navigation states is omitted for notational brevity.

4.2.2 Back-Projection Algorithm

Forming images using SAR is a process of matched filtering that transformed raw returned radar signals into focused pixels. A raw SAR signal is typically a linear frequency modulated (FM), or "chirp", signal. Chirp signals are a sinusoid-like signal with an instantaneous frequency that is linear with time. A transmitted chirp signal is denoted $s_{tx}(t)$ and is equal to

$$s_{tx}(t) = \begin{cases} \exp(j2\pi f_0 t + j\pi K t^2), & 0 \leq t \leq T \\ 0, & \text{otherwise} \end{cases} \tag{4.21}$$

where f_0 is the initial frequency, K is the linear FM rate in hertz per second, and T is the pulse duration.

The chirp signal is transmitted several times along the trajectory, and return signals are collected for each transmitted signal. Using a "stop and hop" approximation, the return radar signal is a time shifted, attenuated version of the transmitted signal given by

$$s_{rx}(t) = A s_{tx}(t - \tau) \tag{4.22}$$

The return signal is fed through a matched filter in a process called "range compression". The matched filter is a time reversed, conjugate version of the transmitted signal $s_{tx}(t)$. The output of the matched filter is denoted $s_{out}(t)$ and is equal to the convolution of $s_{rx}(t)$ with $s^*_{tx}(T - t)$.

$$\begin{aligned} s_{out}(t) &= s_{rx}(t) * s^*_{tx}(T - t) \\ &= \begin{cases} \int_0^t s_{rx}(\lambda) s^*_{tx}(T - (t - \lambda)) d\lambda, & 0 \leq t \leq T \\ \int_{t-T}^T s_{rx}(\lambda) s^*_{tx}(T - (t - \lambda)) d\lambda, & T \leq t \leq 2T \end{cases} \end{aligned} \tag{4.23}$$

Evaluating the convolution results in

$$s_{out}(t) = e^{-j\rho(2\pi f_0 + \pi KT)} \begin{cases} \frac{\sin(\pi K\rho t)}{\pi K\rho}, & 0 \leq t < T \\ T, & t = T \\ \frac{\sin(\pi K\rho(2T-t))}{\pi K\rho}, & T < t \leq 2T \end{cases} \tag{4.24}$$

where $\rho = T - t$. This expression can be written in a closed form using the sinc function $\text{sinc}(x) = \sin(\pi x)/\pi x$.

$$s_{out}(t) = e^{-j\rho(2\pi f_0 + \pi KT)} \xi \text{sinc}(K\rho\xi) \tag{4.25}$$

where ξ is equal to $T - |t - T|$.

After range compression, the sequential returns from a single target form a hyperbolic curve in the range compressed data. This hyperbola is quantified via the range equation denoted $R(\boldsymbol{p}_t, \eta)$ and defined as

$$R(\boldsymbol{p}_t, \eta) = \|\boldsymbol{p}_t - \boldsymbol{p}(\eta)\| \tag{4.26}$$

where $\boldsymbol{p}_t$ is the position of a target of the ground and $\boldsymbol{p}$ is the true time-varying position of the aircraft from (4.1). The aircraft position varies with azimuth time (or slow time), η.

To form an image using BPA, a second matched filter is applied to the range compressed data in the azimuth direction. This is called "azimuth compression". Azimuth compression using BPA is performed in the time domain and is dependent on the range equation, which is dependent on the position of the radar vehicle. For a particular pixel location, $\boldsymbol{p}_{pix}$, azimuth compression is defined by the summation,

$$A(\boldsymbol{p}_{pix}) = \sum_k s_{out}(t_{pix,k}) \text{exp}\left\{ j4\pi \frac{R_k(\boldsymbol{p}_{pix}, \eta)}{\lambda} \right\} \tag{4.27}$$

where k is used to denote the k^{th} range compressed signal, λ is the wavelength at the center frequency of the chirp signal, and $t_{pix,k}$ is the time during the k^{th} range compressed signal

at which $R_k(\boldsymbol{p}_t, \eta) = R_k(\boldsymbol{p}_{pix}, \eta)$. This time can be calculated via the conversion,

$$t_{pix} = 2R_k(\boldsymbol{p}_{pix}, \eta)/c \tag{4.28}$$

where c is the speed of light. To go from t_{pix} to $t_{pix,k}$, an index in the k^{th} range compressed pulse must be found that corresponds with time t_{pix}. Forming a BPA image is a matter of performing azimuth compression for a collection of pixels within some chosen geographical region.

4.3 Analysis

Errors in the estimated trajectory cause errors in the range equation (4.26), which in turn cause errors in the back-projection equation (4.27). The range equation appears in two places in the back-projection equation, namely the index of the range compressed data and the phase of the matched filter. As such, an error in the range equation causes two types of errors.

First, an error in the index of the range compressed data appears as a change in the hyperbolic curve that (4.27) uses to perform azimuth compression. Changes in the chosen curve relative to the correct curve manifest as shifts, eccentricity changes, and distortions. These errors are referred to as "curve errors". Second, an error appears in the phase of the matched filter. This affects the focus of a target in the final image through a phase mismatch. Phase mismatches lead to target blurring. These errors are referred to as "phase errors".

Curve errors and phase errors are explored individually for position, velocity, and attitude navigation errors. Intuition for each type of error is aided by first expanding (4.26) using a Taylor series approximation. For conciseness, the notation for (4.26) is abbreviated to $R(\eta)$. According to [3], the Taylor approximation for the range equation, denoted $\tilde{R}(\eta)$, is approximated as

$$\tilde{R}(\eta) \approx R_0 + \frac{d^2 \left\|R(\eta)\right\|^2}{d\eta^2}\bigg|_{\eta=\eta_0} \frac{1}{2R_0}(\eta - \eta_0)^2 \tag{4.29}$$

where η_0 is the time of closest approach and R_0 is the range of closest approach, which is also equal to $R(\eta_0)$. As a common practice in literature, this approximation is expanded about the time of closest approach η_0. By doing so, the first order term of the expansion equals zero.

The navigation frame is chosen such that the initial position of the radar platform is the origin. This origin can be interpreted globally as the point of GPS denial or locally as the beginning of the synthetic aperture. The platform is assumed to be flying at a constant velocity. For ease of visualization in subsequent figures, the radar platform is assumed to be flying northward. In this scenario, the true time-varying position of the platform is expressed simply as

$$\boldsymbol{p}(\eta) = \boldsymbol{v}_0 \eta \tag{4.30}$$

where $\boldsymbol{v}_0$ is the true initial velocity . In (4.26), the time-varying range is expressed in terms of the truth state. Error analysis is performed by replacing the truth state with the estimated navigation state. Then (4.6) is used to write the navigation state as the difference between the truth state and error state. This is expressed as

$$\hat{R}(\eta) = \|\boldsymbol{p}_t - (\boldsymbol{p}(\eta) - \delta\boldsymbol{p})\| \tag{4.31}$$

where the hat on $\hat{R}(\eta)$ distinguishes this value as an estimate rather than the true value. This construction allows for an intuitive analysis of the back-projection equation with the help of the Taylor approximation from (4.29), for the cases of position, velocity, attitude errors at the beginning of the synthetic aperture.

4.3.1 Position Errors

Using (4.20), an initial position estimation error, denoted $\delta\boldsymbol{p}_0$, is introduced into the estimated range equation.

$$\hat{R}(\eta) = \|\boldsymbol{p}_t - \boldsymbol{v}_0\eta + \delta\boldsymbol{p}_0\| \tag{4.32}$$

This equation is then expanded using the Taylor approximation, again denoted with a tilde.

$$\begin{aligned}\hat{\tilde{R}}(\eta) = &\|\boldsymbol{p}_t - \boldsymbol{v}_0\eta_0 + \delta\boldsymbol{p}_0\| \\ &+ \frac{(\boldsymbol{v}_0)^T\boldsymbol{v}_0}{2\|\boldsymbol{p}_t - \boldsymbol{v}_0\eta_0 + \delta\boldsymbol{p}_0\|}(\eta - \eta_0)^2\end{aligned} \tag{4.33}$$

In the first term of the expansion, $\delta\boldsymbol{p}_0$ causes a constant shift of the hyperbola used for azimuth compression. In the second term, $\delta\boldsymbol{p}_0$ in the denominator is typically small compared $\boldsymbol{p}_t - \boldsymbol{v}_0\eta_0$. As such, its contribution to the overall error is very small and can be ignored. In terms of curve errors, the estimated hyperbola is shifted in the direction of $\delta\boldsymbol{p}_0$ due to the first term of the expansion. For phase errors, constant offsets do not affect the overall focus of any imaged target [3]. Phase offsets only affect knowledge of absolute phase.

The notional effects of position errors are illustrated in Figures 4.1, 4.2, and 4.3. Each figure is split into three subfigures showing how a position error propagates through different stages of radar processing. The first subfigure shows the error's effect on the flight trajectory. The second subfigure shows the error's effect on the range compressed data. The third subfigure shows the error's effect on the final image.

In each figure, light colored or dotted illustrations represent expected data given estimation errors. Solid black illustrations represent actual data given no estimation errors. These figures primarily provide intuition primarily on curve errors but can be useful in visualizing phase errors as well.

4.3.2 Velocity Errors

From (4.20), an initial velocity estimation error is introduced into the estimated range equation as

$$\hat{R}(\eta) = \|\boldsymbol{p}_t - (\boldsymbol{v}_0 - \delta\boldsymbol{v}_0)\eta\| \tag{4.34}$$

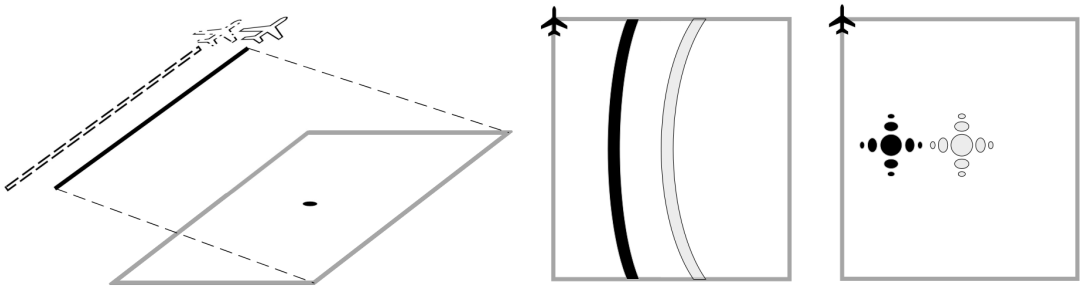

Fig. 4.1: Illustration of how cross track position errors affect the various stages of radar processing. Left: flight trajectory with error. Center: range compressed data with error. Right: final image with error. Light colored or dotted illustrations represent expected data given estimation errors. Solid black illustrations represent truth data.

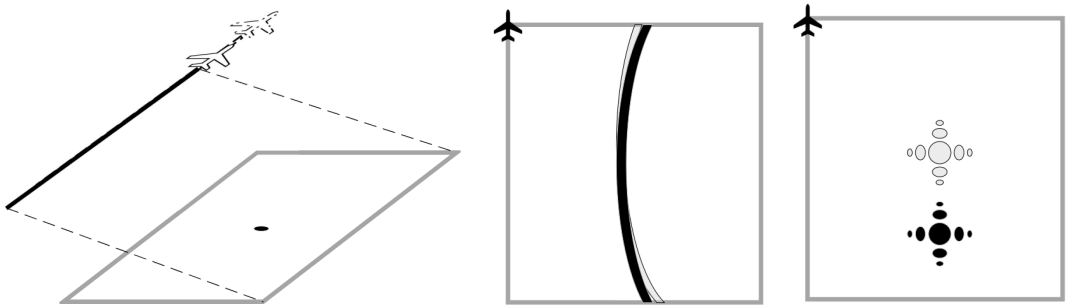

Fig. 4.2: Illustration of how along track position errors affect the various stages of radar processing. Left: flight trajectory with error. Center: range compressed data with error. Right: final image with error. Light colored or dotted illustrations represent expected data given estimation errors. Solid black illustrations represent truth data.

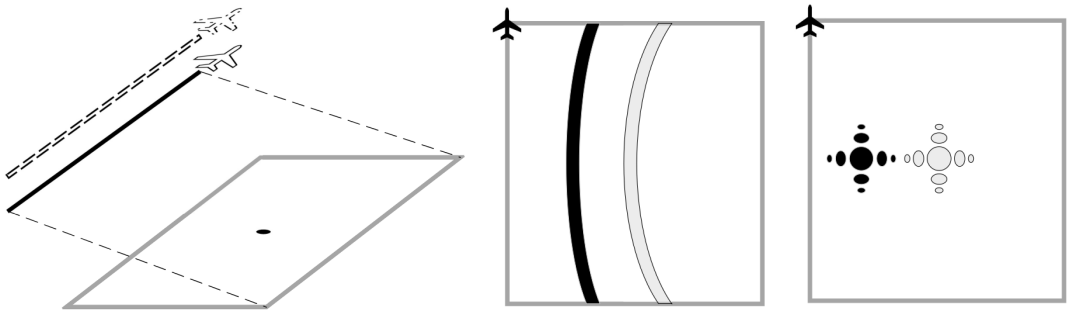

Fig. 4.3: Illustration of how elevation position errors affect the various stages of radar processing. Left: flight trajectory with error. Center: range compressed data with error. Right: final image with error. Light colored or dotted illustrations represent expected data given estimation errors. Solid black illustrations represent truth data.

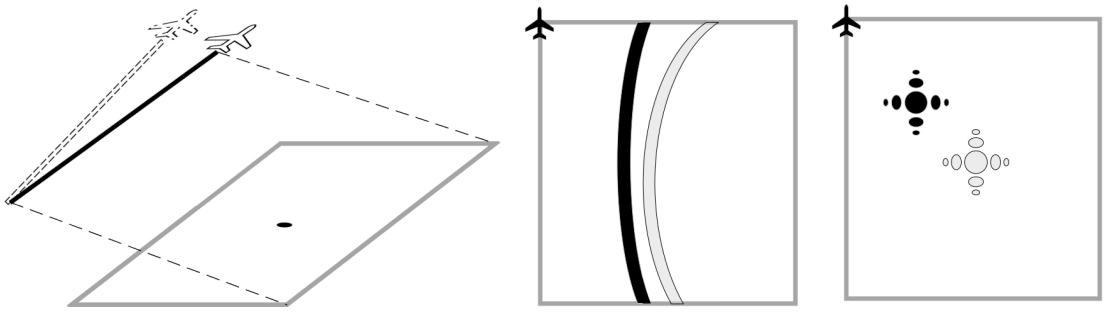

Fig. 4.4: Illustration of how cross track velocity errors affect the various stages of radar processing. Left: flight trajectory with error. Center: range compressed data with error. Right: final image with error. Light colored or dotted illustrations represent expected data given estimation errors. Solid black illustrations represent truth data.

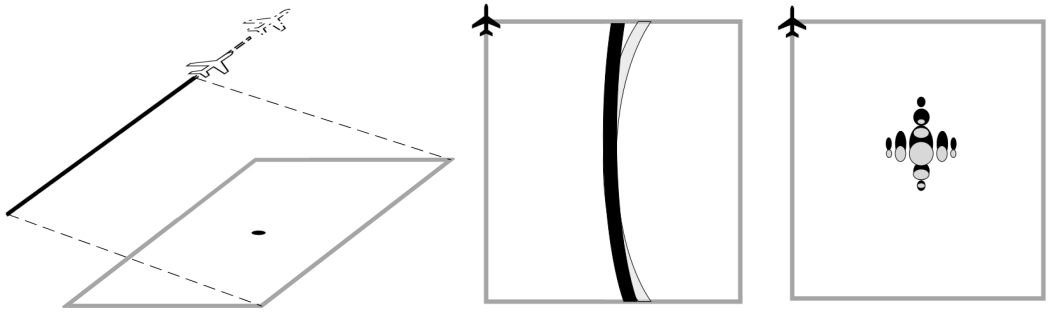

Fig. 4.5: Illustration of how along track velocity errors affect the various stages of radar processing. Left: flight trajectory with error. Center: range compressed data with error. Right: final image with error. Light colored or dotted illustrations represent expected data given estimation errors. Solid black illustrations represent truth data.

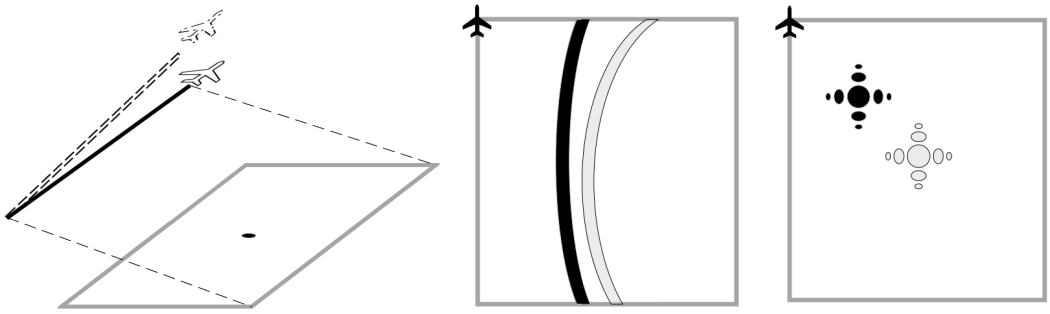

Fig. 4.6: Illustration of how elevation velocity errors affect the various stages of radar processing. Left: flight trajectory with error. Center: range compressed data with error. Right: final image with error. Light colored or dotted illustrations represent expected data given estimation errors. Solid black illustrations represent truth data.

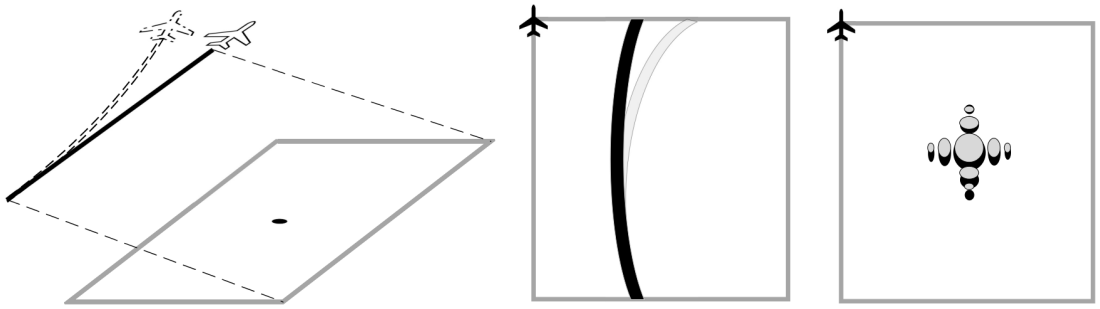

Fig. 4.7: Progression of roll errors through the SAR data. Left: flight trajectory with error. Center: range compressed data with error. Right: final image with error. Light colored or dotted illustrations represent expected data given estimation errors. Solid black illustrations represent truth data.

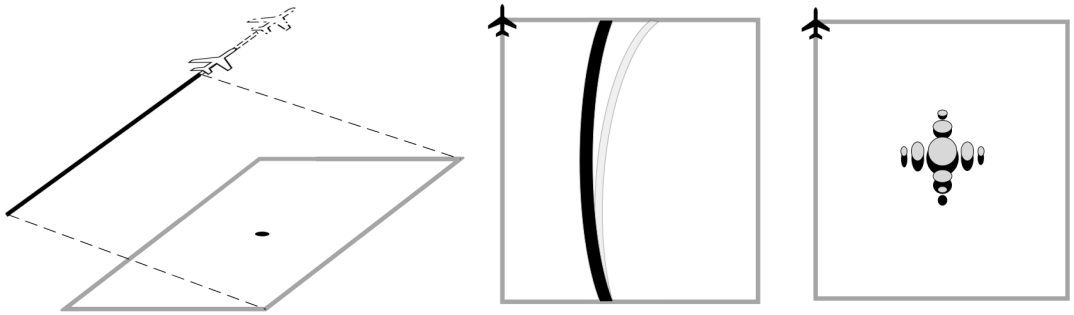

Fig. 4.8: Progression of pitch error through the SAR data. Left: flight trajectory with error. Center: range compressed data with error. Right: final image with error. Light colored or dotted illustrations represent expected data given estimation errors. Solid black illustrations represent truth data.

Again, the Taylor expansion is taken and results in

$$\hat{\hat{R}}(\eta) = \|\boldsymbol{p}_t - (\boldsymbol{v}_0 - \delta\boldsymbol{v}_0)\eta_0\| + \frac{(\boldsymbol{v}_0)^T\boldsymbol{v}_0 - 2(\boldsymbol{v}_0)^T\delta\boldsymbol{v}_0 + (\delta\boldsymbol{v}_0)^T\delta\boldsymbol{v}_0}{\|\boldsymbol{p}_t - (\boldsymbol{v}_0 - \delta\boldsymbol{v}_0)\eta_0\|}(\eta - \eta_0)^2 \tag{4.35}$$

In the first term of the expansion, there is again a constant offset due to $\delta\boldsymbol{v}_0$. As is the case for initial position errors, this constant offset causes a shifted curve error and a negligible offset phase error. In the second term of the expansion, $(\delta\boldsymbol{v}_0)^T\delta\boldsymbol{v}_0$ in the numerator is a quadratic error term and contribute little overall error. Similar to the case of position errors, the $\delta\boldsymbol{v}_0\eta$ term in the denominator contributes negligible overall error due to its relative size compared to the rest of the denominator.

In the numerator of the second term, $2(\boldsymbol{v}_0)^T\delta\boldsymbol{v}_0$ causes a time-varying error. In terms of curve errors, this changes the eccentricity of the expected hyperbola in the range compressed data. For phase errors, this term can be thought of a linearly changing frequency error or azimuth FM rate error.

An azimuth FM rate error is characterized by a phase that changes quadratically in time. A quadratically varying phase yields a linearly changing instantaneous frequency. This is similar to the linear FM signal modeled by equation (4.21). For both curve errors and phase errors, the second numerator term results in blurring of the imaged target in the azimuth dimension. This blur is only present in along track errors, as cross track and elevation errors result in a $\delta\boldsymbol{v}_0$ that is orthogonal to $\boldsymbol{v}_0$.

Again, the notional effects are illustrated in Figures 4.4, 4.5, and 4.6 for various stages of SAR processing. Each figure is again split into three subfigures with identical interpretations as Figures 4.1, 4.2, and 4.3.

4.3.3 Attitude Errors

Again using (4.20), initial attitude errors are injected into the range equation to yield

$$\hat{R}(\eta) = \left\| \boldsymbol{p}_t - \boldsymbol{v}_0\eta + \boldsymbol{\nu}^n \times \delta\boldsymbol{\theta}_0 \frac{\eta^2}{2} \right\| \tag{4.36}$$

Errors in attitude manifest as errors in acceleration. Specific effects from attitude errors are apparent after computing the cross product. Using constant accelerometer measurements,

$$\boldsymbol{\nu}^n \times \delta\boldsymbol{\theta}_0 = \begin{bmatrix} 0 \\ 0 \\ -g \end{bmatrix} \times \begin{bmatrix} \delta\theta_{x,0} \\ \delta\theta_{y,0} \\ \delta\theta_{z,0} \end{bmatrix} = \begin{bmatrix} \delta\theta_{y,0} g \\ -\delta\theta_{x,0} g \\ 0 \end{bmatrix} \tag{4.37}$$

This equation illustrates how attitude errors only cause acceleration errors in the along track and cross track directions. Specifically, errors in roll, $\delta\theta_{x,0}$, cause cross track acceleration errors. Errors in pitch, $\delta\theta_{y,0}$, cause along track acceleration errors. Errors in yaw do not cause any errors in acceleration.

For conciseness, acceleration errors resulting from (4.37) are collectively referred to as $\delta\dot{\boldsymbol{v}}_0$. As such, the estimated range equation takes the form

$$\hat{R}(\eta) = \left\| \boldsymbol{p}_t - \boldsymbol{v}_0\eta + \frac{1}{2}\delta\dot{\boldsymbol{v}}_0\eta^2 \right\| \tag{4.38}$$

The effects of acceleration errors are again explored using the Taylor approximation of the estimated range equation.

$$\begin{aligned} \hat{\hat{R}}(\eta) = &\left\| \boldsymbol{p}_t - \boldsymbol{v}_0\eta_0 + \frac{1}{2}\delta\dot{\boldsymbol{v}}_0\eta_0^2 \right\| \\ &+ \frac{Q}{\left\| \boldsymbol{p}_t - \boldsymbol{v}_0\eta_0 + \frac{1}{2}\delta\dot{\boldsymbol{v}}_0\eta_0^2 \right\|}(\eta - \eta_0)^2 \end{aligned} \tag{4.39}$$

where

$$\begin{aligned} Q = &1.5(\delta\dot{\boldsymbol{v}}_0)^T\delta\dot{\boldsymbol{v}}_0\eta_0^2 - 3(\delta\dot{\boldsymbol{v}}_0)^T\boldsymbol{v}_0\eta_0 \\ &+ \boldsymbol{p}_t^T\delta\dot{\boldsymbol{v}}_0 + (\boldsymbol{v}_0)^T\boldsymbol{v}_0 \end{aligned} \tag{4.40}$$

In the first term of the expansion, $\frac{1}{2}\delta\dot{\boldsymbol{v}}_0\eta_0^2$ causes a constant offset. For curve errors, this term causes a small shift in the imaged target. In practice, this shift isn't strongly apparent, because the image degrades due to other terms before the shifting becomes strong. For phase

errors, this constant offset doesn't affect the focus of the image.

In the second term of the expansion, $1.5(\delta\dot{\boldsymbol{v}}_0)^T\delta\dot{\boldsymbol{v}}_0$ is a quadratic error term and is considered very small. The $\frac{1}{2}\delta\dot{\boldsymbol{v}}_0\eta_0^2$ term in the denominator is small compared to other terms in the denominator and causes negligible overall error. The $\boldsymbol{p}_t^T\delta\dot{\boldsymbol{v}}_0$ in the numerator causes a time-varying error. Interestingly, this error is in terms of the target location implying that the location of the target affects the severity of attitude imaging error. For both curve and phase errors, this term causes blurring similar to the along track velocity errors.

The $3(\delta\dot{\boldsymbol{v}}_0)^T\boldsymbol{v}_0\eta_0$ term also causes a time-varying error. For both curve and phase errors, this again results in blurring; however, this term only becomes significant for along track acceleration errors. This term is negligible for cross track and elevation errors due to orthogonality. Note that this term is dependent on the time of closest approach and therefore changes depending on the location of the target in azimuth.

Notional illustrations of how attitude errors propagate through the SAR processing steps are shown in Figures 4.7 and 4.8. It was shown that yaw errors do not affect SAR images, therefore these figures depict only roll and pitch errors. Each figure is split into subfigures with interpretations identical to those of the position and velocity error figures.

4.4 Simulated Data

The analysis presented in the previous section is now verified via simulation. SAR images are first formed using the true trajectory. Initial errors are then injected and propagated to yield a corrupted estimate of the trajectory. Images are formed with estimation errors and are compared to the truth reference image. The presence and extent of shifting and blurring, as predicted by the development of section 4.3, is also verified.

For each navigation error, a figure is presented with a simulated SAR image superimposed with the predicted target shift. The reference image to which each SAR chip should be compared is provided in Figure 4.9.

The SAR images formed given estimation errors are provided in Figures 4.11, 4.12, and 4.13. For each image, a superimposed "X" shows the location of the reference target

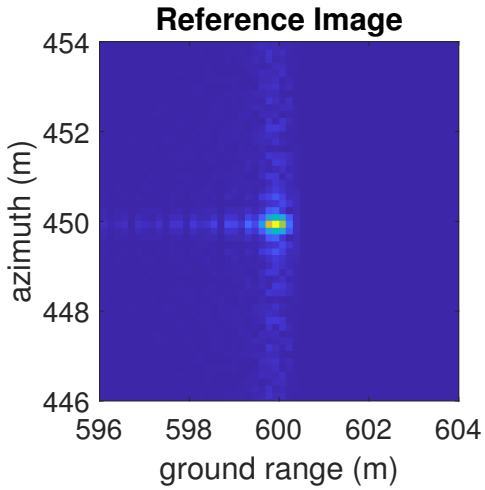

Fig. 4.9: Reference image for simulated SAR data.

in relation to the current image. A superimposed "O" shows the predicted location of the target given the injected estimation errors.

The "X" and "O" are generated using the true range equation, (4.26), and the estimated range equation, (4.31), respectively. Equation (4.26) is used to find the true range of closest approach and time of closest approach, denoted R_0 and η_0. Equation (4.31) is used to find the estimated range of closest approach and time of closest approach, denoted $\hat{R}_0$ and $\hat{\eta}_0$.

$$R_0 = \min R(\eta), \quad \hat{R}_0 = \min \hat{R}(\eta) \tag{4.41}$$
$$\eta_0 = \arg\min_{\eta} R(\eta), \quad \hat{\eta}_0 = \arg\min_{\eta} \hat{R}(\eta)$$

The range of closest approach and time of closest approach are used as coordinates to overlay "X" and "O" onto each image.

Figures 4.11-4.13 illustrate that in all cases, the direction of shifts and blurs is consistent with the development of section 4.3. Furthermore, in cases where blur is negligible, the amount of shift is accurately predicted utilizing the method described previously. It is important to highlight the ambiguity that exists in relating the SAR image error with the attributing navigation error. From a single image, for example, it is impossible isolate the effects of cross track position and elevation errors, since both cause shifts in the cross track

position of the target. Similar difficulties existing in attributing along-track shifts and blurs to the corresponding navigation errors.

4.5 Real Data

The analysis from Section 4.3 is be further verified using real SAR data. Radar data was collected in Logan, Utah. SAR images are formed using a post-processed, high fidelity navigation solution, which is considered truth for the purposes of this research. The reference image in Figure 4.10 is formed using the truth trajectory. Each type of navigation error is then injected into the truth trajectory, from which the distorted SAR images of Figures 4.14-4.16 are formed.

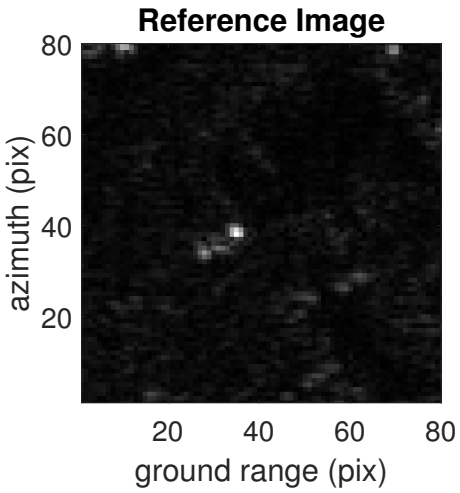

Fig. 4.10: Reference image for real SAR data.

The results on real SAR data mirror the trends observed in section 4.4. The type and direction of the shifts and blurs are consistent with the predictions of section 4.3. In the case of negligible blurs, the shifts on real data are accurately predicted using the method described in section 4.4 for all cases except yaw error, where a very small prediction error is observed. Finally, ambiguity in the attribution of error sources to image errors is observed in the real SAR data. Despite the small discrepancy in yaw, these results serve to further validate the relationships developed in section 4.3.

4.6 Conclusion

This paper analyzes errors in the formation of SAR images using the Back-Projection Algorithm from a navigation perspective, for the case of straight-and-level flight. Relationships are developed between the position, velocity, and attitude estimation errors at the beginning of the synthetic aperture and the observed shifts and blurs of the corrupted BPA SAR image.

The developed relationships were observed and validated on both simulated and real SAR data. In the case of negligible blurring, the location of the target in the corrupted SAR image is accurately predicted given knowledge of the attributing navigation error. These results suggest that errors in BPA SAR images could potentially be used in reverse, i.e. image errors could be characterized and exploited as a navigation aid in GPS-denied applications. For a single image, however, it was observed that the shifts/blurs are not unique to an individual navigation error. The presence of the target location in the developed relationships suggests that the effect of navigation errors can be modified by the selection of the target location. One obvious extension of this work is the consideration of multiple targets with large geometric diversity, to resolve the ambiguity in attributing error sources. Furthermore, methods which characterize the amount and direction of image blurring must be developed to exploit the information contained therein.

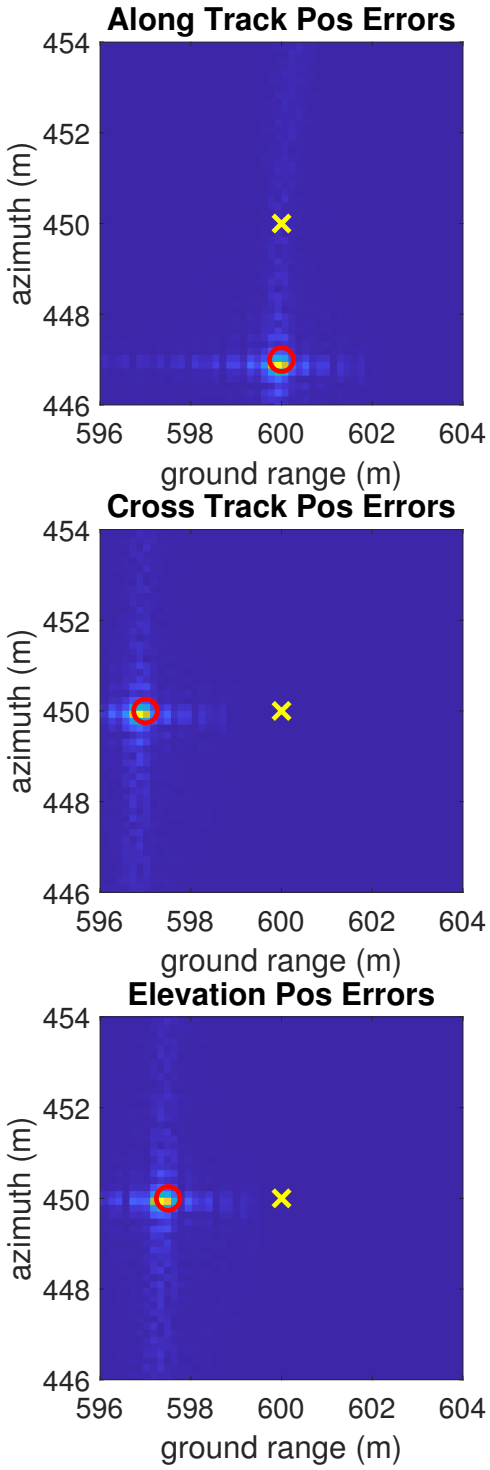

Fig. 4.11: Position errors in simulated data: Top, along track position error (3 m). Middle, cross track position error (3 m). Bottom, elevation position error (3 m). Each figure is superimposed with a reference target location, "X", and a predicted target shift, "O".

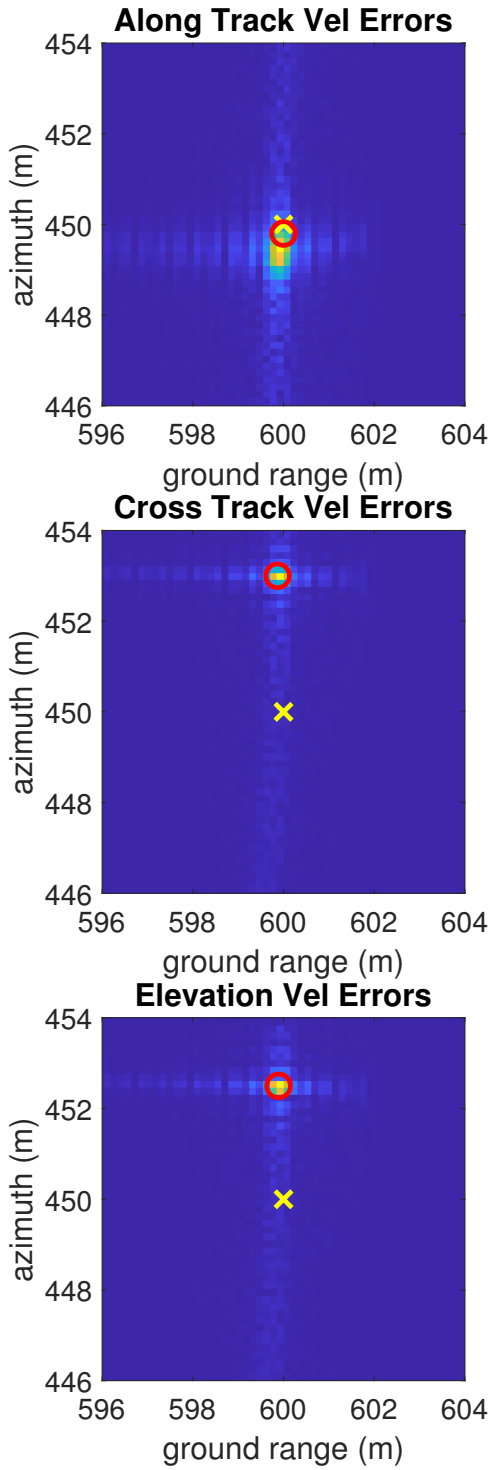

Fig. 4.12: Velocity errors in simulated data: Top, along track velocity error (0.1 m/s). Middle, cross track velocity error (0.05 m/s). Bottom, elevation velocity error (0.05 m/s). Each figure is superimposed with a reference target location, "X", and a predicted target shift, "O".

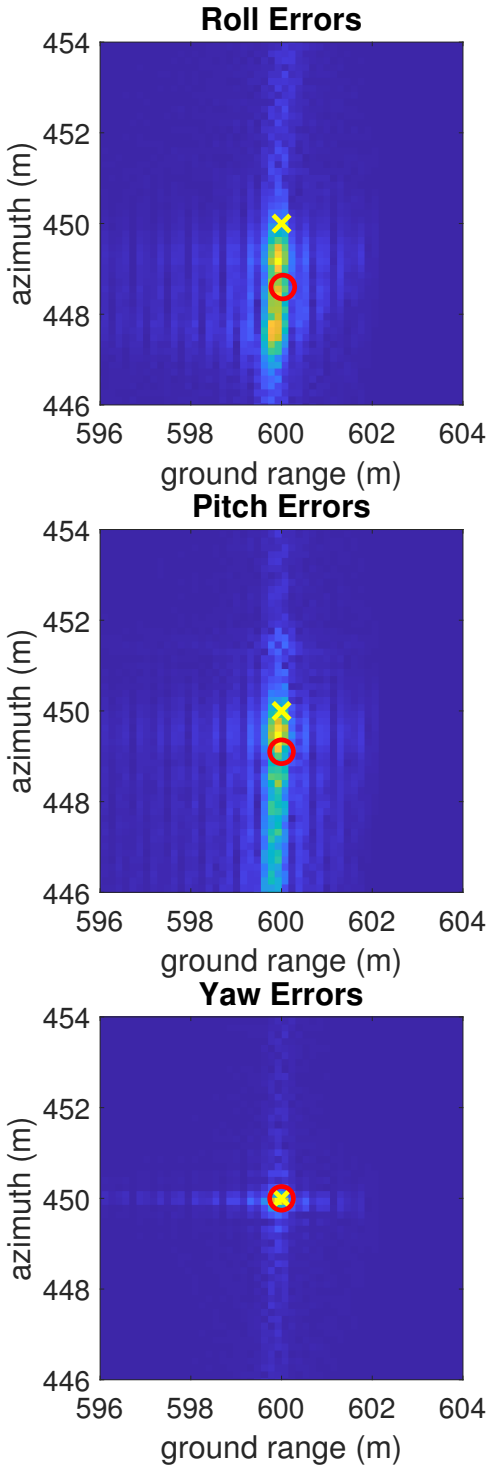

Fig. 4.13: Attitude errors in simulated data: Top, roll error (0.001 rad). Middle, pitch error (0.02 rad). Bottom, yaw error (0.1 rad). Each figure is superimposed with a reference target location, "X", and a predicted target shift, "O".

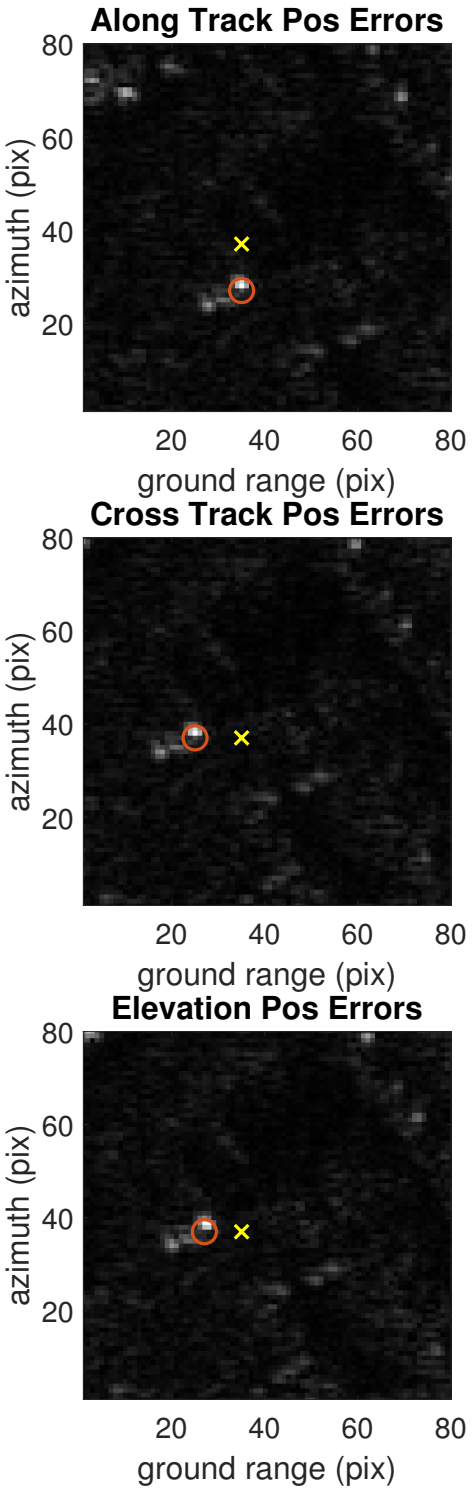

Fig. 4.14: Position errors in real data: Top, along track position error (3 m). Middle, cross track position error (3 m). Bottom, elevation position error (3 m). Each figure is superimposed with a reference target location, "X", and a predicted target shift, "O".

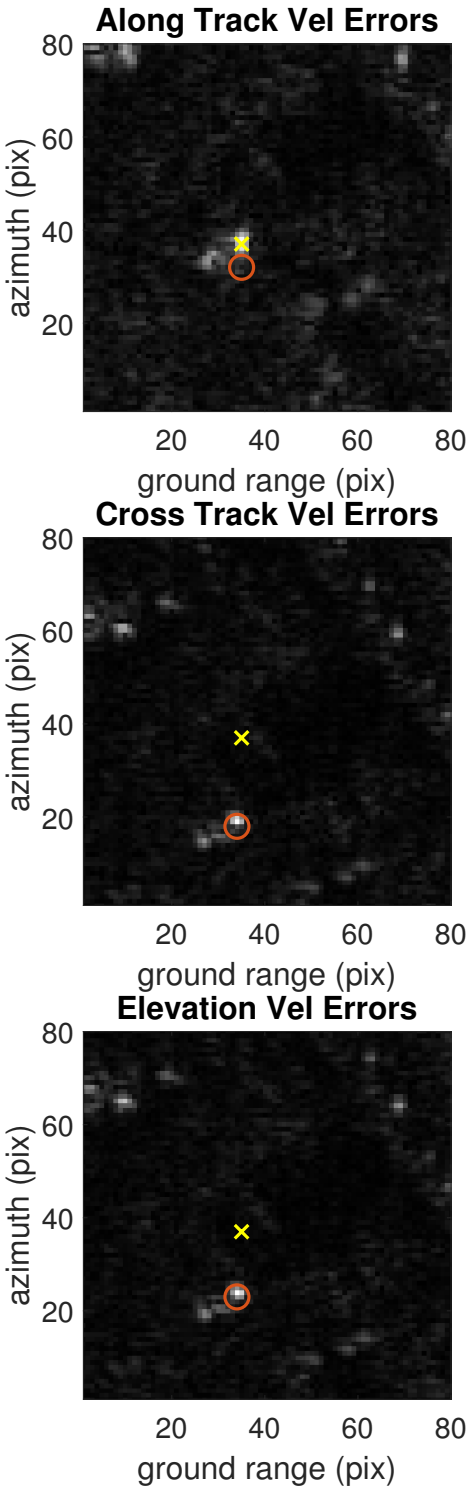

Fig. 4.15: Velocity errors in real data: Top, along track velocity error (1 m/s). Middle, cross track velocity error (0.2 m/s). Bottom, elevation velocity error (0.2 m/s). Each figure is superimposed with a reference target location, "X", and a predicted target shift, "O".

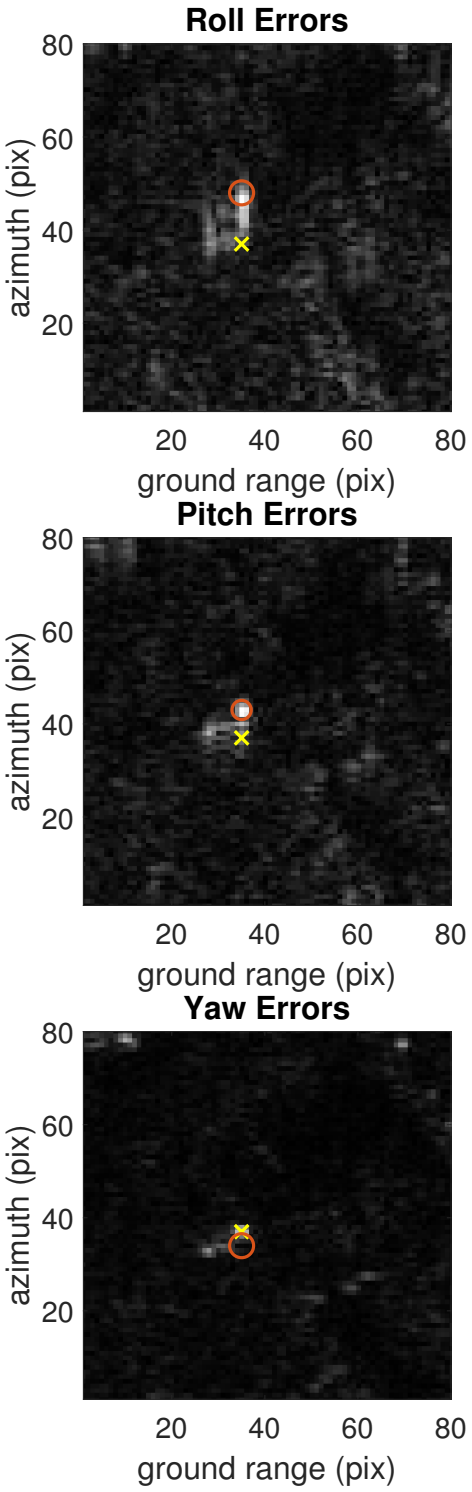

Fig. 4.16: Attitude errors in real data: Top, roll error (0.01 rad). Middle, pitch error (0.5 rad). Bottom, yaw error (0.1 rad). Each figure is superimposed with a reference target location, "X", and a predicted target shift, "O".

CHAPTER 5
GPS-DENIED NAVIGATION USING SYNTHETIC APERTURE RADAR AND KNOWN TARGET LOCATIONS

Past research has explored the feasibility of using radar telemetry in conjunction with an inertial navigation system to perform GPS denied navigation. The research presented in this paper further explores GPS denied navigation using radar by extracting range and cross range measurements from synthetic aperture radar images formed using the range Doppler algorithm. An inertial navigation and radar processing system is implemented using both real and simulated radar images to aid in estimating an aircraft's state in a GPS denied environment. Results and discussion have been provided. The results show that navigating in the absence of GPS using synthetic aperture radar is feasible with converging and bounded estimation errors.

5.1 Introduction

GPS denied navigation is the study of precisely navigating a vehicle in the absence of a Global Navigation Satellite System (GNSS) such as GPS. This can be accomplished in a variety of ways and is a very active field of research. Current research is exploring the feasibility of using synthetic aperture radar (SAR) as a means of navigating without GPS. SAR is a method of processing radar data to form images of a landscape, typically from an aircraft or spacecraft. The research presented in this paper expands on previous research and further tests the feasibility of using radar telemetry to aid in GPS denied navigation.

Specifically, the research presented here explores methods of extracting navigation information from fully formed SAR images. Images are created using the range Doppler algorithm (RDA), which is an efficient Fourier based image formation technique. Navigation measurements are extracted from images through a comparison with known target location data. Measurements are applied to a local coordinate frame and take the form of

range and cross range measurements.

A full flight simulation and radar simulation are implemented and verified via a Monte Carlo analysis. Algorithms developed in the simulated system are applied to navigation and radar data collected in Logan, Utah by the Space Dynamics Laboratory. Results from both the simulated system and real system are provided.

5.1.1 Literature Review

This research is conceptually organized into three categories: GPS denied navigation, SAR image formation, and measurement extraction from SAR images.

GPS denied navigation

GPS is integral in most navigation systems. Without GPS, a navigation system loses knowledge of position, velocity, and attitude, and estimates of the vehicle state experience error. Situations of GPS denial occur in a variety of situations. For example, GPS is easily jammed or spoofed. GPS can also be denied by natural or manmade structures obscuring the sky. Without GPS, a vehicle must rely on other forms of information to precisely navigate.

GPS denied navigation is typically performed using accelerometers and gyroscopes coupled with a selection of auxiliary sensors, from which auxiliary measurements are collected. Examples of possible auxiliary sensors include lidar, cameras, radar, range finders, etc, [16]. The auxiliary sensors attempt to supply knowledge sufficient to replace the knowledge lost by GPS.

Radar is one of the auxiliary sensors currently being researched for this purpose. Some advantages of radar are that its pulses can penetrate cloud cover and are actively illuminating. As such, images of a landscape using SAR can be formed during stormy weather and at night. This presents an advantage over other imaging systems that employ cameras, which can't image at night or during inclement weather, or lidar which may have trouble in inclement depending on illumination wavelengths.

Many methods for using radar as a supplementary sensor have been explored. These methods of navigation can be generally classified into two categories: relative navigation and absolute navigation. Absolute navigation places the vehicle on a global coordinate system such as latitude, longitude, and altitude. Relative navigation places the vehicle on a local coordinate system originating from some known feature or location.

In recent radar aided navigation literature, absolute and relative navigation can be split into several subcategories. Absolute radar aided navigation can be split into methods using terrain matching and methods using SAR images. Relative radar aided navigation can be split into methods using generic radar odometry, methods using Simultaneous Localization and Mapping, and methods again using SAR images. Each of these subcategories is briefly presented here.

Terrain contour matching is one approach to absolute radar aided navigation. Terrain contour matching is a scheme that exploits variations in terrain height along the flight path of an aircraft to determine the location of the vehicle in a global reference frame. Variations in terrain can be measured from radar nadir bounces or from interferometric SAR. These methods have been explored by Hollowell et al, Bergmann et al, Nordlund and Gustafsson, and more, each approach varying in complexity, from grids of Kalman filters to marginalized particle filters [28–32]. Of note is work done by Kim et al [33] measurements from an interferometric radar altimeter (IRA) provide the range to the nearest point to the radar vehicle from the underlying terrain. This measurement is processed together with information from a Digital Elevation Model (DEM) in a particle filter to predict a unique trajectory. Simulation results show ¡3 meters rms of absolute estimation error. The major factor in navigation accuracy is the accuracy of the DEM.

Absolute radar aided navigation using SAR images has been explored by the SARINA project [6,7,34–37]. The SARINA project uses prominent features in SAR images correlated to features within a reference map. In the case of mountainous regions, a DTED is used to synthesize an Interferometric SAR (InSAR) image, which is then compared to the InSAR image produced from the radar data. Divak approached the radar-aided absolute navigation

problem by simulating reference SAR images using 3D terrain data and electro-optical imagery, then comparing it to a real SAR image over the same area [38].

Relative radar aided navigation has been explored using general radar odometry. Scannapieco et al. detected ground targets using a constant false alarm rate and tracked their position using global nearest neighbor in range compressed data [39, 40]. Beard et al. exploited the fact that for linear flight paths, prominent reflectors manifest themselves as hyperbolic curves in the range-compressed vs. time image, [9, 11]. Features were tracked using a hyperbolic Hough transform, after which successive pairs of range measurements were used to determine changes in horizontal position. Altitude above ground level was determined from the nadir radar return. Mostafa et al, developed a combined radar odometry and visual odometry method and demonstrated performance on real data [41].

Simultaneous Localization and Mapping (SLAM) is another example of relative navigation. Where odometry approaches contains only states of the vehicle, SLAM approaches augment the vehicle states with the position of the reflectors in an EKF framework. The SLAM approach was studied over a period of five years by a group from the Air Force Institute of Technology [13, 42–48]. They developed a SLAM architecture that utilized the range-compressed radar data to detect, track, then estimate both the vehicle and reflector states culminating in a hardware implementation with highly reflective targets. Quist et al. extended research relying on the Hough transform by implementing a more efficient Recursive-RANSAC algorithm for data association and tracking of reflectors [12]. Here, reflector states were included in the state vector, resulting in a SLAM framework, which was demonstrated on real outdoor flight data.

Relative navigation using SAR images is less explored, but typically involves using an autofocusing algorithm to estimate velocity errors. Samczynski provides a discussion on the different approaches in this field [49, 50].

The research in this paper performs absolute navigation using SAR images coupled with known target position information along the flight trajectory. The targets are chosen such that they follow the trajectory of the vehicle in a “breadcrumb” like fashion. This

allows for known targets to be visible to the radar antenna at most points in the trajectory. This arrangement is representative of SAR images collected near towns, diverse landscapes, wooded areas, roads, etc.

Synthetic Aperture Radar

Synthetic aperture radar (SAR) is an imaging technique based on the transmission of radar pulses at intervals along the trajectory of some vehicle. The transmitted energy bounces off ground targets and returns to the radar receiver. After collecting data along a sufficiently long section of the trajectory, the received radar pulses are processed into images. Radar pulses can penetrate cloud cover and is actively illuminating. As such, images of a landscape using SAR can be formed during stormy weather and at night. This presents an advantage over other imaging techniques such as optical cameras or lidar systems.

Forming SAR images is a process of matched filtering. Several algorithms exist to process SAR data into images. Differences in image formation algorithms boil down to differences in how matched filtering is performed. For stripmap mode SAR, images can be formed using the back-projection algorithm (BPA) where images are processed with a time domain matched filter on hyperbolic curves in the data. The time domain matched filter is flexible in that it can accommodate complicated flight trajectories, but it is computationally expensive and sensitive to navigation errors. As such, the BPA requires high precision navigation data to form accurate images. Images can also be formed using RDA, which performs matched filtering in the frequency domain after range cell migration correction. The frequency domain filter is computationally less expensive and less sensitive to navigation errors than a time domain filter, but typically requires a straight trajectory to form accurate images. Other image formation algorithms for stripmap SAR include the Omega-K algorithm and the chirp scaling algorithm [3].

The research in this paper will use RDA to form images and SAR based measurements. RDA images are less sensitive to navigation error than BPA images. As such RDA can form measurable images in environments with errors that would leave BPA images unmeasurable. Additionally, this research is aimed toward navigation of light aircraft such as UAVs. The

computationally less expensive option is attractive for the potentially smaller processing packages available to UAVs. Because RDA forms images for straight trajectories, a straight flight assumption will be made in later sections to extract measurements from the RDA SAR images.

SAR imagers are dependent on vehicle position and velocity. Because of this dependence, errors trajectory estimation will result in errors in the final SAR image. Of particular note is that position estimation errors cause target shifting in the image, and velocity estimation errors cause target shifting and blurring [2]. Research performed at Utah State University hypothesizes that GPS denied navigation can be performed based on the SAR image error characteristics [17]. The research in this paper expands on that idea and uses corrupted images as a source of measurements in the navigation algorithm.

Measurement Extraction

This research is, in part, an extension of research done by Lindstrom et al, where the feasibility of GPS denied navigation was explored using range and range-rate measurements from radar telemetry [1]. In their research, range and range-rate measurements were synthesized from the estimated trajectory of an aircraft rather from radar data.

Here, a slightly different system will be implemented that extracts range and cross range position measurements from SAR images. Cross range measurements can be obtained simultaneously with range measurements, which provides an opportunistic advantage over range-rate measurements. The combination of range and cross range measurements is similar to the proposed system described by Nitti et al in their feasibility study [6].

Radar data can be collected and processed to various types of information, each with its own computational complexity. These types include raw radar return data (a.k.a. phase history), range compressed data, and fully formed images. Each type of data has different uses in navigation. For example, range measurements can be obtained from fully formed SAR images by calculating the distance between a location in the image to the radar vehicle. This calculation is straightforward when the SAR algorithm forms images in the slant range dimension, as is the case with RDA. Images formed in the ground range dimension require

an estimate of vehicle altitude above the ground, which may not be accurate or available in the absence of GPS and a DEM.

To form accurate cross range measurements, the time of closest approach (TOC) to any particular target must be known. The TOC is the moment in time when the radar vehicle is closest to the target in question. It is related to the Doppler of the azimuth signal, which requires accurate Doppler parameter estimation. Cumming et al and Li et al have shown methods to properly estimate Doppler parameters such as the Doppler centroid and Azimuth FM rate [51], [52], [3]. Examples of these methods include clutterlock and image autofocusing techniques. Wei et al combines least square regularization and minimum mean square error techniques to autofocus a SAR image from which model parameters can be estimated [53]. In this research, multilook misregistration autofocusing is used to estimate the Doppler parameters of the system.

Section 5.2 provides a background on SAR image formation using RDA. Section 5.3 develops a navigation system conducive to Monte Carlo analysis using SAR image measurements incorporated via an EKF. Section 5.4 summarizes results of the research and provides discussion. Section 5.5 concludes the document and suggests areas of future work. An appendix is included to provide additional details on multilook misregistration autofocusing, which is a processing step employed in section 5.3.

5.2 Background

This section is a self-contained tutorial on the range-Doppler Algorithm, as its use may be unfamiliar to those in the field of GPS-denied navigation. RDA is a SAR image formation technique that takes advantage of the Fourier domain to perform efficient matched filtering. The basic RDA algorithm can be summarized into the following steps:

1. Collect raw radar data
2. Perform range compression
3. Compute FFT in the azimuth dimension
4. Compensate for range cell migration
5. Perform azimuth compression

6. Return data to spatial domain

The process of forming RDA images begins by transmitting radar pulses at multiple points along a vehicle trajectory. These pulses reflect off ground targets and are collected by the radar receiver as raw SAR data. Radar pulses can have various structures but are usually of a linear frequency modulated (LFM) form. LMF signals, or "chirp" signals, are characterized by an instantaneous frequency that varies linearly with time. The transmitted LFM signal $s_{tx}(t)$ is written as

$$s_{tx}(t) = \begin{cases} \exp(j2\pi f_0 t + j\pi K t^2), & 0 \leq t \leq T \\ 0, & \text{otherwise} \end{cases} \tag{5.1}$$

where f_0 is the initial frequency, K is the linear FM rate in Hz/s, and T is the pulse duration.

The return LFM signal is denoted $s_{rx}(t)$. The return signal is written using a "stop and hop" assumption, which assumes the vehicle transmits and receives each radar pulse without traversing any distance.

$$s_{rx}(t) = A s_{tx}(t - \tau) \tag{5.2}$$

In this equation, A is the attenuation of the signal and τ is the time delay between the transmitted and received signal.

After collecting raw radar data, the data is fed through a matched filter in the range dimension to perform "range compression". The matched filter is a time reversed, conjugate version of the transmitted signal $s_{tx}(t)$, which is denoted $g(t)$. For efficiency, the matched filter is applied in the frequency domain. Let a capital letter denote a signal in the frequency

domain. The result of matched filtering is denoted $s_{out}(t)$, and is equal to

$$\begin{aligned} s_{out}(t) &= s_{rx}(t) * g(t) \\ &= \mathscr{F}^{-1}\left\{\mathscr{F}\left\{s_{rx}(t)\right\} \cdot \mathscr{F}\left\{g(t)\right\}\right\} \\ &= \mathscr{F}^{-1}\left\{S_{rx}(f) \cdot G(f)\right\} \end{aligned} \tag{5.3}$$

Each output of the matched filter is collected together to form the aggregate range compressed data, which will be denoted $s_{rc}(t, \eta)$. Note that the range compressed data is not just a function of range time t, but also azimuth time η. Visually, range compressed data appears as a composition of several hyperbolic arcs overlaid on top of each other. Each hyperbolic arc represents a ground target. This is illustrated in Figure 5.1.

Azimuth compression begins by taking an FFT of the range compressed data in the azimuth dimension. The data in the range dimension is left in the time domain. The azimuth-frequency range-time domain is referred to as the range-Doppler domain. The data in the range-Doppler domain is denoted,

$$\mathscr{F}_{\eta}\left\{s_{rc}(t, \eta)\right\} = S_{rc}(t, f_{\eta}) \tag{5.4}$$

Note that the η subscript on $\mathscr{F}$ denotes the FFT in the azimuth dimension. Range cell migration correction must be applied before applying a matched filter to range-Doppler data. Range cell migration refers to the hyperbolic shape of the targets in the data. Each of these hyperbolic arcs must be reformatted to form a straight line within the data. Without correcting for range cell migration, the final image will blur, and resolution will decrease. Figure 5.2 shows the data in the range Doppler domain before and after range cell migration correction

Range cell migration correction can be performed by re-indexing each row of the range-Doppler data according to a correction factor. The amount of correction required for each

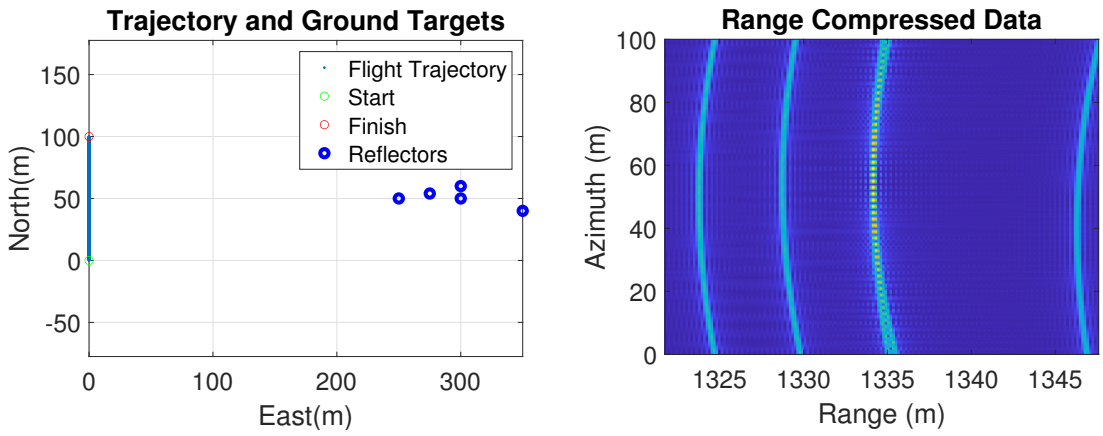

Fig. 5.1: Illustration of how ground targets at various locations (Left) become hyperbolic curves in the range compressed data (Right).

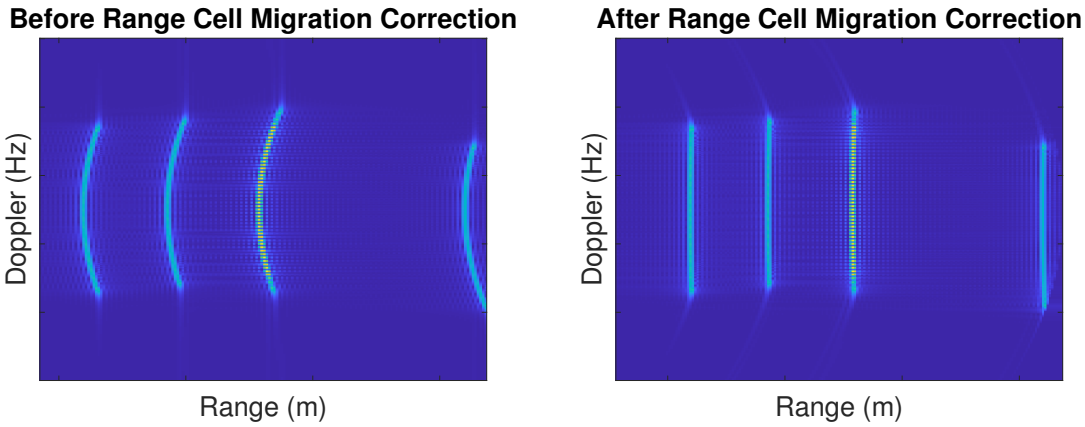

Fig. 5.2: Illustration of the data in the range Doppler domain before (Left) and after (Right) range cell migration correction.

range cell is denoted $\Delta R(f_\eta)$ and is equal to

$$\Delta R(f_\eta) = \frac{\lambda^2 R_0 f_\eta^2}{8V_r^2} \tag{5.5}$$

where λ is the wavelength of the carrier frequency, R_0 is the range of closest approach, f_η is the azimuth Doppler frequency, and V_r is the forward velocity of the radar vehicle. The data after range cell migration correction is denoted $S_{rcmc}(t, f_\eta)$.

After range cell migration correction, a matched filter is applied in the azimuth dimension. The azimuth matched filter is denoted $h(\eta)$ and is a phase only filter equal to the following.

$$h(\eta) = \exp(j2\pi \frac{V_r^2}{\lambda R_0}\eta^2) \tag{5.6}$$

Azimuth filtering is then the multiplication of the range cell migration corrected data and the Fourier transformed matched filter, $H(f_\eta) = \mathscr{F}\{h(\eta)\}$. The data after this step is denoted $S_{ac}(t, f_\eta)$

$$S_{ac}(t, f_\eta) = S_{rcmc}(t, f_\eta) \cdot H(f_\eta) \tag{5.7}$$

The final step in forming images using RDA is to take the inverse FFT in the Doppler dimension of $S_{ac}(t, f_\eta)$.

$$s_{ac}(t, \eta) = \mathscr{F}^{-1}\{S_{ac}(t, f_\eta)\} \tag{5.8}$$

Figure 5.3 shows a fully formed SAR image after azimuth compression.

5.3 Navigation System and Monte Carlo Framework Development

This section develops the framework of the navigation system used in this research. The system framework is based on the tangent frame kinematic model [25]. Because of the relatively short time frame for airborne SAR data collection, it is assumed that gravity is constant and that the earth is non-rotating.

This section additionally develops the extended Kalman filter framework. Truth and navigation states are defined with their associated dynamics models. The truth state differ-

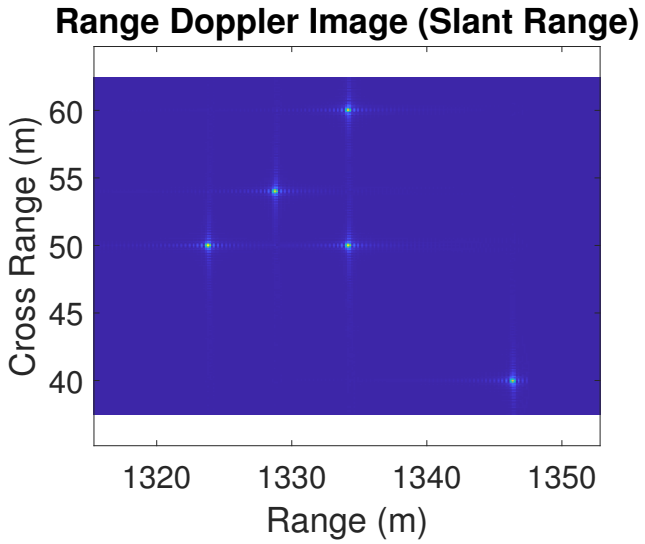

Fig. 5.3: Fully formed SAR image after azimuth matched filtering and inverse FFT.

ential equations are linearized about the navigation state to derive the linear dynamics of the estimation errors used within the EKF. The three states used in developing the EKF, the truth state, the navigation/estimated state, and error state, will be defined in relation to the "north, east, down" or n coordinate system. Measurement models using SAR images are developed. Finally, the Kalman filter equations are presented.

5.3.1 Truth and Navigation Models

The truth state is defined as the actual state of the vehicle as though it were measured with completely noiseless, zero bias instruments. The truth state is denoted $\mathbf{x}$ and behaves

according to the truth dynamics (or truth model), denoted $\dot{\mathbf{x}}$.

$$\mathbf{x} = \begin{bmatrix} \mathbf{p}^n \\ \mathbf{v}^n \\ q_b^n \\ \mathbf{b}_a \\ \mathbf{b}_g \\ b_h \\ b_r \\ b_c \end{bmatrix}, \quad \dot{\mathbf{x}} = \begin{bmatrix} \mathbf{v}^n \\ T_b^n \nu^b + g^n \\ q_b^n \otimes \frac{1}{2} \begin{bmatrix} 0 \\ \omega^b \end{bmatrix} \\ -\frac{1}{\tau_a}\mathbf{b}_a + \mathbf{w}_a \\ -\frac{1}{\tau_g}\mathbf{b}_g + \mathbf{w}_g \\ -\frac{1}{\tau_h}b_h + w_h \\ -\frac{1}{\tau_r}b_r + w_r \\ -\frac{1}{\tau_c}b_c + w_c \end{bmatrix} \tag{5.9}$$

In this definition, $\mathbf{p}^n$ is the position vector, $\mathbf{v}^n$ is the velocity vector, q_b^n is the attitude quaternion which transforms from the body frame, b, to the n frame, and each b_i term is a sensor bias term governed by a first order Markov model. For each bias term, $\frac{1}{\tau_i}$ is the time constant and w_i is process noise. The bias terms are for the accelerometer (a), gyroscope (g), altimeter (h), radar range measurements (r), and radar cross range measurements (c).

Note ν^b and ω^b are measurements from the accelerometer and gyroscope, respectively. g^n is used to represent the gravitational constant. The $\otimes$ symbol is used to denote quaternion multiplication. Lastly, R_b^n is a rotation matrix that rotates the accelerometer measurement into the n frame from the b frame.

The estimated state is defined as the state of the vehicle according to current estimates resulting from instruments and Kalman filtering. It is expected that noise will be present in the estimated state. The estimated state is denoted $\hat{\mathbf{x}}$ and behaves according to the navigation model (or navigation dynamics), which are denoted $\dot{\hat{\mathbf{x}}}$. Note that the estimated state and navigation model are nearly identical to the truth state and truth model. In the navigation model, bias terms are not propagated with process noise, as it is unknown to the filter. Additionally, each accelerometer and gyroscope measurement is compensated for

by the current bias estimate as opposed to the true bias.

$$\hat{\mathbf{x}} = \begin{bmatrix} \hat{\mathbf{p}}^n \\ \hat{\mathbf{v}}^n \\ q_{\hat{b}}^n \\ \hat{\mathbf{b}}_a \\ \hat{\mathbf{b}}_g \\ \hat{b}_h \\ \hat{b}_r \\ \hat{b}_c \end{bmatrix}, \quad \dot{\hat{\mathbf{x}}} = \begin{bmatrix} \hat{\mathbf{v}}^n \\ T_{\hat{b}}^n(\tilde{\nu}^b - \hat{\mathbf{b}}_a) + g^n \\ q_b^n \otimes \frac{1}{2} \begin{bmatrix} 0 \\ \tilde{\omega}^b - \hat{\mathbf{b}}_g \end{bmatrix} \\ -\frac{1}{\tau_a}\hat{\mathbf{b}}_a \\ -\frac{1}{\tau_g}\hat{\mathbf{b}}_g \\ -\frac{1}{\tau_h}\hat{b}_h \\ -\frac{1}{\tau_r}\hat{b}_r \\ -\frac{1}{\tau_c}\hat{b}_c \end{bmatrix} \tag{5.10}$$

The true values of specific force and angular rate are related to the measurement values, sensor biases, and noise,

$$\tilde{\nu}^b = \nu^b + \mathbf{b}_a + \mathbf{n}_\nu \tag{5.11}$$

$$\tilde{\omega}^b = \omega^b + \mathbf{b}_g + \mathbf{n}_\omega \tag{5.12}$$

where $\mathbf{n}_\nu$ and $\mathbf{n}_\omega$ are sensor noise vectors.

5.3.2 Linear Error Model

The error state is defined as the perturbation between the truth state and estimated state. This perturbation is given by

$$\delta\mathbf{p}^n = \mathbf{p}^n - \hat{\mathbf{p}}^n \tag{5.13}$$

$$\delta\mathbf{v}^n = \mathbf{v}^n - \hat{\mathbf{v}}^n \tag{5.14}$$

$$\begin{bmatrix} 1 \\ -\frac{1}{2}\delta\boldsymbol{\theta}^n \end{bmatrix} = q_b^n \otimes (\hat{q}_b^n)^* \tag{5.15}$$

$$\delta b_i = b_i - \hat{b}_i \tag{5.16}$$

where a δ denotes an element of the error state. The subscript i on δb_i is an index indicating any of the various bias terms.

The error state is governed by a linear model formed by linearizing the truth model about the estimated state. The result of the linearization is a model of the form

$$\delta\dot{\mathbf{x}} = \hat{F}\delta\mathbf{x} + B\mathbf{w} \tag{5.17}$$

where $\hat{F}$ is,

$$\hat{F} = \begin{bmatrix} F_{11} & F_{12} \\ 0_{9\times 9} & F_{22} \end{bmatrix} \tag{5.18}$$

$$F_{11} = \begin{bmatrix} 0 & I & 0 \\ 0 & 0 & [R^n_{\hat{b}}(\tilde{\nu}^b - \hat{\mathbf{b}}_a)]\times \\ 0 & 0 & 0 \end{bmatrix} \tag{5.19}$$

$$F_{21} = \begin{bmatrix} 0 & 0 & 0 & 0 & 0 \\ -R^n_{\hat{b}} & 0 & 0 & 0 & 0 \\ 0 & R^n_{\hat{b}} & 0 & 0 & 0 \end{bmatrix} \tag{5.20}$$

$$F_{22} \begin{bmatrix} -\frac{1}{\tau_a}I & 0 & 0 & 0 & 0 \\ 0 & -\frac{1}{\tau_g}I & 0 & 0 & 0 \\ 0 & 0 & -\frac{1}{\tau_h} & 0 & 0 \\ 0 & 0 & 0 & -\frac{1}{\tau_r} & 0 \\ 0 & 0 & 0 & 0 & -\frac{1}{\tau_c} \end{bmatrix} \tag{5.21}$$

The matrix B is a noise coupling matrix and is given by,

$$B = \begin{bmatrix} B_{11} & 0_{9\times 9} \\ 0_{9\times 9} & I_{9\times 9} \end{bmatrix} \tag{5.22}$$

$$B_{11} = \begin{bmatrix} 0 & 0 \\ -R^n_{\hat{b}} & 0 \\ 0 & R^n_{\hat{b}} \end{bmatrix} \tag{5.23}$$

The vector $\mathbf{w}$ is the noise vector and comprises accelerometer and gyroscope measurement noise as well as the process noise driving the sensor bias states.

$$\mathbf{w} = [\mathbf{n}_\nu, \mathbf{n}_\omega, \mathbf{w}_a, \mathbf{w}_g, w_h, w_r, w_c]^T \tag{5.24}$$

Note the "cross" operator, $\times$, which is defined as,

$$\times : \mathbb{R}^3 \rightarrow \mathbb{R}^{3\times 3}, \text{ s.t. } \forall a \in \mathbb{R}^3, (\mathbf{a}\times) = \begin{bmatrix} 0 & -a_3 & a_2 \\ a_3 & 0 & -a_1 \\ -a_2 & a_1 & 0 \end{bmatrix}$$

5.3.3 Measurement Model

The measurement model is comprised of three different measurements. These are the range, cross range, and altitude measurements. All measurements are taken at the time of closest approach for the target corresponding to the given measurement. This means the range and cross range measurements will reveal offsets from the estimated range of closest approach and time of closest approach, respectively. Altitude measurements are taken to resolve an ambiguity that arises in range measurements between cross track and elevation errors.

The range and cross range measurements assume knowledge of a target location. For the purposes of this research, it is assumed that knowledge of the target location comes in the form of a previously-collected SAR image. Other formats of target knowledge are possible and can be implemented for specific system needs. Offsets from true target locations are found using a two-dimensional cross correlation between the collected SAR image and a reference SAR image, both of which are formed in the slant range dimension. The location of the peak of the cross correlation is used to find the offset from the true target location. The offsets are used to calculate the range and cross range measurements. This process is illustrated in Figure 5.4.

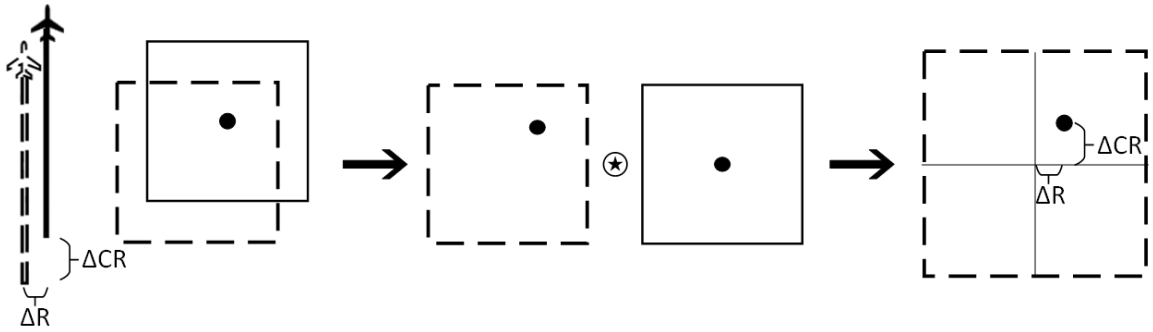

Fig. 5.4: Illustrates the process of calculating radar measurements. A reference image (distinguished using solid lines) and an image formed using the estimated flight trajectory (distinguished using dotted lines) are cross correlated with each other. Offsets in range, ΔR, and cross range, ΔCR, appear in the cross correlation as a shift in the main peak.

Navigation errors will cause blurring and shifting in a SAR image. Shifting is easily detected using the above-mentioned cross correlation. However, when blurring is present in a collected image, the cross correlation yields inaccurate results. An auto-focusing algorithm is, therefore, performed prior to cross correlation to remove blurring.

The measurements described above comprise the "truth measurements". Truth measurements are denoted $\tilde{z}$ where a subscript is added to indicate the measurement type. Altimeter measurements are denoted $\tilde{z}_h$ and are equal to

$$\tilde{z}_h = -p_z + b_h + n_h \tag{5.25}$$

Range and cross range measurements are collected simultaneously and are thus grouped together. These measurements are denoted $\tilde{\mathbf{z}}_{r,c}$ and are equal to

$$\tilde{\mathbf{z}}_{r,c} = \begin{bmatrix} \tilde{z}_r \\ \tilde{z}_c \end{bmatrix} = \begin{bmatrix} ||\mathbf{p}_{targ} - \mathbf{p}^n_{toc}|| + b_r + n_r \\ ||\mathbf{p}^n - \mathbf{r}^n_{orig}|| + b_c + n_c \end{bmatrix} \tag{5.26}$$

In the above measurements, altitude is simply p_z, which is the *down* component of the position state. Range is the distance between the known target location $\mathbf{p}_{targ}$ and the position of the aircraft at the time of closest approach $\mathbf{p}^n_{toc}$.

The cross range measurement is the along track distance travelled by the aircraft. The

along track distance can be measured on either a global coordinate system with the origin being the beginning of the flight trajectory, or on a local coordinate system with the origin being arbitrarily chosen. The origin point is denoted $\mathbf{r}^n_{orig}$ and is chosen to be located within the subaperture. This measurement formulation assumes straight flight. As this assumption is more likely to be true during radar data collection, the model in this paper assumes a local coordinate system centered on an origin located within the trajectory of the current SAR image's subaperture.

Each measurement defined above can be taken at any point within a SAR image's subaperture. During implementation, it is chosen to collect and process measurements at the time of closest approach to the target within the current image. Note that, each measurement in the model is corrupted by both bias, b_i, and noise, n_i.

Analogous to the truth measurements $\tilde{z}$, are the estimated measurements, which are denoted $\hat{\tilde{z}}$. The equations describing the behavior of estimated measurements are nearly identical to the true measurement equations but lacks any knowledge of noise terms and uses estimated states to calculate each measurement.

$$\hat{\tilde{\mathbf{z}}}_{\mathbf{h}} = -\hat{p}_z + \hat{b}_h \tag{5.27}$$

$$\hat{\tilde{\mathbf{z}}}_{\mathbf{r,c}} = \begin{bmatrix} \hat{\tilde{z}}_r \\ \hat{\tilde{z}}_c \end{bmatrix} = \begin{bmatrix} ||\mathbf{p}_{targ} - \hat{\mathbf{p}}^n_{toc}|| + \hat{b}_r \\ ||\hat{\mathbf{p}}^n - \hat{\mathbf{r}}^n_{orig}|| + \hat{b}_c \end{bmatrix} \tag{5.28}$$

The difference between the true measurements $\tilde{\mathbf{z}}$ and estimated measurements $\hat{\tilde{\mathbf{z}}}$ is called the "residual" and is used in the EKF to update the estimate of the error state.

The linearization of the truth model around the navigation state is given as,

$$\delta\tilde{\mathbf{z}} = H\delta\mathbf{x} + \gamma \tag{5.29}$$

where H is the sensitivity matrix for the measurements. H is found by taking the Jacobian of each truth measurement and evaluating about the estimated state. This results in

$$H = \begin{bmatrix} H_1 \\ H_2 \end{bmatrix} \tag{5.30}$$

where H_1 is the sensitivity matrix for the altimeter measurement and is equal to

$$H_1 = \begin{bmatrix} [0, 0, -1] & 0_{1\times 12} \end{bmatrix} \tag{5.31}$$

H_2 is the sensitivity matrix for the radar range and cross range measurements and is equal to

$$H_2 = \begin{bmatrix} \frac{-\mathbf{d}^T}{||\mathbf{d}||} & 0_{1\times 12} \\ \frac{-\mathbf{l}^T}{||\mathbf{l}||} & 0_{1\times 12} \end{bmatrix} \tag{5.32}$$

where $\mathbf{d} = \mathbf{p}_{targ} - \mathbf{p}^n_{toc}$ and $\mathbf{l} = \mathbf{p}^n - \mathbf{r}^n_{orig}$. The vector γ is measurement noise and is equal to

$$\gamma = [n_r, n_c, n_h]^T \tag{5.33}$$

5.3.4 Covariance Propagation

With states, models, and measurements defined and the appropriate linearizations performed, the structure of the EKF can be built. This begins with initialization and propagation of the covariance matrix. The covariance of the error state is initialized using a steady state covariance matrix from an INS processing GPS measurements. This mimics the situation when GPS is denied mid-flight. The covariance of the error state is then propagated forward in time as

$$\dot{P} = \hat{F}P + P\hat{F} + BQB^T \tag{5.34}$$

where $\hat{F}$ and B are defined previously.

The Q matrix is the power spectral density of the noise vector $\mathbf{w}$. Assuming the noise is zero mean, gaussian, and independent, Q is a diagonal.

$$Q = diag(\sigma^2_{vrw} I_{3\times3}, \sigma^2_{arw} I_{3\times3}, \frac{2\sigma^2_{ss,b_a}}{\tau_a} I_{3\times3}, \frac{2\sigma^2_{ss,b_g}}{\tau_g} I_{3\times3}, \frac{2\sigma^2_{ss,b_h}}{\tau_h}, \frac{2\sigma^2_{ss,b_r}}{\tau_r}, \frac{2\sigma^2_{ss,b_c}}{\tau_c}) \tag{5.35}$$

When a measurement becomes available from the radar imaging system, a Kalman update is performed. To perform a Kalman update, the Kalman gain is first calculated, which is given by

$$K = P^- H^T [H P^- H^T + G R G^T]^{-1} \tag{5.36}$$

where P^- is the error state covariance before the Kalman update, and R is the covariance of the noise on the available measurement. The matrix H varies between H_1 and H_2 depending on the type of measurement available.

The Kalman gain is then used to update the error state covariance using the Joseph form,

$$P^+ = [I - KH] P^- [I - KH]^T + K G R G^T K^T \tag{5.37}$$

The Kalman gain and measurement residual is also used to update the estimate of the error state.

$$\delta\hat{\mathbf{x}}^+ = K[\tilde{\mathbf{z}} - \hat{\tilde{\mathbf{z}}}] \tag{5.38}$$

After updating the estimate of the error state vector, the new error is applied to the navigation state, which forms an updated navigation state vector. This update is performed as,

$$\hat{\mathbf{x}}^{+} = \begin{bmatrix} (\hat{\mathbf{p}}^{n})^{-} + \delta\mathbf{p}^{n} \\ (\hat{\mathbf{v}}^{n})^{-} + \delta\mathbf{v}^{n} \\ \begin{bmatrix} 1 \\ -\frac{1}{2}\delta\theta_{b}^{n} \end{bmatrix} \otimes (q_{b}^{n})^{-} \\ (\hat{\mathbf{b}}_{a})^{-} + \delta\mathbf{b}_{a} \\ (\hat{\mathbf{b}}_{g})^{-} + \delta\mathbf{b}_{g} \\ (\hat{b}_{h})^{-} + \delta b_{h} \\ (\hat{b}_{r})^{-} + \delta b_{r} \\ (\hat{b}_{c})^{-} + \delta b_{c} \end{bmatrix} \tag{5.39}$$

5.4 Results

The system described above is implemented on both simulated and real data. Results of both types of data are given in this section. Loosely coupled GPS measurements are used to calibrate initial bias estimates and initial covariance matrices. After calibration, GPS measurements cease, and the aircraft begins navigating using SAR images.

5.4.1 Simulated Data

A full flight and radar processing simulation was created to test the feasibility of the work described in the previous sections. The true flight trajectory is a straight and level flight flying northward. Initial errors are injected into the true trajectory and are propagated forward to create the estimated trajectory. The radar scene is a random field of radar scatterers dense enough to ensure that a few targets appear in every SAR image. The flight is fifty seconds long and is split into fifty subapertures, each one being one second long. In the simulation, an aircraft flies along the true trajectory and collects radar data. At the end of each subaperture, a SAR image is formed using RDA and the estimated vehicle state. Measurements are extracted and applied in the EKF using the method described in Section 5.3.3. The true trajectory and the estimated trajectory produced by the EKF are compared, and estimation errors are calculated.

In the simulation, accelerometer and gyroscope measurements are synthesized with

added zero mean gaussian noise. Noise is consistent with a tactical grade inertial measurement unit (IMU). Tactical grade measurements are chosen to mimic the quality of the data used in the real data implementation.

Noise is also added to the radar measurements to better mimic measurements from the real data. Because the radar measurements rely on a cross correlation to infer distances, the quality of the measurement depends heavily on the quality of the reference target information and the radar scene being imaged. Radar scenes with very diffuse or very sparse targets may produce an inaccurate cross correlation, leading to an inaccurate range or cross range measurement.

Tables 5.1 and 5.2 summarizes the parameters used for both the navigation system and radar system.

Table 5.1: Summary of radar parameters used in simulation.

SAR Parameter	Value
RF center frequency	9.75 GHz
Bandwidth	500 MHz
Range over-sample rate	2
Range resolution	0.15 m
PRF	100 Hz
Initial Velocity	10 m/sec
Antenna squint	0.0 deg
Ideal azimuth resolution	0.1 m
Range offset	2000 m
Min/Max range	2000 m/2210 m
Sub aperture length	1 sec (10 m)

Table 5.2: Summary of navigation parameters used in simulation.

Navigation Parameter	Value
Velocity random walk	0.1 m/s/sqrt(hr)
Initial Accelerometer bias	0.01 g
Angular random walk	0.1 deg/sqrt(hr)
Initial Gyroscope bias	5 deg/hr
Altimeter standard deviation	1.3 m
Range standard deviation	0.25 m
Cross range standard deviation	0.25 m

The results of the simulated Monte Carlo analysis are provided in Figures 5.5 through 5.8. Each of the figures shows a collection of solid lines mostly bounded by a set of dashed lines. Each solid line represents a single run of the Monte Carlo simulation. Each dotted line represents a 3-sigma bound inside which the solid lines should mostly fall.

Figure 5.5 shows only one set of solid lines each. This figure plots the residual measurement $\tilde{\mathbf{z}} - \hat{\tilde{\mathbf{z}}}$ for one of the Monte Carlo runs. According to Kalman filter theory, the residuals should be white and zero mean in structure. This figure provides a visual confirmation of the residuals meeting these requirements. Figure 5.6 shows the estimation error in the position states, calculated as the difference between the true and estimated trajectories. Figures 5.7 and 5.8 show similar information for the aircraft velocity and attitude, respectively.

The results show that the proposed navigation and radar system are capable of estimating the aircraft state in the absence of GPS. The measurement residuals are white and zero mean. The estimation error converges and remains bounded over the course of the full trajectory. The position is estimated in all dimensions to within 3 meters. Velocity is estimated to within 0.5 meters per second. North and east attitudes are estimated within 2 milli-radians, and down attitude is estimated withing 7 milli-radians.

5.4.2 Real Data

A system similar to that for the simulated data was implemented to process real flight and radar data. As with simulated data, the real flight length is fifty seconds, which is split into fifty sub-apertures, each sub-aperture being one second long.

Flight and radar data were collected and provided by the Space Dynamics Lab (SDL) in Logan, Utah. The data were collected on their FlexSAR system, a low-cost, high quality prototyping SAR instrument [54], paired with a NovAtel SPAN CPT7 tactical grade IMU [55]. A GPS based navigation solution is available for the trajectory, which is taken to be the "truth" trajectory. This solution is achieved via post-processing in Waypoint software by NovAtel and is accurate to about 1 cm. Altimeter measurements were synthesized using parameters based on the Honeywell Precision Barometer HPB [56].

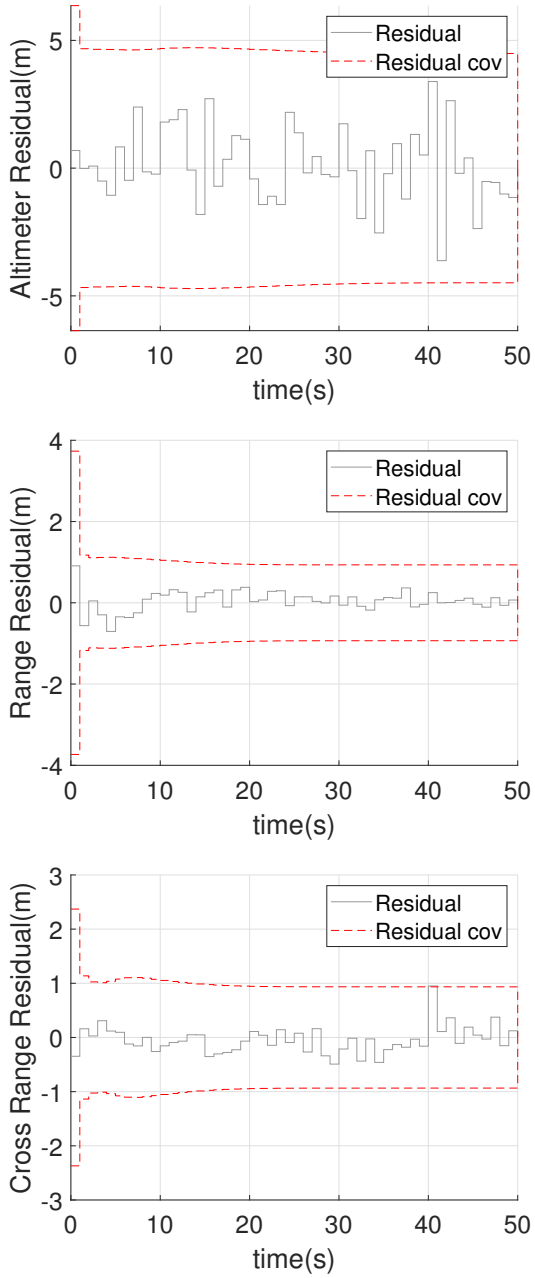

Fig. 5.5: Measurement residuals for altimeter measurements (Top), range measurements (Middle), and cross range measurements (Bottom). Dotted lines signify 3 sigma bounds, and solid lines represent residual measurements.

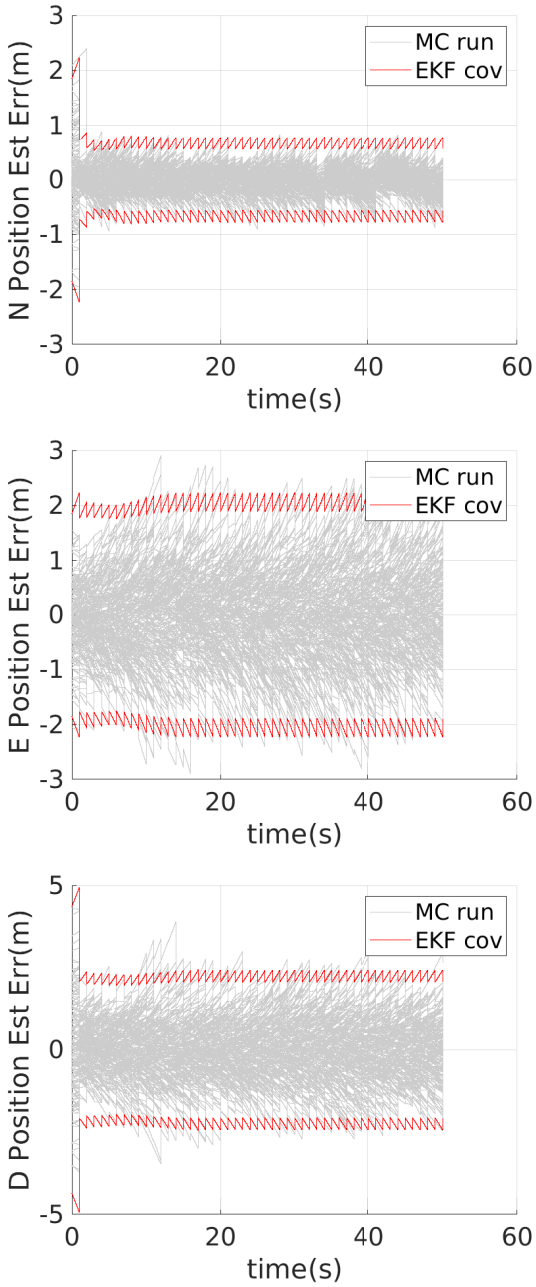

Fig. 5.6: Estimation errors for north position (Top), east position (Middle), and down position (Bottom). Dotted lines signify 3 sigma bounds. Individual solid lines represent individual runs of the Monte Carlo simulation.

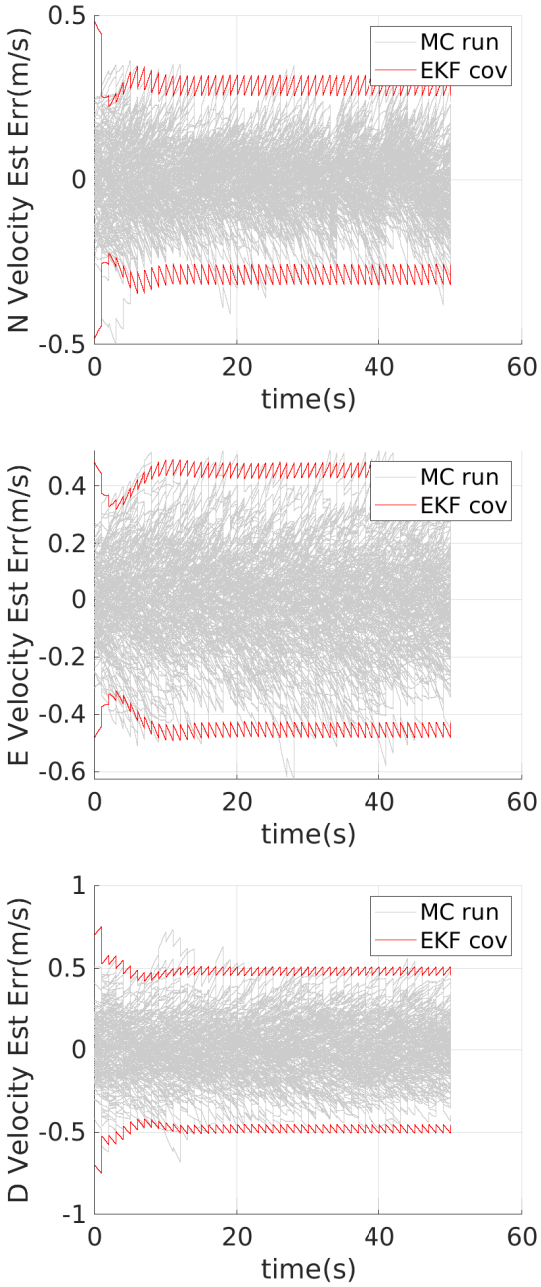

Fig. 5.7: Estimation errors for north velocity (Top), east velocity (Middle), and down velocity (Bottom). Dotted lines signify 3 sigma bounds. Individual solid lines represent individual runs of the Monte Carlo simulation.

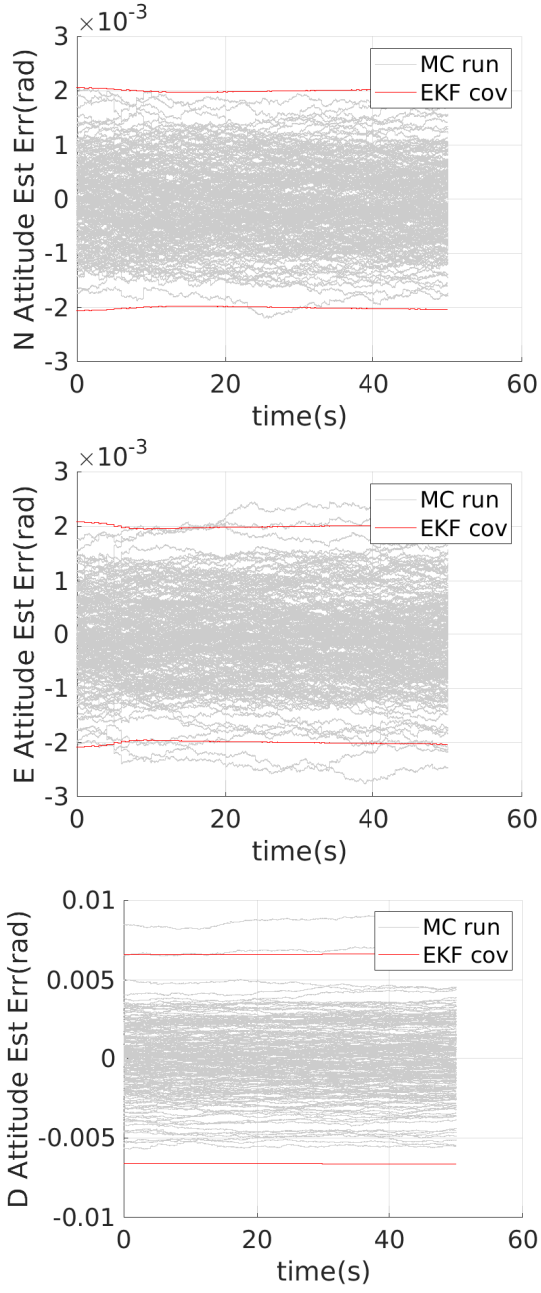

Fig. 5.8: Estimation errors for north attitude (Top), east attitude (Middle), and down attitude (Bottom). Dotted lines signify 3 sigma bounds. Individual solid lines represent individual runs of the Monte Carlo simulation.

Tables 5.3 and 5.4 list parameters specific to the instruments used in data collection.

Table 5.3: Summary of radar parameters from the FlexSAR system.

SAR Parameter	Value
RF center frequency	9.75 GHz
Bandwidth	500 MHz
Range over-sample rate	1
Range resolution	0.2998 m
PRF	5000 Hz (decimated to 1667 Hz)
Initial Velocity	60 m/sec
Antenna squint	0.0 deg
Ideal azimuth resolution	0.0378 m
Range offset	1948 m
Min/Max range	1948 m/2112 m
Sub aperture length	1 sec (60 m)

Table 5.4: Summary of navigation parameters from the FlexSAR system.

Navigation Parameter	Value
Velocity random walk	0.1 m/s/sqrt(hr)
Initial Accelerometer bias	0.0033 g
Angular random walk	0.1 deg/sqrt(hr)
Initial Gyroscope bias	4.0758 deg/hr
Altimeter accuracy (3σ)	0.4 hPa

For real data, a single iteration of flight estimation is performed. Accelerometer and gyroscope measurements are provided in the data set and are used to propagate the navigation state forward in time. At the end of each subaperture, a SAR image is formed, and measurements are extracted and applied to the estimated state via the EKF. estimation errors are recorded throughout the flight and are displayed. At the end of the flight, state estimation errors are calculated and displayed.

Estimation results are shown in Figures 5.9 through 5.12. These again illustrate the performance of the system in terms of residuals and estimation errors. Figure 5.9 provides a visual confirmation that the measurement residuals are zero mean and white.

Over the course of a fifty second GPS denied flight, the estimation errors remain

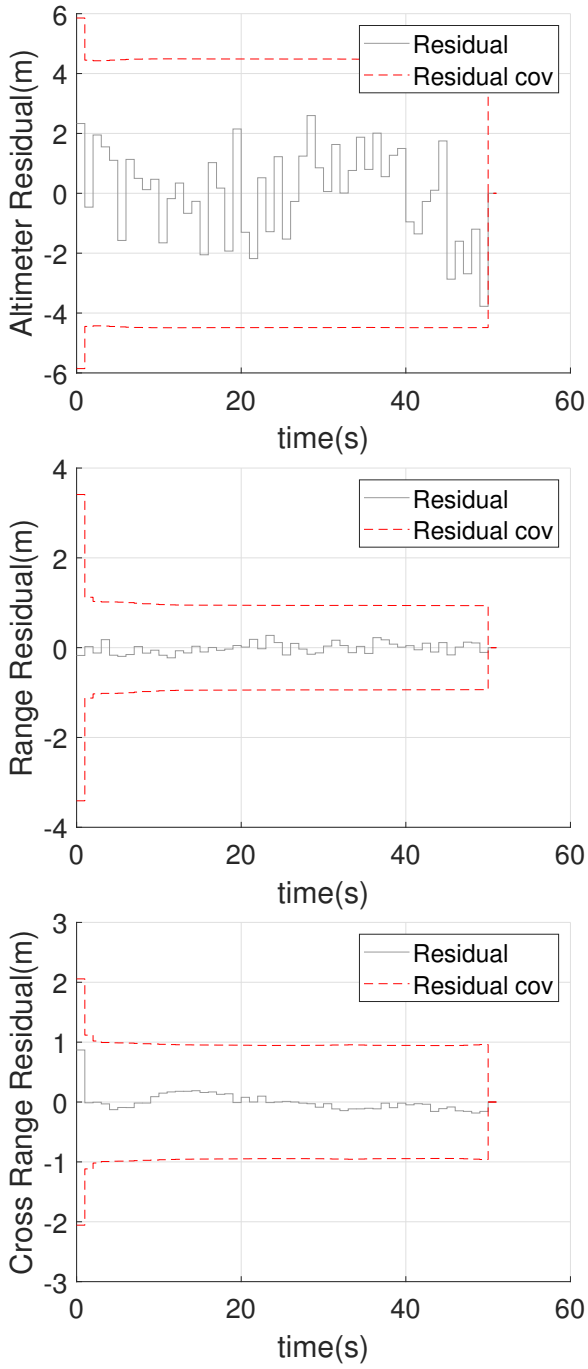

Fig. 5.9: Measurement residuals from the real data set for the altimeter measurements (Top), range measurements (Middle), and cross range measurements (Bottom). Dotted lines signify 3 sigma bounds, and solid lines represent residual measurements.

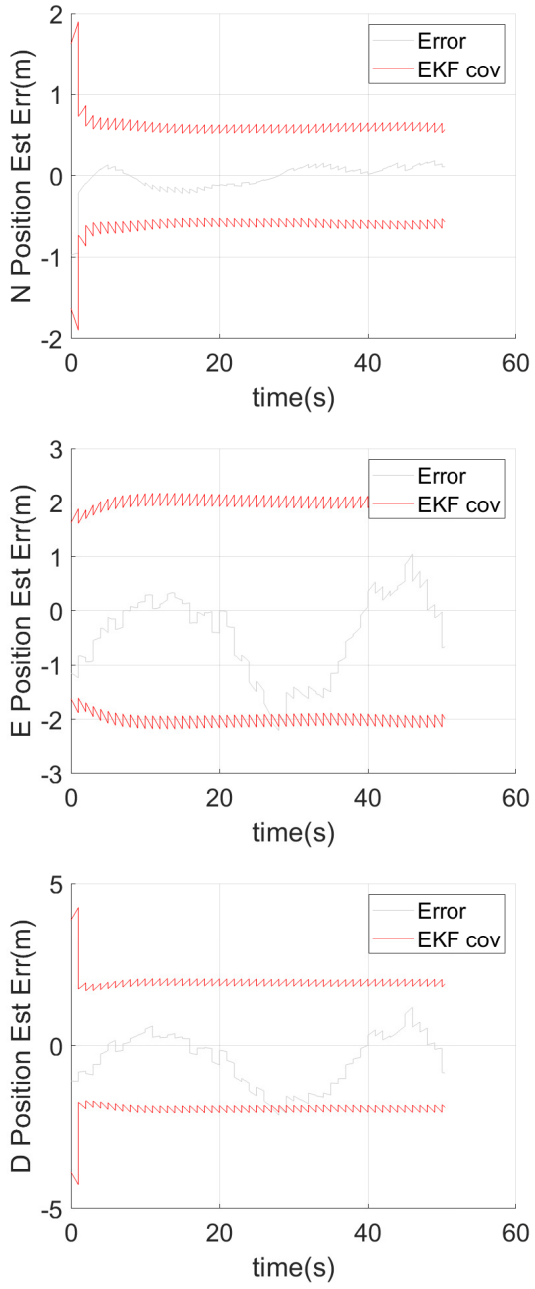

Fig. 5.10: Estimation errors from the real data set for north position (Top), east position (Middle), and down position (Bottom). Dotted lines signify 3 sigma bounds. Solid lines represent actual estimation error.

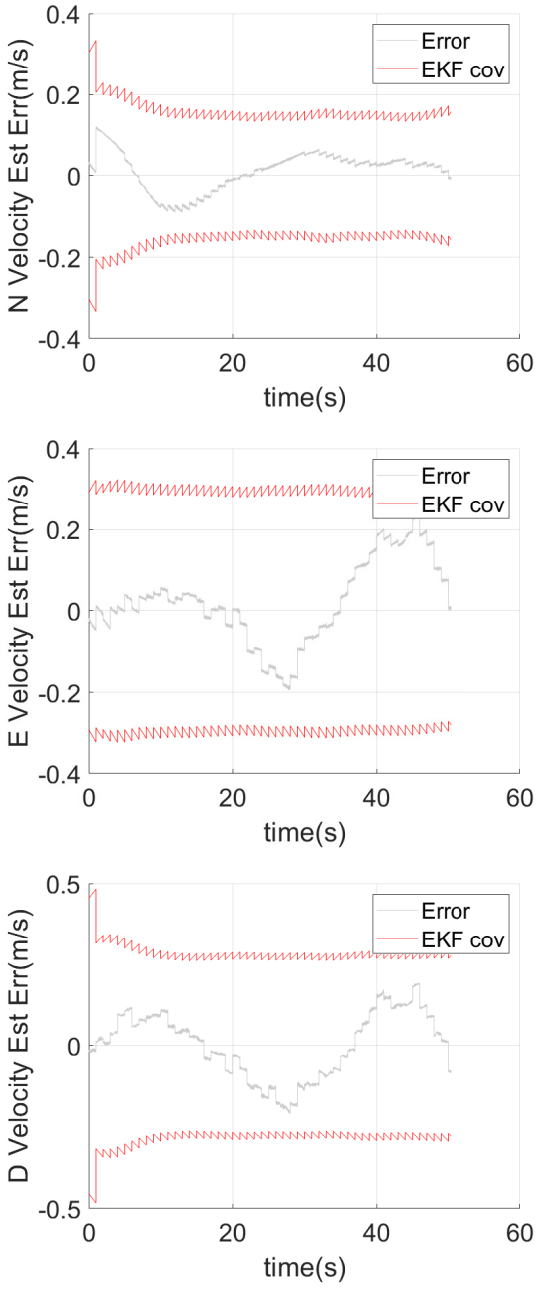

Fig. 5.11: Estimation errors from the real data set for north velocity (Top), east velocity (Middle), and down velocity (Bottom). Dotted lines signify 3 sigma bounds. Solid lines represent actual estimation error.

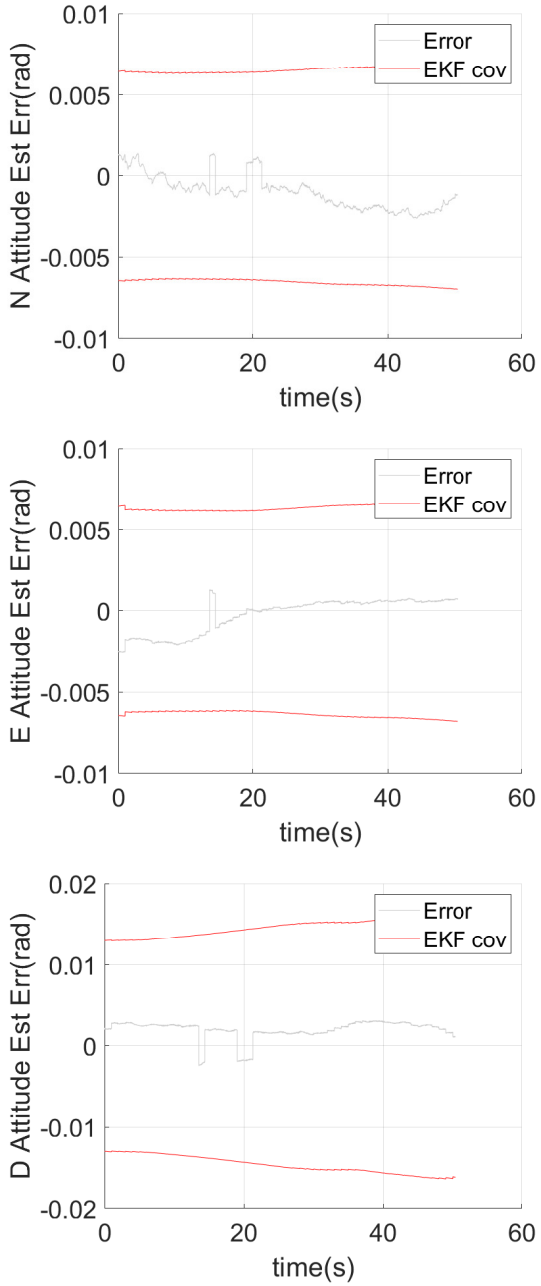

Fig. 5.12: Estimation errors from the real data set for north attitude (Top), east attitude (Middle), and down attitude (Bottom). Dotted lines signify 3 sigma bounds. Solid lines represent actual estimation error.

bounded within the 3-sigma covariance lines. Position errors stay bounded within approximately 3 meters. Velocity errors stay bounded within approximately 0.4 meters per second. Attitude errors stay bounded within approximately 7 milli-radians in the north and east case and 15 milli-radians in the down case. These results are very similar to the simulated data case, which uses similar parameter and initialization values to best mimic the real data case.

To highlight the effect of the radar measurements on estimation errors, Figure 5.13 has been provided. This figure plots estimation errors bounds for north, east and down positions. Each sub-figure shows two bounds on a logarithmic scale. The dotted line represents the estimation error 3σ bound when no SAR measurements are processed. The solid line shows the same bound when SAR measurements are processed. Notice that omission of SAR measurements degrades the north and east estimates, and they begin to grow without bound. The down estimate stays bounded due to altimeter measurements.

5.5 Conclusion

This paper furthers the research done in absolute radar aided GPS denied navigation using RDA SAR images. The feasibility of extracting navigation information from RDA SAR images is demonstrated. Range and cross range measurements were extracted from RDA SAR images via comparing to known target locations and processed in an indirect extended Kalman filter. Both simulated data and real data were analyzed. Estimation using simulated data was shown to have converging estimation errors and be bounded within 3-sigma values of the state covariance matrix. Estimation errors using the real data were similarly bounded. In both cases, errors in position were estimated with approximately 3 meters.

These results further suggest that using SAR images in GPS denied situations is a viable solution for absolute GPS denied navigation.

5.5.1 Future Work

The SAR based measurements in this paper are based on a cross correlation, which

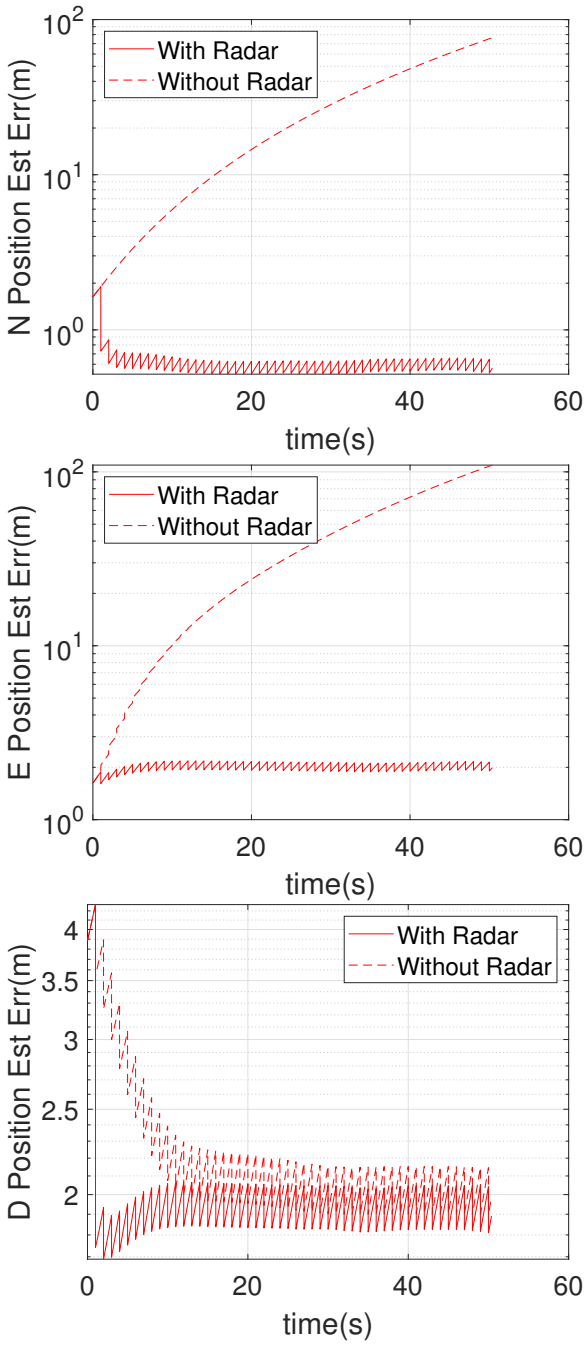

Fig. 5.13: Comparison of position estimation error bounds while using SAR measurements and while omitting SAR measurements. Dotted lines indicate the bounds given omission of SAR measurements. Solid lines indicate the bounds given the use of SAR measurements.

shows a dependence on the type and uniqueness of the targets in the area imaged by the radar. Investigation could be performed on target types and scene uniqueness and the induced effect on measurement noise. This would reveal scene requirements of a SAR based navigation system for successful GPS denied navigation.

Real time generation of SAR images has been demonstrated in past research. Methods developed here could be implemented on a real time system.

This research was performed using range, cross range, and altitude measurements. Research could be performed to explore the effect of alternate or addition measurements incorporated into the measurement model. Research could be performed to find other SAR based measurements and compare their effectiveness in a GPS denied scenario.

5.6 Appendix

5.6.1 Autofocus

There are several methods of autofocusing images. From Cumming and Wong, four methods are presented [3]. Two are magnitude based and two are phase based. The magnitude based methods are contrast maximization and azimuth misregistration. The phase based methods are phase difference (PD) and phase gradient algorithm (PGA). The research in this paper performs azimuth misregistration.

Azimuth misregistration is based on multilook processing. The idea is that an error in the azimuth FM rate will cause a ground target to shift in the azimuth direction between two separate looks of the same target. Azimuth FM rate errors are introduced into the SAR imaging system when forward velocity or attitude errors are present.

In Section 4.2 the azimuth matched filter was expressed in terms of R_0 and V_r.

$$\exp\{j2\pi\frac{V_r^2}{\lambda R_0}\eta^2\} \tag{5.40}$$

By defining the azimuth FM rate as $K_a = \frac{2V_r^2}{R_0\lambda}$, the azimuth matched filter can be expressed as

$$\exp\{j\pi K_a \eta^2\} \tag{5.41}$$

Now let K_{amf} be the azimuth FM rate with an error included such that $K_{amf} = K_a + \Delta K$ where ΔK is the amount of error present in K_{amf}.

The matched filter is adjusted to produce two different looks of the same target. This is done by selecting two disjoint frequency bands within the frequency range of the original matched filter. In general, the frequency used in the matched filter is equal to $f_\eta = -K_a\eta$ where η is centered around the time of closest approach to a given target. Each of the two looks will have a different center frequency, denoted $f_{\eta,1}$ and $f_{\eta,2}$. Δf_a is defined as the difference between the center frequencies of the two looks, $\Delta f_a = f_{\eta,2} - f_{\eta,1}$.

The amount of misregistration between the two separate looks is denoted $\Delta\eta$ and is defined as

$$\Delta\eta = -\Delta f_a \left(\frac{1}{K_a} - \frac{1}{K_{amf}}\right) \tag{5.42}$$

By rearranging equation (5.42), the azimuth FM rate error can be expressed as

$$\Delta K_a \approx -\frac{K_{amf}^2}{\Delta f_a}\Delta\eta \tag{5.43}$$

$\Delta\eta$ can be solved for numerically by cross correlating Look 1 and Look 2 with each other. the peak of the cross correlation shifts according to the level of misregistration. With ΔK solved for, the corrected azimuth matched filter is equal to

$$\exp\{j\pi(K_{amf} - \Delta K)\eta^2\} \tag{5.44}$$

The new azimuth matched filter is used to perform azimuth compression. The result is a focused image that can then be used for measurement extraction in the navigation system described in the main body of this paper. Figure 5.14 shows a blurred SAR image before and after azimuth misregistration autofocusing.

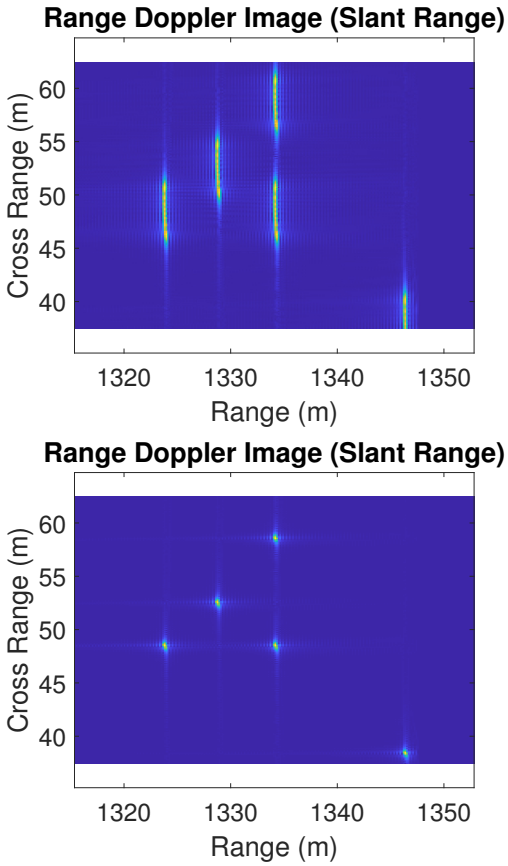

Fig. 5.14: Comparison of a blurry SAR image before (Top) and after (Bottom) azimuth misregistration autofocusing.

CHAPTER 6

CONCLUSION

In this thesis, several aspects of SAR aided GPS denied navigation were explored. The first portion of research investigated the feasibility of using range and range rate measurements to navigate in the absence of GPS. As part of the investigation, several parameters were varied, and their results were analyzed. These parameters include IMU grade, measurement noise strength, and ground target location. Overall, the study concluded that GPS denied navigation using range and range rate measurements was feasible.

The next contribution of this thesis was an in-depth development of the relationships between navigation errors and SAR imaging errors using BPA images. Specifically, the effects of aircraft position, velocity, and attitude errors on SAR image blurring and shifting were analyzed. The developed relationships were observed and validated on both simulated and real SAR data. The results suggested that the reverse problem of using image errors to characterize navigation errors may be possible but will require further research. This is due to ambiguities that arise between image errors and navigation errors.

The final contribution of this thesis was to demonstrate a full system that performed GPS denied navigation using both simulated and real SAR data. Range and cross range measurements were extracted from SAR images formed using RDA and incorporated into an indirect EKF. Navigation estimation using simulated data was shown to have converging estimation errors and be bounded within 3-sigma values of the state covariance matrix. Navigation using the real data also resulted in bounded and converging estimation errors.

The contributions of this thesis are stepping stones in creating a robust GPS denied navigation system using SAR as an auxiliary navigation instrument. A natural extension of this research is to create a real time implementation, which would be a significant contribution to the field.

Additionally, the SAR measurements from the full implementation are based on a cross

correlation, which shows a dependence on the type and uniqueness of the targets in the area imaged by the radar. Investigation could be performed on target types and scene uniqueness and their induced effect on measurement noise. This would reveal scene requirements of a SAR based navigation system for successful GPS denied navigation.

Range, cross range, and altitude measurements were shown to be sufficient for navigation. Research could be performed to explore the effect of alternate or addition measurements incorporated into the measurement model.

Finally, having a reference image available to cross correlate with an online image during measurement extraction is a large assumption. In a deployable system, perfect reference images may not be available. As such, future research could explore more robust methods of incorporating target location information into the measurement extraction algorithm.

REFERENCES

[1] C. Lindstrom, R. Christensen, and J. Gunther, "An Investigation of GPS-Denied Navigation Using Airborne Radar Telemetry," in *2020 IEEE/ION Position, Location and Navigation Symposium (PLANS)*, Apr. 2020, pp. 168–176, iSSN: 2153-3598, ©2020 IEEE. Reprinted, with permission.

[2] ——, "Sensitivity of BPA SAR Image Formation to Initial Position, Velocity, and Attitude Navigation Errors," *arXiv:2009.10210 [eess]*, Sep. 2020, arXiv: 2009.10210, Submitted to IEEE. Copyright subject to change without notice.

[3] I. G. Cumming and F. H. Wong, *Digital Processing of Synthetic Aperture Radar Data*.

[4] P. S. Maybeck, *Stochastic Models, Estimation, and Control*. New York: Navtech Book and Software Store, 1994, vol. 1.

[5] C. Ben and T. Islam, "Field study of a 24 GHz FMCW radar system suitable to detect small-sized RPAS under 5 kg MTOW," 2015.

[6] D. O. Nitti, F. Bovenga, M. T. Chiaradia, M. Greco, and G. Pinelli, "Feasibility of Using Synthetic Aperture Radar to Aid UAV Navigation," *Sensors*, vol. 15, no. 8, pp. 18 334–18 359, Aug. 2015. [Online]. Available: https://www.mdpi.com/1424-8220/15/8/18334

[7] M. Greco, K. Kulpa, G. Pinelli, and P. Samczynski, "SAR and InSAR georeferencing algorithms for inertial navigation systems," in *Photonics Applications in Astronomy, Communications, Industry, and High-Energy Physics Experiments 2011*, vol. 8008. International Society for Optics and Photonics, Oct. 2011, p. 80081O. [Online]. Available: https://www.spiedigitallibrary.org/conference-proceedings-of-spie/8008/80081O/SAR-and-InSAR-georeferencing-algorithms-for-inertial-navigation-systems/10.1117/12.904971.short

[8] A. F. Scannapieco, A. Renga, and A. Moccia, "Compact millimeter wave FMCW InSAR for UAS indoor navigation," in *2015 IEEE Metrology for Aerospace (MetroAeroSpace)*, Jun. 2015, pp. 551–556.

[9] E. B. Quist and R. W. Beard, "Radar odometry on fixed-wing small unmanned aircraft," *IEEE Transactions on Aerospace and Electronic Systems*, vol. 52, no. 1, pp. 396–410, Feb. 2016.

[10] E. Quist, "UAV Navigation and Radar Odometry," Ph.D. dissertation, Mar. 2015. [Online]. Available: https://scholarsarchive.byu.edu/etd/4439

[11] P. C. Niedfeldt, E. B. Quist, and R. W. Beard, "Characterizing range progression of SAR point scatterers with recursive RANSAC," in *2014 IEEE Radar Conference*, May 2014, pp. 0712–0717.

[12] E. B. Quist, P. C. Niedfeldt, and R. W. Beard, "Radar odometry with recursive-RANSAC," *IEEE Transactions on Aerospace and Electronic Systems*, vol. 52, no. 4, pp. 1618–1630, Aug. 2016.

[13] K. Kauffman, J. Raquet, Y. Morton, and D. Garmatyuk, "Enhanced feature detection and tracking algorithm for UWB-OFDM SAR navigation," in *Proceedings of the 2011 IEEE National Aerospace and Electronics Conference (NAECON)*, Jul. 2011, pp. 261–269.

[14] R. Christensen, J. Gunther, and D. Long, "Toward GPS-denied Navigation Utilizing Back Projection-based Synthetic Aperture Radar Images," in *Proceedings of the ION 2019 Pacific PNT Meeting*, Apr. 2019, pp. 108–119. [Online]. Available: https://doi.org/10.33012/2019.16797

[15] M. I. Duersch and D. G. Long, "Analysis of time-domain back-projection for stripmap SAR," *International Journal of Remote Sensing*, vol. 36, no. 8, pp. 2010–2036, Apr. 2015, publisher: Taylor & Francis _eprint: https://doi.org/10.1080/01431161.2015.1030044. [Online]. Available: https://doi.org/10.1080/01431161.2015.1030044

[16] G. Balamurugan, J. Valarmathi, and V. P. S. Naidu, "Survey on uav navigation in gps denied environments," in *2016 International Conference on Signal Processing, Communication, Power and Embedded System (SCOPES)*, 2016, pp. 198–204.

[17] R. Christensen, J. Gunther, and D. Long, "Radar-Aided, GPS-Denied Navigation."

[18] R. Bamler, "A comparison of range-Doppler and wavenumber domain SAR focusing algorithms," *IEEE Transactions on Geoscience and Remote Sensing*, vol. 30, no. 4, pp. 706–713, Jul. 1992. [Online]. Available: http://ieeexplore.ieee.org/document/158864/

[19] J. L. Farrell, J. H. Mims, and A. Sorrell, "Effects of Navigation Errors in Maneuvering SAR," *IEEE Transactions on Aerospace and Electronic Systems*, vol. AES-9, no. 5, pp. 758–776, Sep. 1973.

[20] V. C. Chen, "Time-frequency analysis of SAR images with ground moving targets," in *Wavelet Applications V*, vol. 3391. International Society for Optics and Photonics, Mar. 1998, pp. 295–302. [Online]. Available: https://www.spiedigitallibrary.org/conference-proceedings-of-spie/3391/0000/Time-frequency-analysis-of-SAR-images-with-ground-moving-targets/10.1117/12.304879.short

[21] J. Moreira, "Estimating the residual error of the reflectivity displacement method for aircraft motion error extraction from SAR raw data," in *IEEE International Conference on Radar*, May 1990, pp. 70–75.

[22] M. Xing, X. Jiang, R. Wu, F. Zhou, and Z. Bao, "Motion Compensation for UAV SAR Based on Raw Radar Data," *IEEE Transactions on Geoscience and Remote Sensing*, vol. 47, no. 8, pp. 2870–2883, Aug. 2009, conference Name: IEEE Transactions on Geoscience and Remote Sensing.

[23] S. Bing, W. Ye, C. Jie, W. Yan, and L. Bing, "Image position analysis of motion errors for missile-borne SAR based on diving model," in *2013 IEEE International Conference on Imaging Systems and Techniques (IST)*, Oct. 2013, pp. 206–209, iSSN: 1558-2809.

[24] M. S. Grewal, A. P. Andrews, and C. Bartone, *Global navigation satellite systems, inertial navigation, and integration*, third edition ed. Hoboken: John Wiley & Sons, 2013.

[25] J. Farrell, *Aided navigation: GPS with high rate sensors*, ser. Electronic engineering. New York: McGraw-Hill, 2008, oCLC: ocn212908814.

[26] P. G. Savage, *Strapdown analytics*. Maple Plain, Minn.: Strapdown Associates, 2000.

[27] R. Zanetti, "Rotations, Transformations, Left Quaternions, Right Quaternions?" *The Journal of the Astronautical Sciences*, vol. 66, no. 3, pp. 361–381, Sep. 2019. [Online]. Available: http://link.springer.com/10.1007/s40295-018-00151-2

[28] J. Hollowell, "Heli/SITAN: a terrain referenced navigation algorithm for helicopters," in *IEEE Symposium on Position Location and Navigation. A Decade of Excellence in the Navigation Sciences*, Mar. 1990, pp. 616–625. [Online]. Available: http://ieeexplore.ieee.org/lpdocs/epic03/wrapper.htm?arnumber=66236

[29] N. Bergman, L. Ljung, and F. Gustafsson, "Terrain navigation using Bayesian statistics," *IEEE Control Systems Magazine*, vol. 19, no. 3, pp. 33–40, Jun. 1999. [Online]. Available: http://ieeexplore.ieee.org/lpdocs/epic03/wrapper.htm?arnumber=768538

[30] P.-J. Nordlund and F. Gustafsson, "Marginalized Particle Filter for Accurate and Reliable Terrain-Aided Navigation," *IEEE Transactions on Aerospace and Electronic Systems*, vol. 45, no. 4, pp. 1385–1399, Oct. 2009. [Online]. Available: http://ieeexplore.ieee.org/lpdocs/epic03/wrapper.htm?arnumber=5310306

[31] Long Zhao, Nan Gao, Baoqi Huang, Qingyun Wang, and Jianhua Zhou, "A Novel Terrain-Aided Navigation Algorithm Combined With the TERCOM Algorithm and Particle Filter," *IEEE Sensors Journal*, vol. 15, no. 2, pp. 1124–1131, Feb. 2015. [Online]. Available: http://ieeexplore.ieee.org/lpdocs/epic03/wrapper.htm?arnumber=6913541

[32] S. Jiang, B. Wang, M. Xiang, X. Fu, X. Sun, X. Hu, and Q. Qian, "The InSAR/INS Integrated Navigation Based on Interferograms Matching," in *EUSAR 2018; 12th European Conference on Synthetic Aperture Radar*, Jun. 2018, pp. 1–4.

[33] Y. Kim, J. Park, and H. Bang, "Terrain-Referenced Navigation using an Interferometric Radar Altimeter: IRA-Based TRN," *Navigation*, vol. 65, no. 2, pp. 157–167, Jun. 2018. [Online]. Available: http://doi.wiley.com/10.1002/navi.233

[34] Z. Sjanic and F. Gustafsson, "Simultaneous navigation and SAR auto-focusing," in *2010 13th International Conference on Information Fusion*, Jul. 2010, pp. 1–7. [Online]. Available: http://ieeexplore.ieee.org/document/5711931/

[35] L. Fabbrini, M. Messina, M. Greco, and G. Pinelli, "Linear landmark extraction in SAR images with application to augmented integrity aero-navigation: an overview to a novel processing chain," in *Proc. SPIE 8008, Photonics Applications in Astronomy, Communications, Industry, and High-Energy Physics Experiments 201*, Jun. 2011, p. 80081P. [Online]. Available: http://proceedings.spiedigitallibrary.org/proceeding.aspx?doi=10.1117/12.905022

[36] M. Greco, G. Pinelli, K. Kulpa, P. Samczynski, B. Querry, and S. Querry, "The study on SAR images exploitation for air platform navigation purposes," in *2011 12th International Radar Symposium (IRS)*, Sep. 2011, pp. 347–352.

[37] M. Greco, S. Querry, G. Pinelli, K. Kulpa, P. Samczynski, D. Gromek, A. Gromek, M. Malanowski, B. Querry, and A. Bonsignore, "SAR-based augmented integrity navigation architecture," in *2012 13th International Radar Symposium*, May 2012, pp. 225–229. [Online]. Available: http://ieeexplore.ieee.org/document/6233320/

[38] M. Divak, "Simulated SAR with GIS Data and Pose Estimation using Affine Projection," Ph.D. dissertation, Lulea University of Technology, 2017.

[39] A. F. Scannapieco, A. Renga, G. Fasano, and A. Moccia, "Experimental Analysis of Radar Odometry by Commercial Ultralight Radar Sensor for Miniaturized UAS," *Journal of Intelligent & Robotic Systems*, vol. 90, no. 3, pp. 485–503, Jun. 2018. [Online]. Available: https://doi.org/10.1007/s10846-017-0688-1

[40] A. F. Scannapieco, "A novel outlier removal method for two-dimensional radar odometry," *Sonar Navigation IET Radar*, vol. 13, no. 10, pp. 1705–1712, 2019.

[41] M. Mostafa, S. Zahran, A. Moussa, N. El-Sheimy, and A. Sesay, "Radar and Visual Odometry Integrated System Aided Navigation for UAVS in GNSS Denied Environment," *Sensors*, vol. 18, no. 9, p. 2776, Sep. 2018. [Online]. Available: https://www.mdpi.com/1424-8220/18/9/2776

[42] K. J. Kauffman, "Fast Target Tracking Technique for Synthetic Aperture Radars," Ph.D. dissertation, Miami University, 2009. [Online]. Available: http://rave.ohiolink.edu/etdc/view?acc_num=miami1250263416

[43] K. Kauffman, Y. Morton, J. Raquet, and D. Garmatyuk, "Simulation Study of UWB-OFDM SAR for Dead-Reckoning Navigation," in *Proceedings of the 2010 International Technical Meeting of The Institute of Navigation*, 2010.

[44] K. Kauffman, J. Raquet, Y. Morton, and D. Garmatyuk, "Simulation study of UWB-OFDM SAR for navigation using an extended Kalman filter," in *Proceedings of ION GNSS*, 2010.

[45] K. Kauffman, J. Raque, Y. Morton, and D. Garmatyuk, "Simulation Study of UWB-OFDM SAR for Navigation with INS Integration," in *Proceedings of the 2011 International Technical Meeting of The Institute of Navigation*, 2011.

[46] K. Kauffman, Y. Morton, J. Raquet, and D. Garmatyuk, "Experimental Study of UWB-OFDM SAR for Indoor Navigation with INS Integration," in *25th International Technical Meeting of the Satellite Division of the Insitute of Navigation*, 2012.

[47] K. Kauffman, Y. Morton, and D. Garmatyuk, "Experimental Study of Two-channel UWB-OFDM Radar for Indoor Navigation with INS Integration," in *Proceedings of the 26th International Technical Meeting of The Satellite Division of the Institute of Navigation*, Nashville, TN, 2013.

[48] K. Kauffman, J. Raquet, Y. Morton, and D. Garmatyuk, "Real-Time UWB-OFDM Radar-Based Navigation in Unknown Terrain," *IEEE Transactions on Aerospace and Electronic Systems*, vol. 49, no. 3, pp. 1453–1466, Jul. 2013.

[49] P. Samczynski and K. Kulpa, "Coherent MapDrift Technique," *IEEE Transactions on Geoscience and Remote Sensing*, vol. 48, no. 3, pp. 1505–1517, Mar. 2010. [Online]. Available: http://ieeexplore.ieee.org/document/5308453/

[50] P. Samczynski, "Superconvergent Velocity Estimator for an Autofocus Coherent MapDrift Technique," *IEEE Geoscience and Remote Sensing Letters*, vol. 9, no. 2, pp. 204–208, Mar. 2012. [Online]. Available: http://ieeexplore.ieee.org/document/6018248/

[51] A. Sharif and I. Cumming, "Doppler centroid estimation for azimuth-offset SARS," in *Proceedings of the IEEE 1995 National Aerospace and Electronics Conference. NAECON 1995*, vol. 1, May 1995, pp. 134–139 vol.1, iSSN: 0547-3578.

[52] F.-k. Li, D. N. Held, J. C. Curlander, and C. Wu, "Doppler Parameter Estimation for Spaceborne Synthetic-Aperture Radars," *IEEE Transactions on Geoscience and Remote Sensing*, vol. GE-23, no. 1, pp. 47–56, Jan. 1985, conference Name: IEEE Transactions on Geoscience and Remote Sensing.

[53] S.-J. Wei, X.-L. Zhang, and J. Shi, "An autofocus approach for model error correction in compressed sensing SAR imaging," in *2012 IEEE International Geoscience and Remote Sensing Symposium*, Jul. 2012, pp. 3987–3990, iSSN: 2153-7003.

[54] M. Jensen, C. Knight, and B. Haslem, "FlexSAR, a high quality, flexible, cost effective, prototype SAR system," in *Radar Sensor Technology XX*, vol. 9829. International Society for Optics and Photonics, May 2016, p. 98290A. [Online]. Available: https://www.spiedigitallibrary.org/conference-proceedings-of-spie/9829/98290A/FlexSAR-a-high-quality-flexible-cost-effective-prototype-SAR-system/10.1117/12.2224951.short

[55] Novatel GNSS/INS Module: SPAN-CPT Single Enclosure GNSS/INS Receiver. [Online]. Available: http://www.novatel.com/products/span-gnss-inertial-navigation-systems.

[56] Honeywell Precision Barometer and Altimeter (HPB/HPA). [Online]. Available: http://www.aerospace.honeywell.com/ en/learn/products/sensors/honeywell-precision-barometer-and-altimeter.

[57] F. Berizzi and G. Corsini, "Autofocusing of inverse synthetic aperture radar images using contrast optimization," *IEEE Transactions on Aerospace and Electronic Systems*, vol. 32, no. 3, pp. 1185–1191, Jul. 1996, conference Name: IEEE Transactions on Aerospace and Electronic Systems.

APPENDICES

APPENDIX A

Kalman Filter Verification and Debugging Process

A.1 State Vector Mappings and Validation

The three state vectors, the truth state $\mathbf{x}$, the estimated state $\hat{\mathbf{x}}$, and the error state $\delta\mathbf{x}$, can be related to each other through the following three mappings.

$$\mathbf{x} = l(\hat{\mathbf{x}}, \delta\mathbf{x}) \tag{A.1}$$

$$\hat{\mathbf{x}} = m(\mathbf{x}, \delta\mathbf{x}) \tag{A.2}$$

$$\delta\mathbf{x} = n(\hat{\mathbf{x}}, \mathbf{x}) \tag{A.3}$$

Each of these mappings can be explained intuitively. The mapping $\mathbf{x} = l(\hat{\mathbf{x}}, \delta\mathbf{x})$ can be thought of as a function that produces the truth state by adding a small perturbation to the estimated state. In other words, it removes the error from the estimated state. The mapping $\hat{\mathbf{x}} = m(\mathbf{x}, \delta\mathbf{x})$ can be thought of as adding an error to the truth state to create the estimated state. The mapping $\delta\mathbf{x} = n(\hat{\mathbf{x}}, \mathbf{x})$ is a measurement of how much error exists between truth and estimated states.

The above mappings are defined as follows

$$\mathbf{x} = l(\hat{\mathbf{x}}, \delta\mathbf{x}) = \begin{bmatrix} \mathbf{p}^{ned} = \hat{\mathbf{p}}^{ned} + \delta\mathbf{p}^{ned} \\ \mathbf{v}^{ned} = \hat{\mathbf{v}}^{ned} + \delta\mathbf{v}^{ned} \\ q_b^{ned} = \begin{bmatrix} 1 \\ -\frac{1}{2}\delta\theta_b^{ned} \end{bmatrix} \otimes q_{\hat{b}}^{ned} \\ \mathbf{b}_{accel} = \hat{\mathbf{b}}_{accel} + \delta\mathbf{b}_{accel} \\ \mathbf{b}_{gyro} = \hat{\mathbf{b}}_{gyro} + \delta\mathbf{b}_{gyro} \\ b_{alt} = \hat{b}_{alt} + \delta b_{alt} \\ b_{range} = \hat{b}_{range} + \delta b_{range} \\ b_{rate} = \hat{b}_{rate} + \delta b_{rate} \end{bmatrix} \tag{A.4}$$

$$\hat{\mathbf{x}} = m(\mathbf{x}, \delta\mathbf{x}) = \begin{bmatrix} \hat{\mathbf{p}}^{ned} = \mathbf{p}^{ned} - \delta\mathbf{p}^{ned} \\ \hat{\mathbf{v}}^{ned} = \mathbf{v}^{ned} - \delta\mathbf{v}^{ned} \\ q_{\hat{b}}^{ned} = \begin{bmatrix} 1 \\ \frac{1}{2}\delta\theta_b^{ned} \end{bmatrix} \otimes q_b^{ned} \\ \hat{\mathbf{b}}_{accel} = \mathbf{b}_{accel} - \delta\mathbf{b}_{accel} \\ \hat{\mathbf{b}}_{gyro} = \mathbf{b}_{gyro} - \delta\mathbf{b}_{gyro} \\ \hat{b}_{alt} = b_{alt} - \delta b_{alt} \\ \hat{b}_{range} = b_{range} - \delta b_{range} \\ \hat{b}_{rate} = b_{rate} - \delta b_{rate} \end{bmatrix} \tag{A.5}$$

$$\delta\mathbf{x} = n(\hat{\mathbf{x}}, \mathbf{x}) = \begin{bmatrix} \delta\mathbf{p}^{ned} = \mathbf{p}^{ned} - \hat{\mathbf{p}}^{ned} \\ \delta\mathbf{v}^{ned} = \mathbf{v}^{ned} - \hat{\mathbf{v}}^{ned} \\ \delta\theta_b^{ned} = -2 \cdot (q_b^{ned} \otimes (q_{\hat{b}}^{ned})^*)_{2:4} \\ \delta\mathbf{b}_{accel} = \mathbf{b}_{accel} - \hat{\mathbf{b}}_{accel} \\ \delta\mathbf{b}_{gyro} = \mathbf{b}_{gyro} - \hat{\mathbf{b}}_{gyro} \\ \delta\mathbf{b}_{alt} = \mathbf{b}_{alt} - \hat{\mathbf{b}}_{alt} \\ \delta\mathbf{b}_{range} = \mathbf{b}_{range} - \hat{\mathbf{b}}_{range} \\ \delta\mathbf{b}_{rate} = \mathbf{b}_{rate} - \hat{\mathbf{b}}_{rate} \end{bmatrix} \tag{A.6}$$

where $\otimes$ denotes the quaternion multiplication operator, * denotes the quaternion conjugate,

and the $2:4$ subscript refers to elements 2 through 4 of the resulting quaternion. All other variables are defined in the main body of the thesis.

These mappings can be validated to ensure consistency between all three states. To clarify, this validation step validates the relationships between the states and does not validate correct implementation of the states themselves. This validation step was performed on the state vectors in Chapter 3. To perform the validation of the above mappings for the truth, estimated, and error states, the mappings were programmed into MATLAB, and the following steps were taken.

1. An initial error state, $\delta\mathbf{x}$, and an initial truth state $\mathbf{x}$ were defined. The error state was formed using a random number generator. Both the error state and the truth state are shown in Table A.1.

Table A.1: Defining truth and error state.

	Position	Velocity	Attitude	Bias Accel	Bias Gyro	Bias Alt	Bias Range	Bias Rate
$\mathbf{x}$	(1000,0,-500)	(50,0,0)	(1,0,0,0)	(0.228,0.436,0.311)	(0.923,0.430,0.184)	0.905	0.980	0.221
$\delta\mathbf{x}$	(0.379,0.812,0.533)	(0.351,0.939,0.876)	(0.018,0.021,0.020)	(0.208,0.301,0.471)	(0.230,0.844,0.195)	0.226	0.171	0.101

2. The initial truth states and error states were fed into the function $m(\mathbf{x}, \delta\mathbf{x})$ to produce a test estimate state, which is denoted as $\hat{\mathbf{x}}'$. The result is shown in Table A.2.

Table A.2: Estimated state.

	Position	Velocity	Attitude	Bias Accel	Bias Gyro	Bias Alt	Bias Range	Bias Rate
$\hat{\mathbf{x}}'$	(999.621,-0.812,-500.533)	(49.649,-0.939,-0.876)	(0.999,0.009,0.010,0.010)	(0.020,0.135,-0.160)	(0.693,-0.414,-0.010)	0.679	0.809	0.120

3. The initial truth state and $\hat{\mathbf{x}}'$ were fed into the function $n(\hat{\mathbf{x}}', \mathbf{x})$ to produce a test error state, which is denoted as $\delta\mathbf{x}'$. The difference between the initial error state, $\delta\mathbf{x}$, and test error state, $\delta\mathbf{x}'$, was then calculated. This is shown in Table A.3. The result of the difference was close to zero, which validates the error state mapping.

4. The test estimate state and initial error state were fed into the function $l(\hat{\mathbf{x}}', \delta\mathbf{x})$ to produce a test truth state, which is denoted as $\mathbf{x}'$. The difference between the test

Table A.3: Difference between defined error with calculated error.

	Position	Velocity	Attitude	Bias Accel	Bias Gyro	Bias Alt	Bias Range	Bias Rate
$\delta\mathbf{x}$	(0.379,0.812,0.533)	(0.351,0.939,0.876)	(0.018,0.021,0.020)	(0.208,0.301,0.471)	(0.230,0.844,0.195)	0.226	0.171	0.101
$\delta\mathbf{x}'$	(0.379,0.812,0.533)	(0.351,0.939,0.876)	(0.018,0.021,0.020)	(0.208,0.301,0.471)	(0.231,0.844,0.195)	0.226	0.171	0.101
$\delta\mathbf{x} - \delta\mathbf{x}'$	(0,0,0)	(0,0,0)	(-0.264e-5,-0.298e-5,-0.281e-5)	(0,0,0)	(0,0,0)	0	0	0

truth state, $\mathbf{x}'$, and the initial truth state, $\mathbf{x}$, was calculated. This is shown in Table A.4. The difference was sufficiently close to zero, which validates the truth state mapping.

Table A.4: Difference between defined truth and calculated truth.

	Position	Velocity	Attitude	Bias Accel	Bias Gyro	Bias Alt	Bias Range	Bias Rate
$\mathbf{x}$	(1000,0,-500)	(50,0,0)	(1,0,0,0)	(0.228,0.436,0.311)	(0.923,0.430,0.184)	0.905	0.980	0.221
$\mathbf{x}'$	(1000,0,-500)	(50,0,0)	(1,0,0,0)	(0.228,0.436,0.311)	(0.923,0.430,0.184)	0.905	0.980	0.221
$\mathbf{x} - \mathbf{x}'$	(0,0,0)	(0,0,0)	(0,0,0,0)	(0,0,0)	(0,0,0)	0	0	0

A.2 Truth and Navigation State Propagation and Validation

To verify the consistency of the model definitions, each state propagation model and measurement model is simulated in MATLAB. For the purposes of this verification step, all noise sources and biases are set to zero. The simulation then propagates the truth state and estimated state using the truth model and navigation model, respectively. Without noise, the truth and navigation models should produce nearly the same results.

This verification step was performed on the models defined in Chapter 3. The simulation was provided with accelerometer and gyroscope data, which moves the model along a trajectory. In the absence of noise, the sensor data provided to the truth model and navigation model was identical. The trajectory defined by the sensor data is shown in Figure A.1.

After both models processed the sensor data, errors in position, velocity, and attitude are calculated using the $n(\hat{\mathbf{x}}, \mathbf{x})$ function defined in Section A.1. The resulting errors were plotting and are shown in Figure A.2. Notice the scale factor in the upper corner of each subfigure, which shows that these errors are very close to zero.

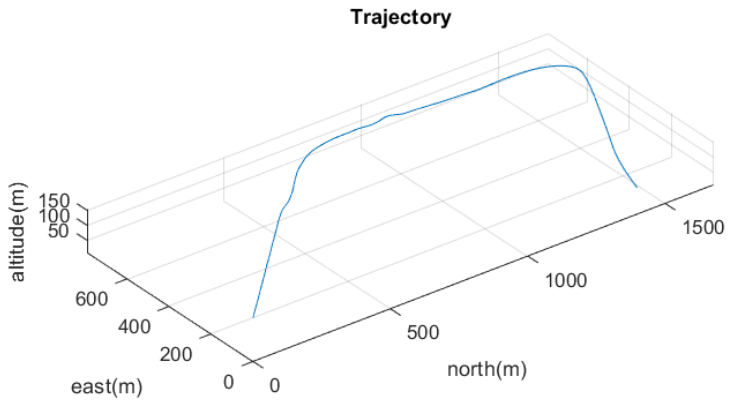

Fig. A.1: Trajectory of UAV using true measurements from an IMU.

As assumed at the beginning of the simulation, no noise or bias was added to the states or sensor measurements. Figure A.3 verifies zero bias throughout the simulation.

At each Kalman update time, measurements were taken using the sensor measurement function $\tilde{\mathbf{z}}$ and the estimate measurement function $\hat{\tilde{\mathbf{z}}}$. The difference between these measurements is called the residual measurement error and is shown in Figure A.4 for the range, range rate, and altimeter measurements. As with the position, velocity, and attitude errors, the residual errors are multiplied by a scale factor which produces near zero values for each measurement residual.

This process validated that the truth model and navigation models from Chapter 3 produce the same results in the absence of noise. In other words, the two models are consistent with each other.

A.3 Error State Propagation and Validation

This step validates the propagation of the error state. To do this, the error state is propagated forward in time using a non-linear model and a linear model. The difference between the non-linear and linear error states should be small.

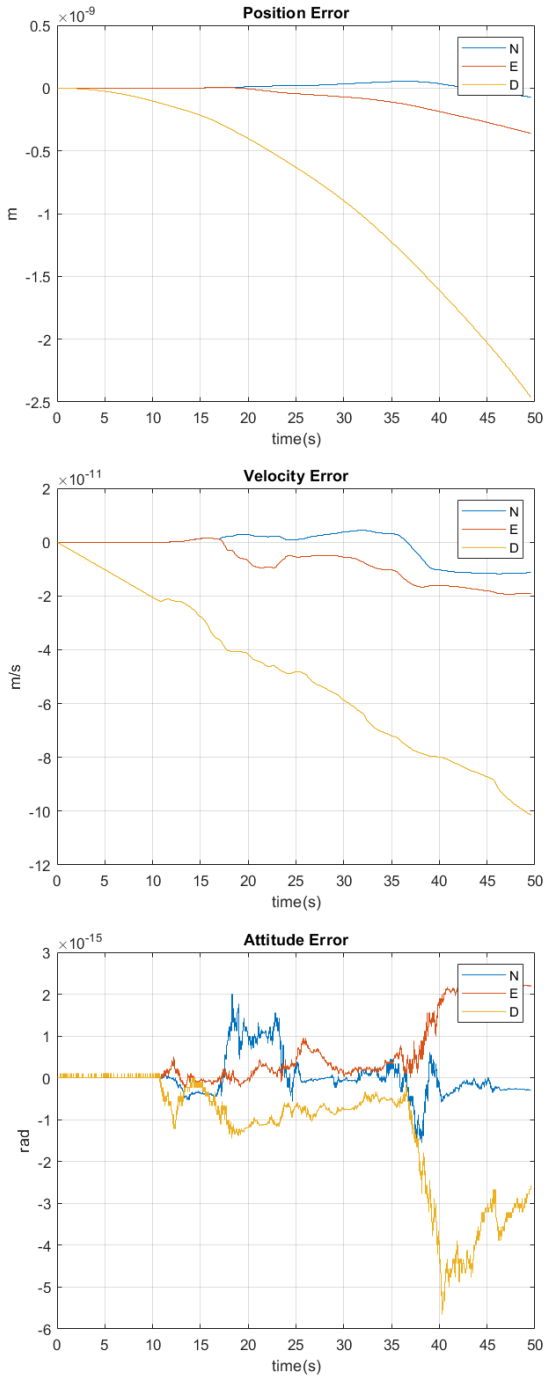

Fig. A.2: Errors in the position, velocity, and attitude between the truth and navigation models.

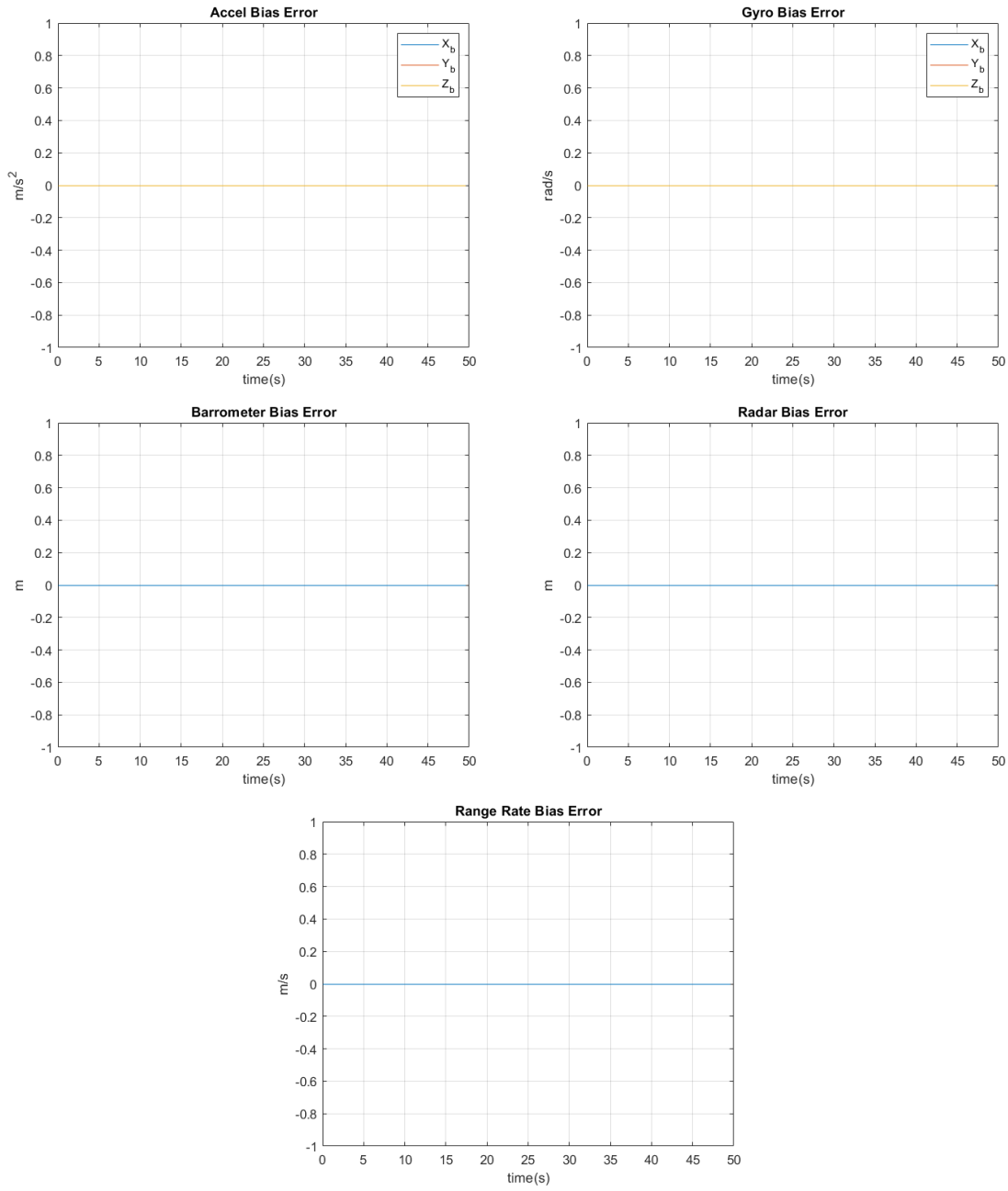

Fig. A.3: Errors of the bias states, which are all zero with no noise propagation.

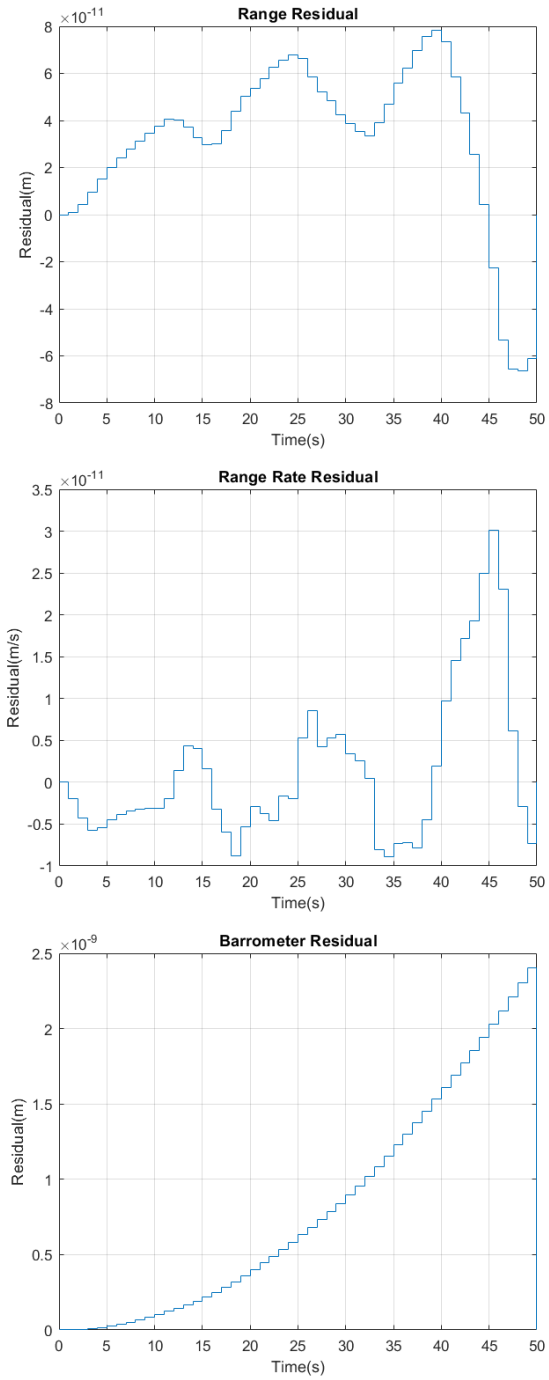

Fig. A.4: Residual errors between the true measurements and estimated measurements.

The nonlinear error state can be found be propagating the non-linear truth and navigation models forward in time and calculating the error between the two models. This is done using the already validated $n(\hat{\mathbf{x}}, \mathbf{x})$ mapping. Note that the non-linear truth and navigation models have also already been validated.

The linear error state is propagated using the linear model defined by the $\hat{F}$ matrix. This matrix is developed through linearizing the truth model about the estimated state. The linear error state at time t is calculated using the $\hat{F}$ matrix as $\delta\dot{\mathbf{x}} = \hat{F}\delta\mathbf{x}$. The same initial error used in the nonlinear error propagation is used to initialize the linear error model. The model is then propagated forward in time for t seconds. This results in a linear error state at time t.

The nonlinear and linear error states are compared to each other for accuracy. The $\hat{F}$ is considered validated is the difference between the nonlinear and linear error states is "small"[1]. This validation process was performed on the $\hat{F}$ matrix from Chapter 3 and the results are shown in Table A.5.

For this application, the errors are considered small enough. Thus, the linear error model is validated and is consistent with the definitions of the nonlinear truth and navigation models.

A.4 Linear Measurement Validation

The difference between $\tilde{\mathbf{z}}$ and $\hat{\tilde{\mathbf{z}}}$ is called the measurement "residual" and will be denoted $\delta\mathbf{z}$. The residual is important in the EKF to calculate an updated error state vector. The residual is used in this section to validate the H matrix in the linear measurement model. For purposes of validation, let $\delta\mathbf{z}_{nl}$ to be the nonlinear measurement residual and $\delta\mathbf{z}_{l}$ to be

[1]The word "small" must be interpreted differently for each new application. In any case, the difference between the two error states will be non-zero, because the linear error model does not account for higher order error terms.

Table A.5: Validation of $\hat{F}$ matrix using a comparison of nonlinear and linear error states at time t.

state	delx_linear	delx_nonlinear	propError
p_x	1.2027	1.202	0.00070823
p_y	2.1446	2.1429	0.0017244
p_z	3.2835	3.2849	-0.0013857
v_x	0.30566	0.30424	0.001419
v_y	0.089675	0.086234	0.0034411
v_z	0.26791	0.27067	-0.002767
θ_x	0.0099969	0.0099951	1.7465e-06
θ_y	0.020009	0.020006	3.3867e-06
θ_z	0.030013	0.030008	5.3278e-06
$b_{accel,x}$	0.0080317	0.0080317	0
$b_{accel,y}$	0.016063	0.016063	0
$b_{accel,z}$	0.024095	0.024095	0
$b_{gyro,x}$	3.9693e-06	3.9693e-06	0
$b_{gyro,y}$	7.9386e-06	7.9386e-06	0
$b_{gyro,z}$	1.1908e-05	1.1908e-05	0
b_{alt}	0.81873	0.81873	0
b_{range}	1.6375	1.6375	0
b_{rate}	1.2281	1.2281	0

the linear measurement residual. These residuals are defined by

$$\delta\mathbf{z}_{nl} = \tilde{\mathbf{z}} - \hat{\tilde{\mathbf{z}}} \tag{A.7}$$

$$\delta\mathbf{z}_{l} = H\delta\mathbf{x} \tag{A.8}$$

In Section A.3, the $\hat{F}$ matrix was validated by calculating errors using nonlinear propagation and comparing the results with errors calculated using linear propagation. A similar method can be employed to validate the H matrix. An error, $\delta\mathbf{x}$ is injected into the truth model. Measurements for $\tilde{\mathbf{z}}$ and $\hat{\tilde{\mathbf{z}}}$ are made and an H matrix is calculated. Just as in validating $\hat{F}$, this validation is done in the absence of process and measurement noise.

With values for $\tilde{\mathbf{z}}$, $\hat{\tilde{\mathbf{z}}}$, and H, the nonlinear residual $\delta\mathbf{z}_{nl}$ and the linear residual $\delta\mathbf{z}_{l}$ are calculated. The two residual measurements are compared with each other. If the difference between the two residuals is "small" then the H matrix is validated.

This validation step was used on the measurement model from Chapter 3, and the

results have been provided. Table A.6 shows the results of the validation process. The error between the two residual calculations is several orders of magnitude smaller than the measurements $\tilde{\mathbf{z}}$ and $\hat{\tilde{\mathbf{z}}}$, which are on the order of hundreds of meters. The difference between the nonlinear and linear residuals is considered small enough in this case. Therefore, the H matrix in the linear measurement model is validated.

Table A.6: Validation of H matrix by calculating the difference between linear and nonlinear residual measurements.

	residual_linear	residual_nonlinear	resError
Range	-0.49928	-0.49676	-0.0025155
Range Rate	1.2466	1.2472	-0.00057447
Altitude	-2	-2	0

A.5 Covariance Propagation Validation

This section provides details on validating the covariance propagation equations. This validation step was again applied to the model in Chapter 3. To validate the propagation of the error state covariance in the presence of noise, the following steps are performed.

- An initial state covariance $P(t_0)$ is defined.
- Errors consistent with the initial state covariance are injected into the estimated state $\hat{\mathbf{x}}$.
- The matrices $\hat{F}, B$, and Q are calculated.
- The covariance is propagated forward in time without Kalman updates.
- The truth state and estimated state are propagated forward in time without Kalman updates. The error between the truth and estimated states is calculated.
- The propagation of covariance and state vectors repeats several times to perform a Monte Carlo simulation.
- Hairline plots from the Monte Carlo simulation are created.

- 3σ bounds are created from the covariance propagation. If the propagation errors from the truth and estimated states are contained within the 3σ bounds, then the covariance propagation is validated.

To begin, an initial state covariance is defined $P(t_0)$. The diagonals of $P(t_0)$ contain variances for each error state, denoted $\sigma^2_{\delta\mathbf{x}_i}$ where $\delta\mathbf{x}_i$ represents the i^{th} component of the error state vector. With these variances, $P(t_0)$ is equal to,

$$P(t_0) = \begin{bmatrix} \sigma^2_{\delta\mathbf{p}^{ned}} & 0_{3\times3} & 0_{3\times3} & 0_{3\times3} & 0_{3\times3} & 0_{3\times1} & 0_{3\times1} & 0_{3\times1} \\ 0_{3\times3} & \sigma^2_{\delta\mathbf{v}^{ned}} & 0_{3\times3} & 0_{3\times3} & 0_{3\times3} & 0_{3\times1} & 0_{3\times1} & 0_{3\times1} \\ 0_{3\times3} & 0_{3\times3} & \sigma^2_{\delta\theta_b^{ned}} & 0_{3\times3} & 0_{3\times3} & 0_{3\times1} & 0_{3\times1} & 0_{3\times1} \\ 0_{3\times3} & 0_{3\times3} & 0_{3\times3} & \sigma^2_{\delta\mathbf{b}_{accel}} & 0_{3\times3} & 0_{3\times1} & 0_{3\times1} & 0_{3\times1} \\ 0_{3\times3} & 0_{3\times3} & 0_{3\times3} & 0_{3\times3} & \sigma^2_{\delta\mathbf{b}_{gyro}} & 0_{3\times1} & 0_{3\times1} & 0_{3\times1} \\ 0_{1\times3} & 0_{1\times3} & 0_{1\times3} & 0_{1\times3} & 0_{1\times3} & \sigma^2_{\delta b_{alt}} & 0 & 0 \\ 0_{1\times3} & 0_{1\times3} & 0_{1\times3} & 0_{1\times3} & 0_{1\times3} & 0 & \sigma^2_{\delta b_{range}} & 0 \\ 0_{1\times3} & 0_{1\times3} & 0_{1\times3} & 0_{1\times3} & 0_{1\times3} & 0 & 0 & \sigma^2_{\delta b_{rate}} \end{bmatrix} \tag{A.9}$$

In simulation, values for the error state are set by the user. Table A.7 shows the values selected for this validation step. These values are in terms of 3σ values, denoted $\sigma_{3s,\delta\mathbf{x}_i}$.

Table A.7: 3σ values selected by the user for this validation step.

3σ (State)	Value
$\sigma_{3s,\delta\mathbf{p}^{ned}}$	diag([1, 1, 3]) (m)
$\sigma_{3s,\delta\mathbf{v}^{ned}}$	diag([0.1, 0.1, 0.1]) (m/s)
$\sigma_{3s,\delta\theta_b^{ned}}$	diag([0.1, 0.1, 0.1]) (rad)
$\sigma_{3s,\delta\mathbf{b}_{accel}}$	diag([0.001, 0.001, 0.001]) (g)
$\sigma_{3s,\delta\mathbf{b}_{gyro}}$	diag([1, 1, 1]) (deg/hr)
$\sigma_{3s,\delta\mathbf{b}_{alt}}$	0.1 (m)
$\sigma_{3s,\delta\mathbf{b}^{range}}$	0.1 (m)
$\sigma_{3s,\delta\mathbf{b}^{rate}}$	0.1 (m/s)

Errors can be generated using standard normal random variables. Let $y \sim \mathcal{N}(0,1)$. An

error δx_i in the error state vector $\delta\mathbf{x}$ can be generated as [2] $\delta x_i = y\sigma_{ss,\delta x_i}$. These δx_i errors are then injected into the initial estimated state $\hat{\mathbf{x}}$.

Recall the equation for the power spectral density Q.

$$Q = \begin{bmatrix} \sigma^2_{vrw} I_{3\times3} & 0_{3\times3} & 0_{3\times3} & 0_{3\times3} & 0_{3\times1} & 0_{3\times1} & 0_{3\times1} \\ 0_{3\times3} & \sigma^2_{arw} I_{3\times3} & 0_{3\times3} & 0_{3\times3} & 0_{3\times1} & 0_{3\times1} & 0_{3\times1} \\ 0_{3\times3} & 0_{3\times3} & \frac{2\sigma^2_{ss,b_{accel}}}{\tau_{accel}} I_{3\times3} & 0_{3\times3} & 0_{3\times1} & 0_{3\times1} & 0_{3\times1} \\ 0_{3\times3} & 0_{3\times3} & 0_{3\times3} & \frac{2\sigma^2_{ss,b_{gyro}}}{\tau_{gyro}} I_{3\times3} & 0_{3\times1} & 0_{3\times1} & 0_{3\times1} \\ 0_{3\times3} & 0_{3\times3} & 0_{3\times3} & 0_{3\times3} & \frac{2\sigma^2_{ss,b_{alt}}}{\tau_{alt}} & 0 & 0 \\ 0_{1\times3} & 0_{1\times3} & 0_{1\times3} & 0_{1\times3} & 0 & \frac{2\sigma^2_{ss,b_{range}}}{\tau_{range}} & 0 \\ 0_{1\times3} & 0_{1\times3} & 0_{1\times3} & 0_{1\times3} & 0 & 0 & \frac{2\sigma^2_{ss,b_{rate}}}{\tau_{rate}} \end{bmatrix} \tag{A.10}$$

In simulation, each of the noise variances in Q is selected by the user in terms of 3σ values. The 3σ values used for this validation step are shown in Table A.8.

Table A.8: 3σ noise values used for covariance propagation validation.

3σ (Noise)	Values
$\sigma_{3s,vrw}$	0.06 (m/s/sqrt(hr))
$\sigma_{3s,arw}$	0.07 (deg/sqrt(hr))
$\sigma_{3s,b_{accel}}$	0.001 (g)
$\sigma_{3s,b_{gyro}}$	1 (deg/hr)
$\sigma_{3s,b_{alt}}$	0.1 (m)
$\sigma_{3s,b_{range}}$	0.1 (m)
$\sigma_{3s,b_{rate}}$	0.1 (m)

Given the values for the initial covariance P, the injected errors $\delta\mathbf{x}$, and the power spectral density Q, a Monte Carlo simulation is run to validate the covariance propagation. The Monte Carlo simulation was run 200 times. The results of the simulation are given in Figures A.5 through A.10.

[2] This is the expression for generating continuous noise. In software, the noise is discrete. To simulate the discrete samples of a continuous noise process, the actual calculation is $\delta x_i = y\sqrt{\frac{\sigma^2_{3s,\delta x_i}}{\Delta t}}$ where Δt is the simulation sampling rate.

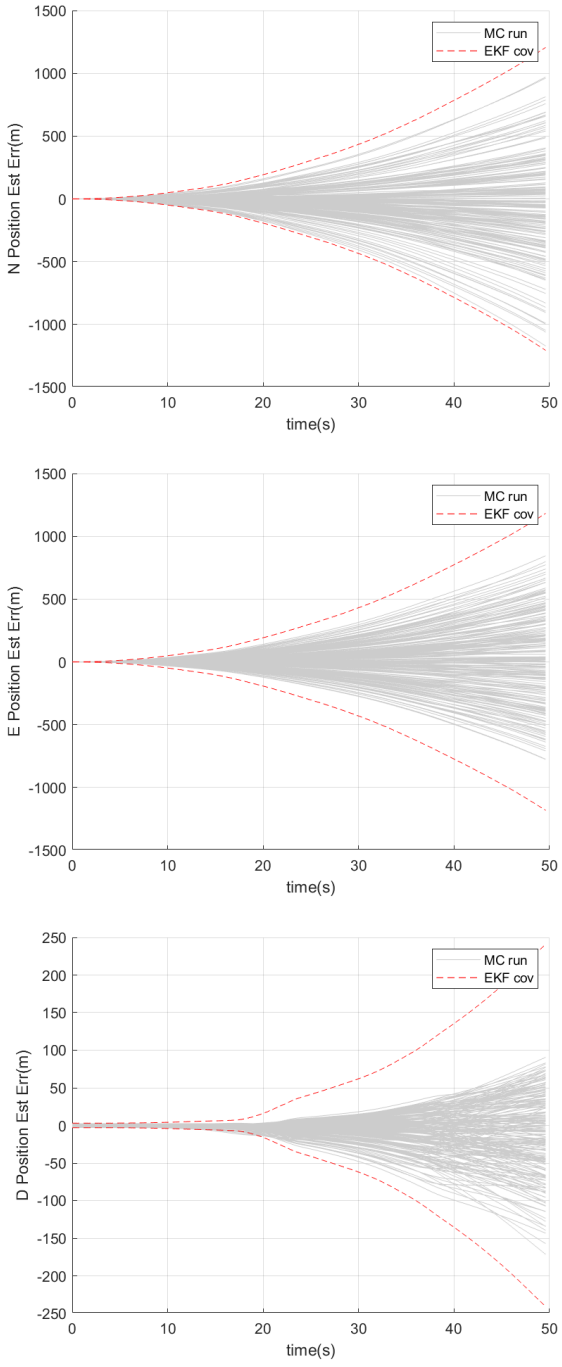

Fig. A.5: Hairline plot showing the propagation errors in position. From top to bottom: North position error, east position error, down position error.

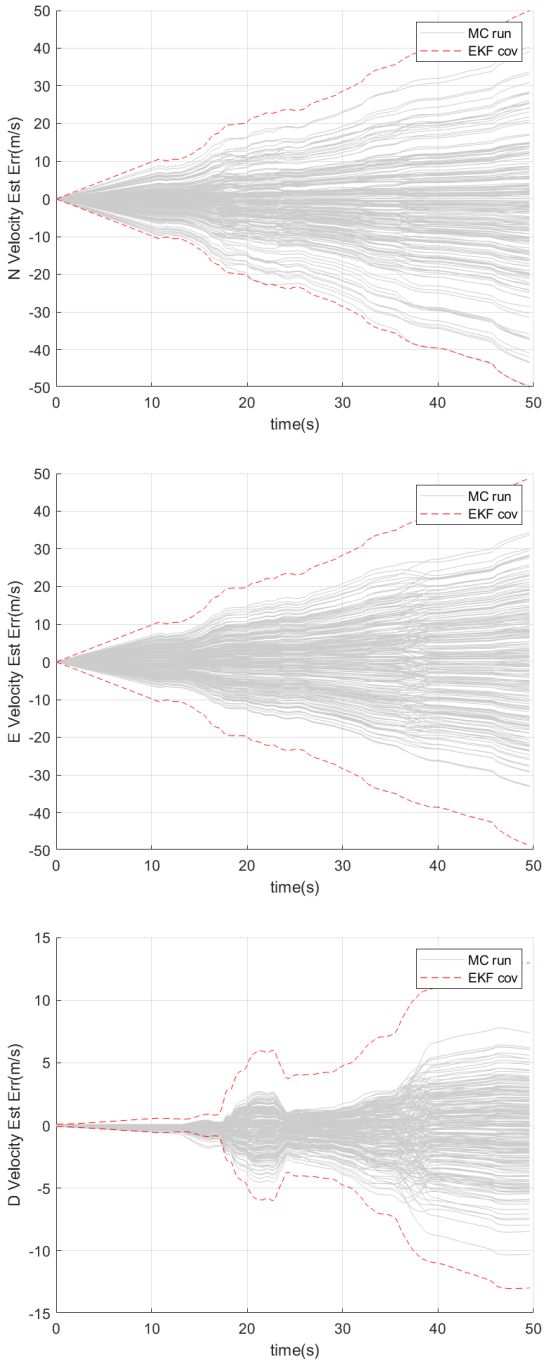

Fig. A.6: Hairline plot showing the propagation errors in velocity. From top to bottom: North velocity error, east velocity error, down velocity error.

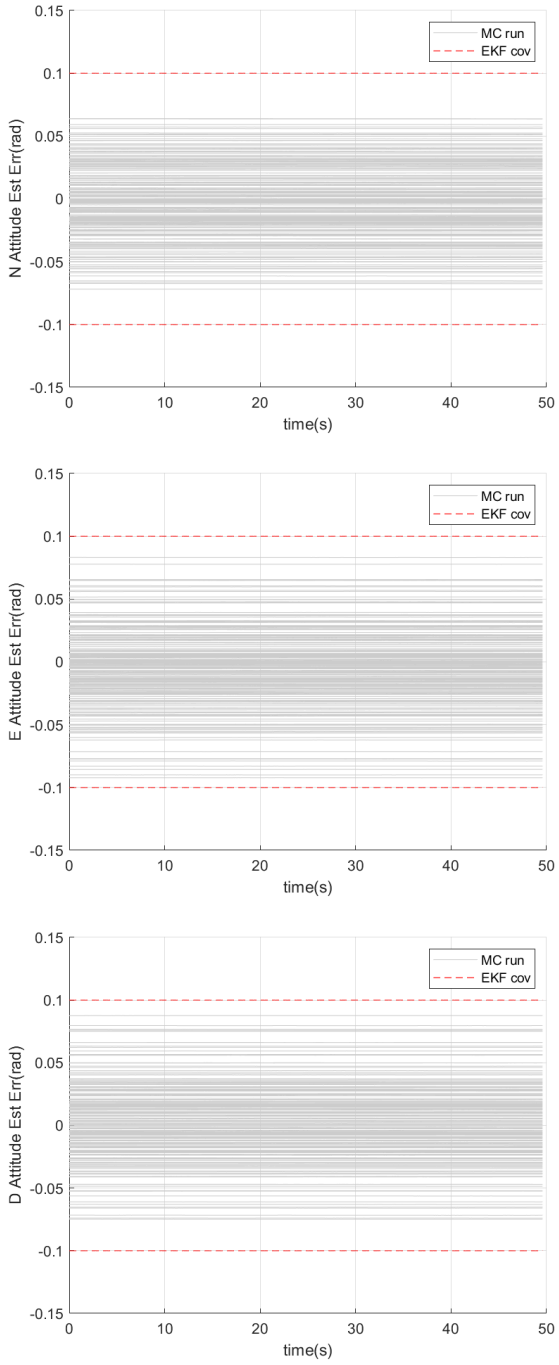

Fig. A.7: Hairline plot showing the propagation errors in attitude. From top to bottom: North attitude error, east attitude error, down attitude error.

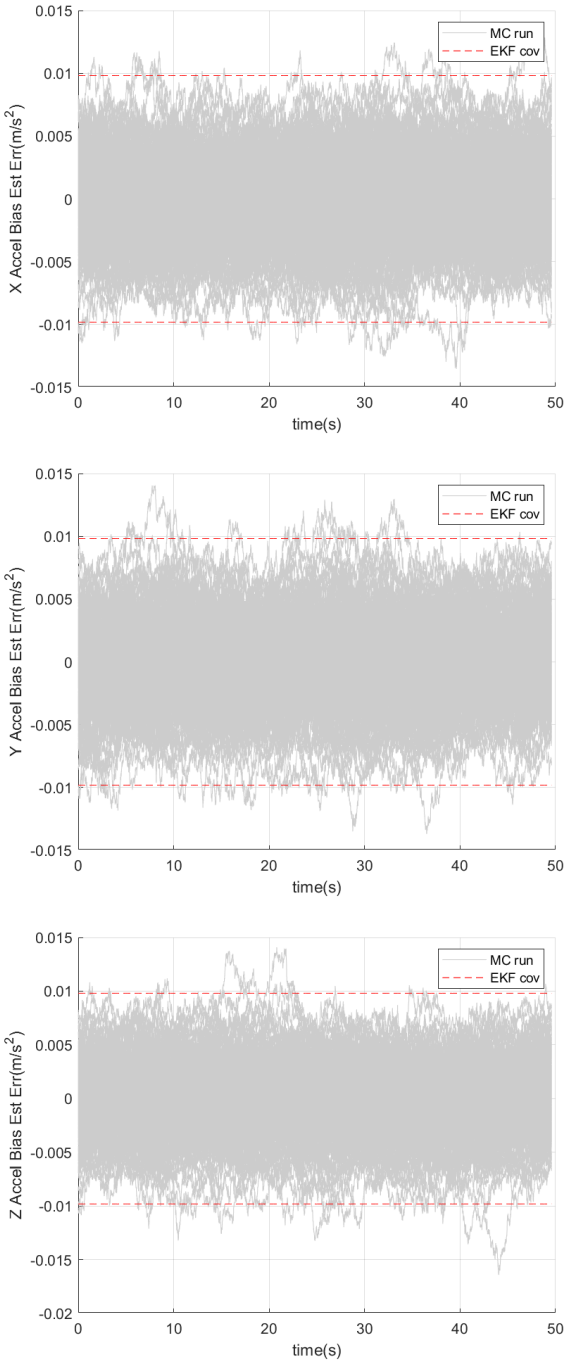

Fig. A.8: Hairline plot showing the propagation errors in accelerometer bias. From top to bottom: X accelerometer bias error, Y accelerometer bias error, Z accelerometer bias error.

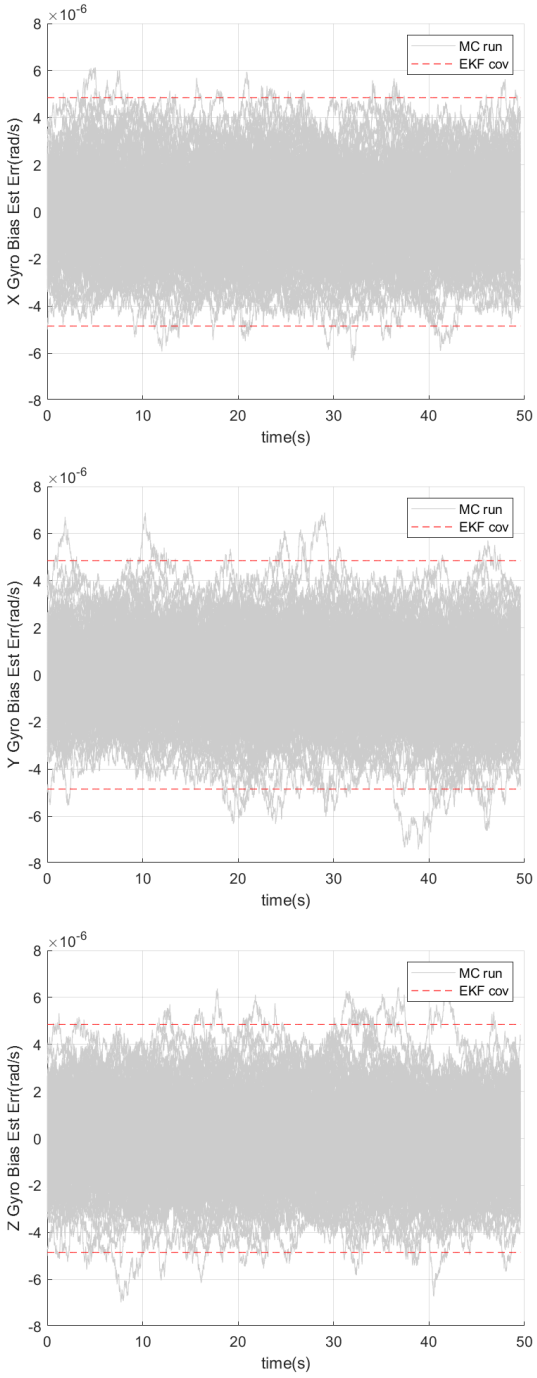

Fig. A.9: Hairline plot showing the propagation errors in gyroscope bias. From top to bottom: X gyroscope bias error, Y gyroscope bias error, Z gyroscope bias error.

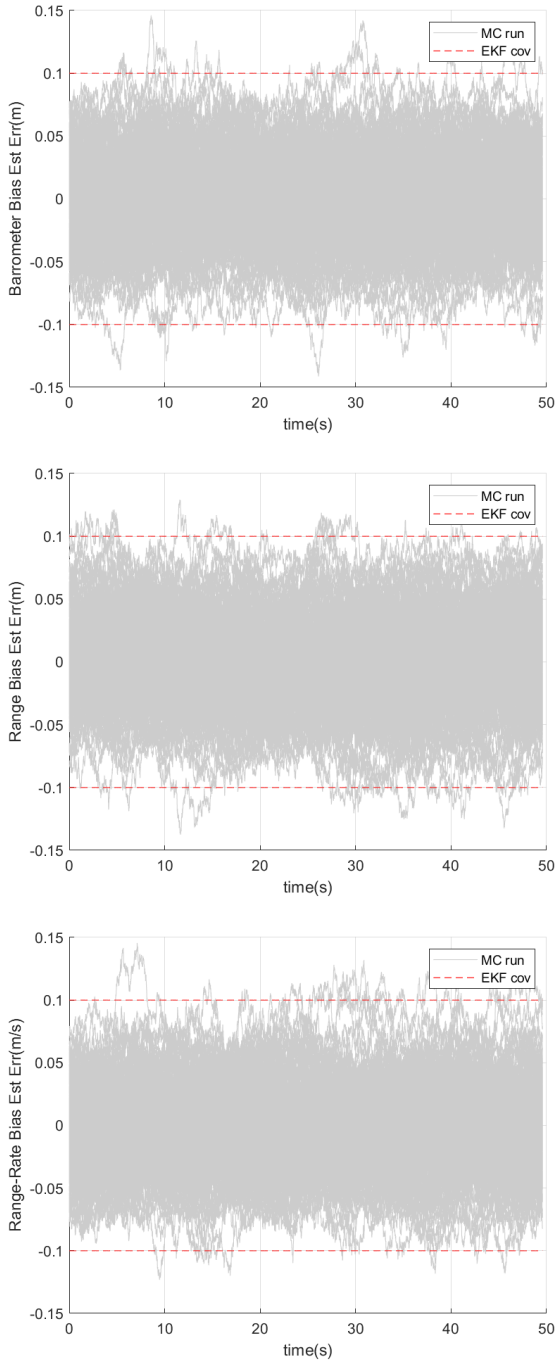

Fig. A.10: Hairline plot showing the propagation errors in altimeter, range, and range-rate biases. From top to bottom: Altimeter bias error, range bias error, range-rate bias error.

Each hairline plot shows 3σ error bounds denoted by the dotted lines. These bounds are calculated using the error state covariance matrix P. Each hair in the hairline plot is a single run of the Monte Carlo simulation. Because the bounds are 3σ bounds, most of the hairs should remain in the bounds with the occasional outlier. For 200 runs of the Monte Carlo simulation, the resulting errors are within bounds. This validates the propagation of the error state covariance matrix.

A.6 Kalman Update Validation

This section validates the equations from the previous section. Before validation, an R matrix is selected, which determines the noise variances of the radar and altimeter measurements. For this section, R is equal to

$$R = \begin{bmatrix} \sigma^2_{\tilde{z}_{range}} & 0 & 0 \\ 0 & \sigma^2_{\tilde{z}_{rate}} & 0 \\ 0 & 0 & \sigma^2_{\tilde{z}_{alt}} \end{bmatrix} \tag{A.11}$$

where $\sigma_{\tilde{z}_i} = \sigma_{3s,\tilde{z}_i}/3$ and where the $\sigma_{3s,\tilde{z}_i}$ are selected by the user and are defined in Table A.9.

Table A.9: Noise standard deviations used for SAR and altimeter measurement noises.

3σ (Measurement)	Values
$\sigma_{\tilde{z}_{radar}}$	0.2 (m)
$\sigma_{\tilde{z}_{rate}}$	0.2 (m/s)
$\sigma_{\tilde{z}_{alt}}$	0.2 (m)

If implemented correctly, the Kalman filter should produce residual measurements that are zero-mean and white. After a single Monte Carlo run, the residual measurements with their associated covariances were plotted. These plots are shown in Figure A.11. As in Section A.5, the solid line represents a single Monte Carlo run and the dotted line represents the 3σ bounds of the measurement residual.

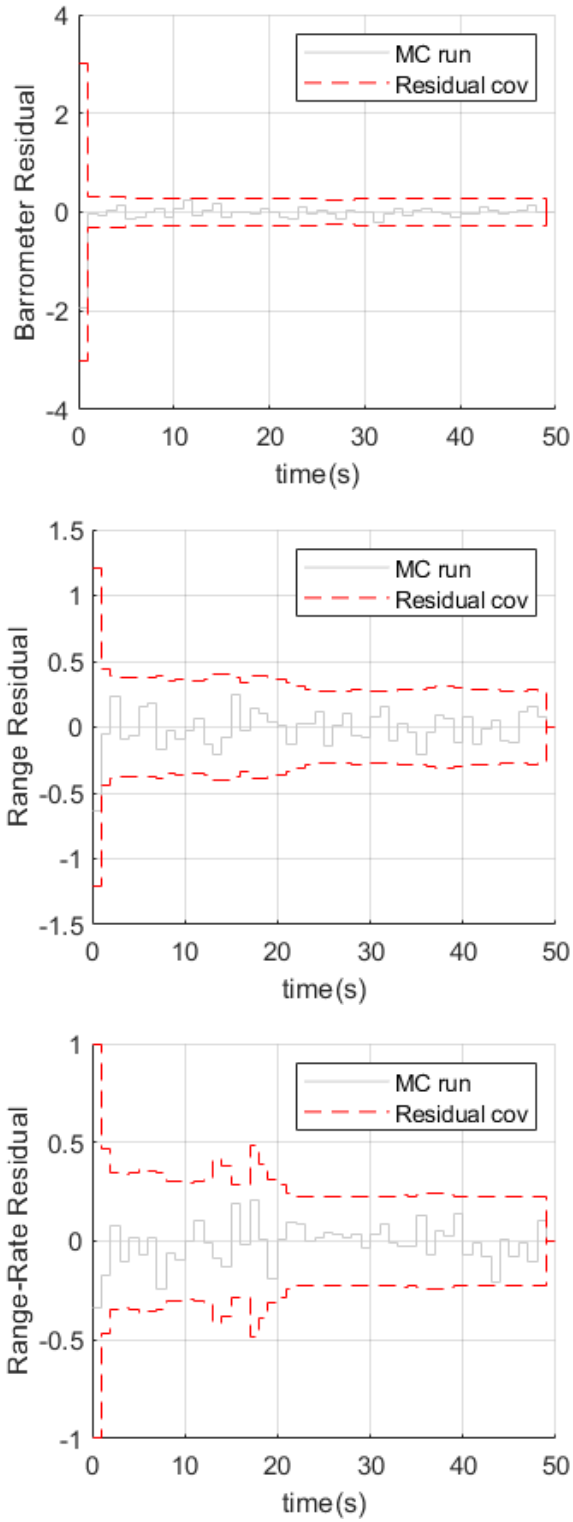

Fig. A.11: Residual measurements after implementation of Kalman updates. From top to bottom: Altimeter residual, range residual, range-rate residual.

It was observed that the measurement residuals satisfy the zero-mean and white conditions. To further validate correct implementation of the Kalman update equations, a Monte Carlo simulation with 200 runs was performed. Hair plots of the propagation error were created as was done in Section A.5. These plots are shown in Figures A.12 through A.17. Note how the covariance of the error state (indicated by the dotted line) changes in tandem with the actual state errors. This further implies correct implementation.

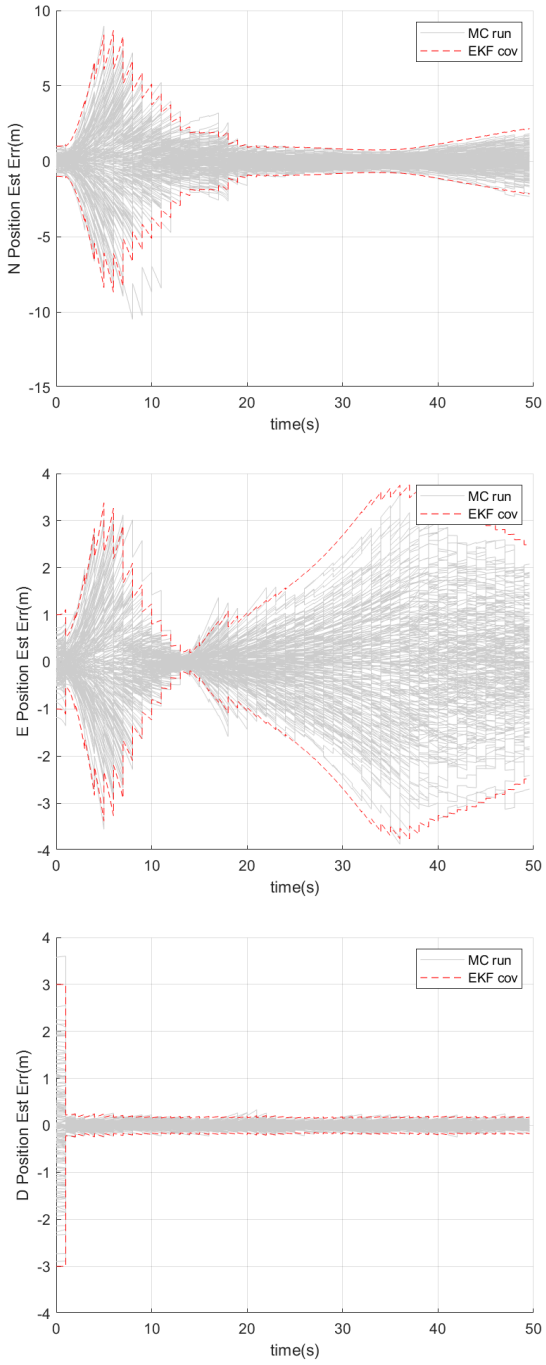

Fig. A.12: State error propagation after Kalman updates. From top to bottom: North position error, east position error, down position error.

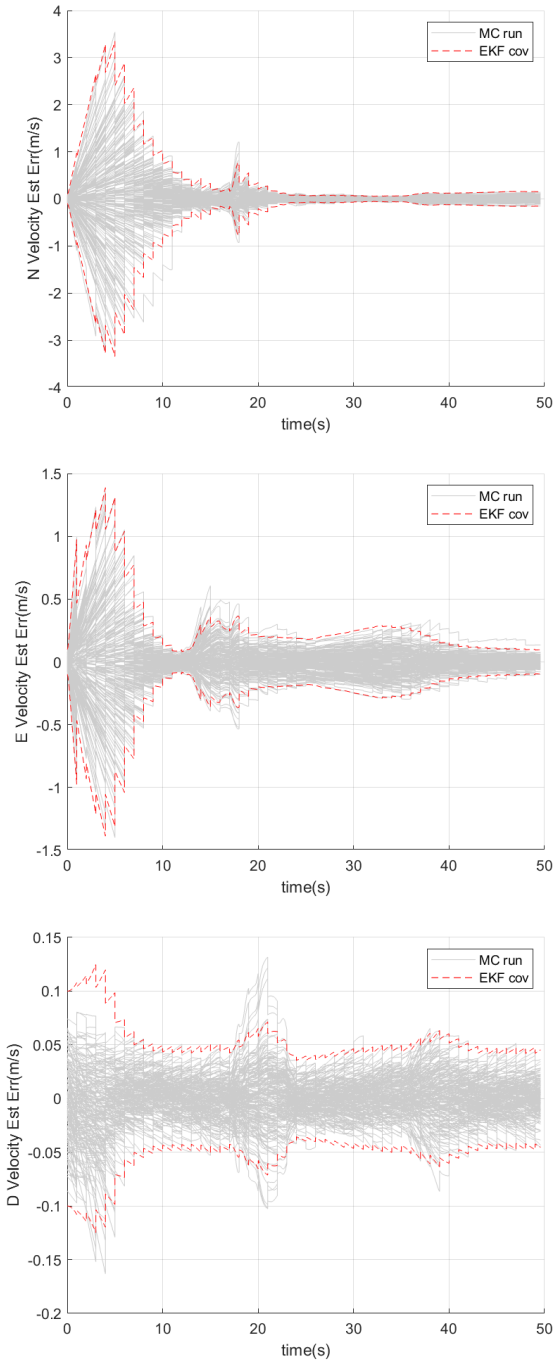

Fig. A.13: State error propagation after Kalman updates. From top to bottom: North velocity error, east velocity error, down velocity error.

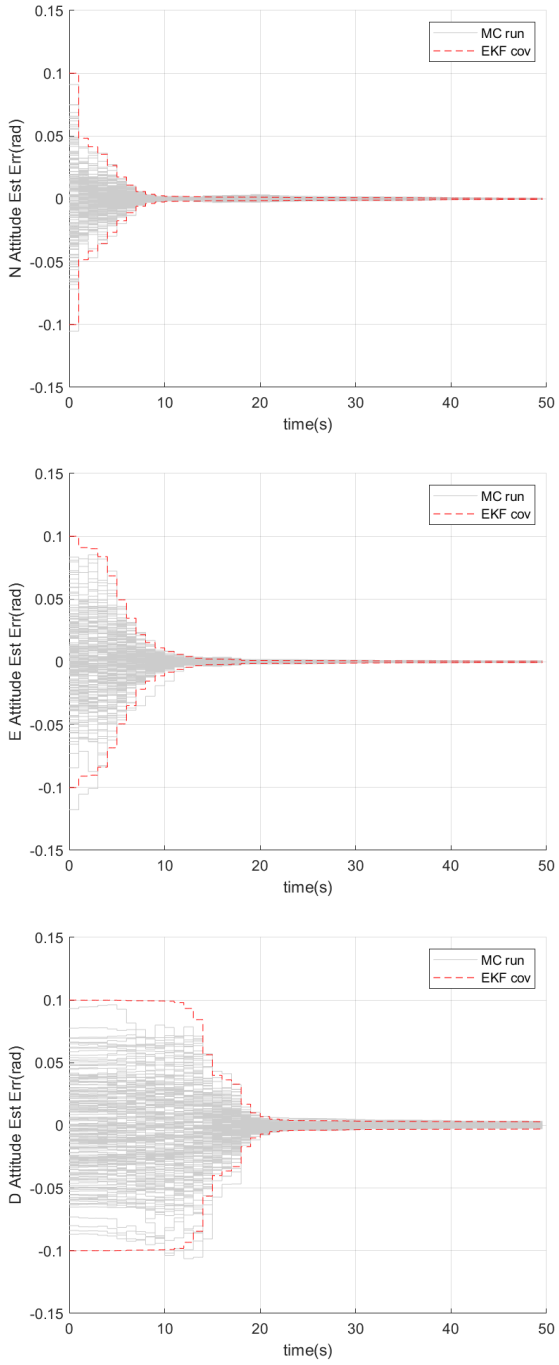

Fig. A.14: State error propagation after Kalman updates. From top to bottom: North attitude error, east attitude error, down attitude error.

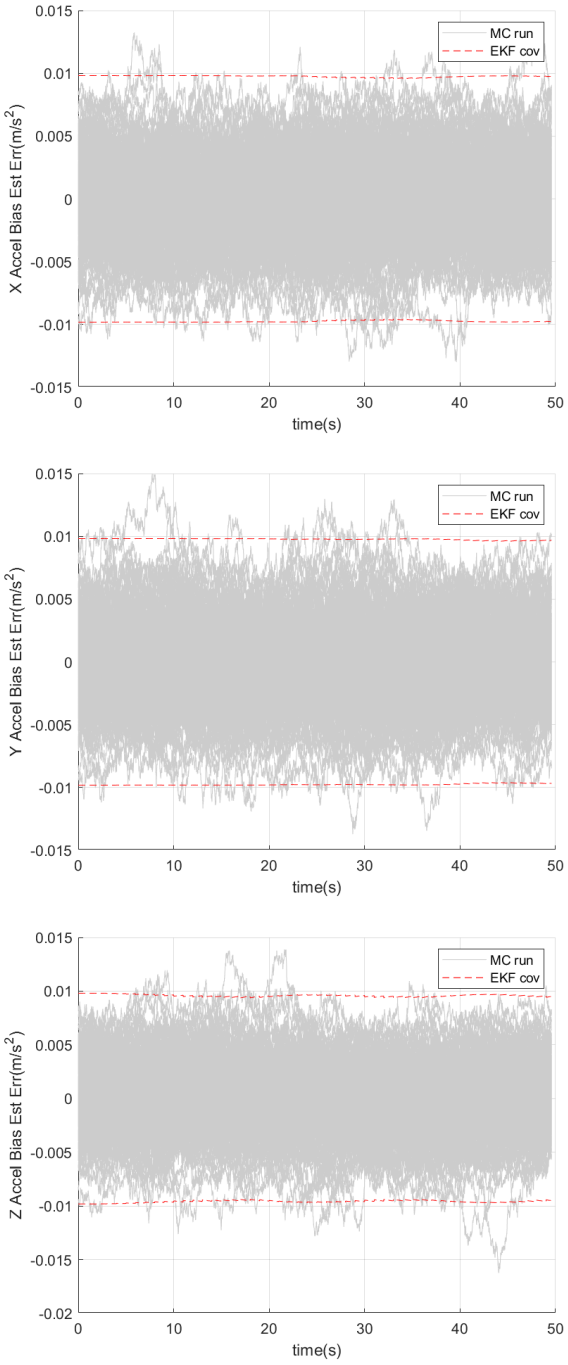

Fig. A.15: State error propagation after Kalman updates. From top to bottom: X accelerometer bias error, Y accelerometer bias error, Z accelerometer bias error.

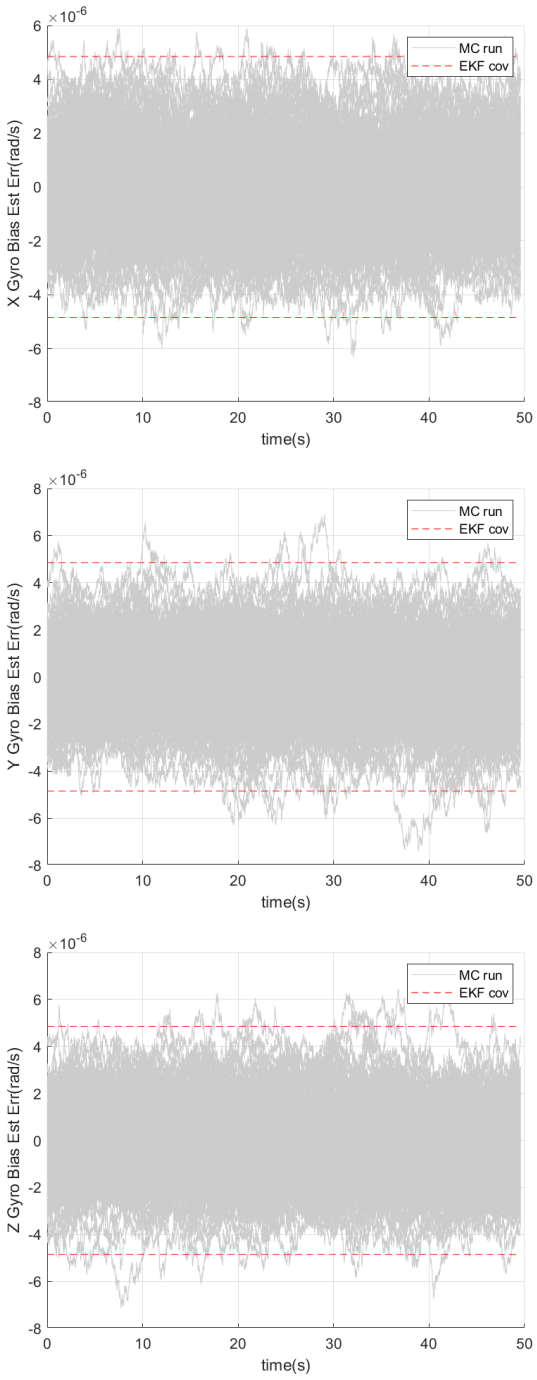

Fig. A.16: State error propagation after Kalman updates. From top to bottom: X gyroscope bias error, Y gyroscope bias error, Z gyroscope bias error.

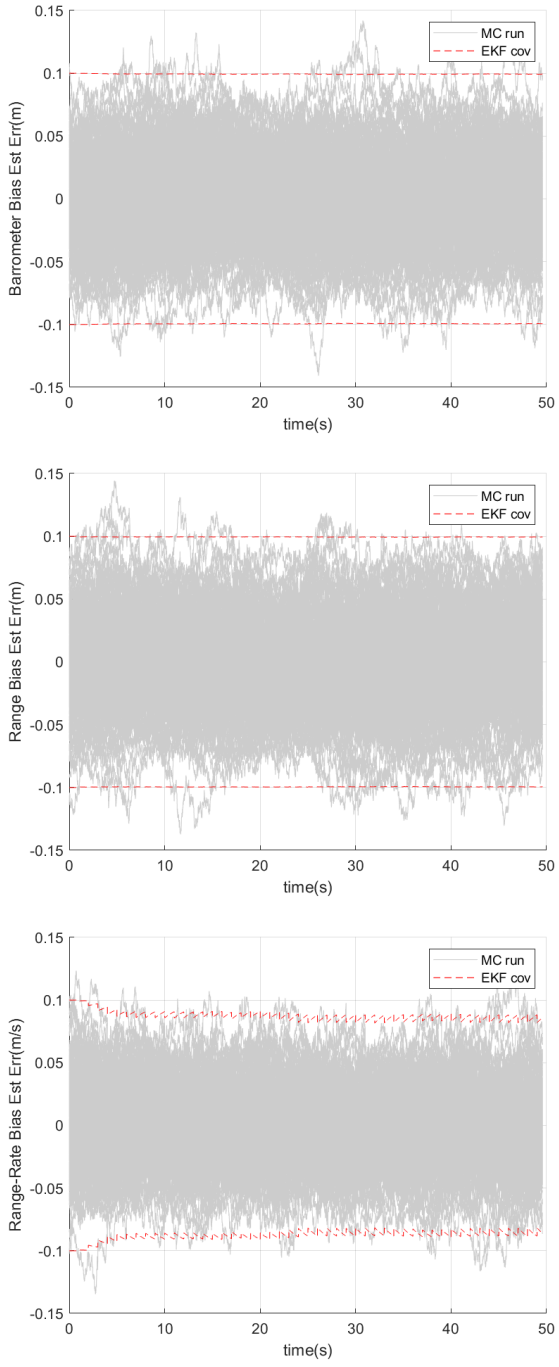

Fig. A.17: State error propagation after Kalman updates. From top to bottom: Altimeter bias error, range, range-rate bias error.

APPENDIX B

EKF Related Derivations

This section contains derivations for portions of the EKF used in Chapters 3 and 5.

B.1 Linearization of Velocity State

The linearized velocity state arises when linearizing the truth state about the estimated state to form a linear error model. The linearization process begins with

$$\dot{\hat{\mathbf{v}}}^{ned} + \delta\dot{\mathbf{v}}^{ned} = (I - (\delta\theta_b^{ned}\times))R_{\hat{b}}^{ned}(\hat{\nu}^b - \hat{\mathbf{b}}_{accel} - \delta\mathbf{b}_{accel} - \mathbf{n}_\nu) + g^{ned} \tag{B.1}$$

The goal is to write an expression for the linear error model, $\delta\dot{\mathbf{v}}$. Expanding the equation produces

$$\dot{\hat{\mathbf{v}}}^{ned} + \delta\dot{\mathbf{v}}^{ned} = R_{\hat{b}}^{ned}(\hat{\nu}^b - \hat{\mathbf{b}}_{accel} - \delta\mathbf{b}_{accel} - \mathbf{n}_\nu) - (\delta\theta_b^{ned}\times)R_{\hat{b}}^{ned}(\hat{\nu}^b - \hat{\mathbf{b}}_{accel} - \delta\mathbf{b}_{accel} - \mathbf{n}_\nu) \tag{B.2}$$

Subtracting the estimated state and reversing the order of the cross product results in

$$\delta\dot{\mathbf{v}}^{ned} = R_{\hat{b}}^{ned}(-\delta\mathbf{b}_{accel} - \mathbf{n}_\nu) + [R_{\hat{b}}^{ned}(\hat{\nu}^b - \hat{\mathbf{b}}_{accel} - \delta\mathbf{b}_{accel} - \mathbf{n}_\nu)] \times \delta\theta_b^{ned} \tag{B.3}$$

Neglecting second order terms results in the expression used in the linear error model in Chapters 3 and 5.

$$\begin{aligned}\delta\dot{\mathbf{v}}^{ned} =& R_{\hat{b}}^{ned}(-\delta\mathbf{b}_{accel} - \mathbf{n}_\nu) + [R_{\hat{b}}^{ned}(\hat{\nu}^b - \hat{\mathbf{b}}_{accel})] \times \delta\theta_b^{ned} \\ =& [R_{\hat{b}}^{ned}(\hat{\nu}^b - \hat{\mathbf{b}}_{accel})] \times \delta\theta_b^{ned} - R_{\hat{b}}^{ned}\delta\mathbf{b}_{accel} - R_{\hat{b}}^{ned}\mathbf{n}_\nu)\end{aligned} \tag{B.4}$$

B.2 Linearization of Attitude State

The linearized attitude state again arises from linearizing the truth state to produce a linear error model. The process begins with

$$\frac{d}{dt}\left(\begin{bmatrix} 1 \\ -\frac{1}{2}\delta\theta_b^{ned} \end{bmatrix} \otimes q_{\hat{b}}^{ned}\right) = \frac{1}{2}\begin{bmatrix} 1 \\ -\frac{1}{2}\delta\theta_b^{ned} \end{bmatrix} \otimes q_{\hat{b}}^{ned} \otimes \begin{bmatrix} 0 \\ \hat{\omega}^b - \hat{\mathbf{b}}_{gyro} - \delta\mathbf{b}_{gyro} - \mathbf{n}_\omega \end{bmatrix} \tag{B.5}$$

For clarity, let $\delta q = \begin{bmatrix} 1 \\ -\frac{1}{2}\delta\theta_b^{ned} \end{bmatrix}$. This results in,

$$\frac{d}{dt}(\delta q \otimes q_{\hat{b}}^{ned}) = \frac{1}{2}\delta q \otimes q_{\hat{b}}^{ned} \otimes \begin{bmatrix} 0 \\ \hat{\omega}^b - \hat{\mathbf{b}}_{gyro} - \delta\mathbf{b}_{gyro} - \mathbf{n}_\omega \end{bmatrix} \tag{B.6}$$

Expanding the derivative on the left and splitting the quaternion on the right results in

$$\delta\dot{q} \otimes q_{\hat{b}}^{ned} + \delta q \otimes \dot{q}_{\hat{b}}^{ned} = \frac{1}{2}\delta q \otimes q_{\hat{b}}^{ned} \otimes \left(\begin{bmatrix} 0 \\ \hat{\omega}^b - \hat{\mathbf{b}}_{gyro} \end{bmatrix} + \begin{bmatrix} 0 \\ -\delta\mathbf{b}_{gyro} - \mathbf{n}_\omega \end{bmatrix}\right) \tag{B.7}$$

Distributing the quaternion multiplication on the right results in

$$\delta\dot{q} \otimes q_{\hat{b}}^{ned} + \delta q \otimes \dot{q}_{\hat{b}}^{ned} = \frac{1}{2}\delta q \otimes q_{\hat{b}}^{ned} \otimes \begin{bmatrix} 0 \\ \hat{\omega}^b - \hat{\mathbf{b}}_{gyro} \end{bmatrix} + \frac{1}{2}\delta q \otimes q_{\hat{b}}^{ned} \otimes \begin{bmatrix} 0 \\ -\delta\mathbf{b}_{gyro} - \mathbf{n}_\omega \end{bmatrix} \tag{B.8}$$

Recall from Chapters 3 and 5 that the expression for attitude in the navigation model is $\dot{q}_{\hat{b}}^{ned} = q_{\hat{b}}^{ned} \otimes \frac{1}{2}\begin{bmatrix} 0 \\ \tilde{\omega}^b - \hat{\mathbf{b}}_{gyro} \end{bmatrix}$ Substituting in the estimated attitude state results in

$$\delta\dot{q} \otimes q_{\hat{b}}^{ned} + \delta q \otimes \dot{q}_{\hat{b}}^{ned} = \delta q \otimes \dot{q}_{\hat{b}}^{ned} + \frac{1}{2}\delta q \otimes q_{\hat{b}}^{ned} \otimes \begin{bmatrix} 0 \\ -\delta\mathbf{b}_{gyro} - \mathbf{n}_\omega \end{bmatrix} \tag{B.9}$$

A $\delta q \otimes \dot{q}_{\hat{b}}^{ned}$ term appears on both sides of the equation and can be cancelled.

$$\delta\dot{q} \otimes q_{\hat{b}}^{ned} = \frac{1}{2}\delta q \otimes q_{\hat{b}}^{ned} \otimes \begin{bmatrix} 0 \\ -\delta\mathbf{b}_{gyro} - \mathbf{n}_\omega \end{bmatrix} \tag{B.10}$$

Right hand multiplication by $(q_{\hat{b}}^{ned})^*$ on both sides results in

$$\delta\dot{q} = \frac{1}{2}\delta q \otimes q_{\hat{b}}^{ned} \otimes \begin{bmatrix} 0 \\ -\delta\mathbf{b}_{gyro} - \mathbf{n}_\omega \end{bmatrix} \otimes (q_{\hat{b}}^{ned})^* \tag{B.11}$$

The last three terms of this equation are of the form of a quaternion rotation. Expressed in the language of rotation matrices, the quaternion rotation portion of the equation can be written as,

$$q_{\hat{b}}^{ned} \otimes \begin{bmatrix} 0 \\ -\delta \mathbf{b}_{gyro} - \mathbf{n}_{\omega} \end{bmatrix} \otimes (q_{\hat{b}}^{ned})^* \implies \begin{bmatrix} 0 \\ -R_{\hat{b}}^{ned}\delta \mathbf{b}_{gyro} - R_{\hat{b}}^{ned}\mathbf{n}_{\omega} \end{bmatrix} \tag{B.12}$$

It follows,

$$\delta \dot{q} = \frac{1}{2}\delta q \otimes \begin{bmatrix} 0 \\ -R_{\hat{b}}^{ned}\delta \mathbf{b}_{gyro} - R_{\hat{b}}^{ned}\mathbf{n}_{\omega} \end{bmatrix} \tag{B.13}$$

Recall $\delta q = \begin{bmatrix} 1 \\ -\frac{1}{2}\delta\theta_b^{ned} \end{bmatrix}$. Substituting this expression back into the equation results in

$$\begin{bmatrix} 1 \\ -\frac{1}{2}\delta\dot{\theta}_b^{ned} \end{bmatrix} = \frac{1}{2}\begin{bmatrix} 1 \\ -\frac{1}{2}\delta\theta_b^{ned} \end{bmatrix} \otimes \begin{bmatrix} 0 \\ -R_{\hat{b}}^{ned}\delta \mathbf{b}_{gyro} - R_{\hat{b}}^{ned}\mathbf{n}_{\omega} \end{bmatrix} \tag{B.14}$$

Recall that quaternion multiplication for two quaternions $\begin{bmatrix} r \\ \mathbf{s} \end{bmatrix}$ and $\begin{bmatrix} q \\ \mathbf{t} \end{bmatrix}$ is equal to $\begin{bmatrix} rq - \mathbf{s}\cdot\mathbf{t} \\ r\mathbf{t} + q\mathbf{s} + \mathbf{s}\times\mathbf{t} \end{bmatrix}$ Using this definition,

$$\begin{aligned} \begin{bmatrix} 1 \\ -\frac{1}{2}\delta\dot{\theta}_b^{ned} \end{bmatrix} &= \frac{1}{2}\begin{bmatrix} 1 \\ -\frac{1}{2}\delta\theta_b^{ned} \end{bmatrix} \otimes \begin{bmatrix} 0 \\ -R_{\hat{b}}^{ned}\delta \mathbf{b}_{gyro} - R_{\hat{b}}^{ned}\mathbf{n}_{\omega} \end{bmatrix} \\ &= \frac{1}{2}\begin{bmatrix} -\frac{1}{2}\delta\theta_b^{ned}\cdot(-R_{\hat{b}}^{ned}\delta \mathbf{b}_{gyro} - R_{\hat{b}}^{ned}\mathbf{n}_{\omega}) \\ -\frac{1}{2}\delta\theta_b^{ned}\times(-R_{\hat{b}}^{ned}\delta \mathbf{b}_{gyro} - R_{\hat{b}}^{ned}\mathbf{n}_{\omega}) - R_{\hat{b}}^{ned}\delta \mathbf{b}_{gyro} - R_{\hat{b}}^{ned}\mathbf{n}_{\omega} \end{bmatrix} \end{aligned} \tag{B.15}$$

Equating the vector portion of the quaternion results in

$$\begin{aligned} -\frac{1}{2}\delta\dot{\theta}_b^{ned} &= \frac{1}{2}(-\frac{1}{2}\delta\theta_b^{ned} \times (-R_{\hat{b}}^{ned}\delta \mathbf{b}_{gyro} - R_{\hat{b}}^{ned}\mathbf{n}_{\omega}) - R_{\hat{b}}^{ned}\delta \mathbf{b}_{gyro} - R_{\hat{b}}^{ned}\mathbf{n}_{\omega}) \\ \delta\dot{\theta}_b^{ned} &= \frac{1}{2}\delta\theta_b^{ned} \times (-R_{\hat{b}}^{ned}\delta \mathbf{b}_{gyro} - R_{\hat{b}}^{ned}\mathbf{n}_{\omega}) + R_{\hat{b}}^{ned}\delta \mathbf{b}_{gyro} + R_{\hat{b}}^{ned}\mathbf{n}_{\omega} \end{aligned} \tag{B.16}$$

Neglecting second order terms results in the expression used in the linear error model in Chapters 3 and 5.

$$\delta\dot{\theta}_b^{ned} = R_{\hat{b}}^{ned}\delta \mathbf{b}_{gyro} + R_{\hat{b}}^{ned}\mathbf{n}_{\omega} \tag{B.17}$$

B.3 Linearization of Measurement Model

To obtain the H matrix, the measurement model is linearized using the Jacobian. Recall that the measurement model $\tilde{\mathbf{z}}$ is defined as

$$\tilde{\mathbf{z}} = \begin{bmatrix} \tilde{\mathbf{z}}_{range} \\ \tilde{\mathbf{z}}_{rate} \\ \tilde{\mathbf{z}}_{alt} \end{bmatrix} = \begin{bmatrix} ||\mathbf{r} - \mathbf{p}^{ned}|| + b_{range} + n_{range} \\ -(\mathbf{v}^{ned})^T \frac{\mathbf{r}-\mathbf{p}^{ned}}{||\mathbf{r}-\mathbf{p}^{ned}||} + b_{rate} + n_{rate} \\ -p_z + b_{alt} + n_{alt} \end{bmatrix} \tag{B.18}$$

The Jacobian of the measurement model evaluated at $\mathbf{x}$ is equal to,

$$H = \left.\frac{\delta \tilde{\mathbf{z}}}{\delta \mathbf{x}}\right|_{x=\hat{x}}$$

$$H = \begin{bmatrix} \frac{\delta \tilde{\mathbf{z}}_{range}}{\delta \mathbf{p}^{ned}} & \frac{\delta \tilde{\mathbf{z}}_{range}}{\delta \mathbf{v}^{ned}} & \frac{\delta \tilde{\mathbf{z}}_{range}}{\delta \theta^{ned}} & \frac{\delta \tilde{\mathbf{z}}_{range}}{\delta \mathbf{b}_{accel}} & \frac{\delta \tilde{\mathbf{z}}_{range}}{\delta \mathbf{b}_{gyro}} & \frac{\delta \tilde{\mathbf{z}}_{range}}{\delta b_{alt}} & \frac{\delta \tilde{\mathbf{z}}_{range}}{\delta b_{range}} & \frac{\delta \tilde{\mathbf{z}}_{range}}{\delta b_{rate}} \\ \frac{\delta \tilde{\mathbf{z}}_{rate}}{\delta \mathbf{p}^{ned}} & \frac{\delta \tilde{\mathbf{z}}_{rate}}{\delta \mathbf{v}^{ned}} & \frac{\delta \tilde{\mathbf{z}}_{rate}}{\delta \theta^{ned}} & \frac{\delta \tilde{\mathbf{z}}_{rate}}{\delta \mathbf{b}_{accel}} & \frac{\delta \tilde{\mathbf{z}}_{rate}}{\delta \mathbf{b}_{gyro}} & \frac{\delta \tilde{\mathbf{z}}_{rate}}{\delta b_{alt}} & \frac{\delta \tilde{\mathbf{z}}_{rate}}{\delta b_{range}} & \frac{\delta \tilde{\mathbf{z}}_{rate}}{\delta b_{rate}} \\ \frac{\delta \tilde{\mathbf{z}}_{alt}}{\delta \mathbf{p}^{ned}} & \frac{\delta \tilde{\mathbf{z}}_{alt}}{\delta \mathbf{v}^{ned}} & \frac{\delta \tilde{\mathbf{z}}_{alt}}{\delta \theta^{ned}} & \frac{\delta \tilde{\mathbf{z}}_{alt}}{\delta \mathbf{b}_{accel}} & \frac{\delta \tilde{\mathbf{z}}_{alt}}{\delta \mathbf{b}_{gyro}} & \frac{\delta \tilde{\mathbf{z}}_{alt}}{\delta b_{alt}} & \frac{\delta \tilde{\mathbf{z}}_{alt}}{\delta b_{range}} & \frac{\delta \tilde{\mathbf{z}}_{alt}}{\delta b_{rate}} \end{bmatrix}\Bigg|_{x=\hat{x}} \tag{B.19}$$

Notice that many of the partial derivatives will equal 0, as the measurements do not contain several of the terms in $\delta\mathbf{x}$. The list of nonzero partial derivatives is

$$\frac{\delta \tilde{\mathbf{z}}_{range}}{\delta \mathbf{p}^{ned}}, \frac{\delta \tilde{\mathbf{z}}_{rate}}{\delta \mathbf{p}^{ned}}, \frac{\delta \tilde{\mathbf{z}}_{rate}}{\delta \mathbf{v}^{ned}}, \frac{\delta \tilde{\mathbf{z}}_{alt}}{\delta \mathbf{p}^{ned}}, \frac{\delta \tilde{\mathbf{z}}_{range}}{\delta b_{range}}, \frac{\delta \tilde{\mathbf{z}}_{rate}}{\delta b_{rate}}, \text{ and } \frac{\delta \tilde{\mathbf{z}}_{alt}}{\delta b_{alt}}$$

Using the regular rules for derivatives (i.e. chain rule, quotient rule, etc) the nonzero partial derivatives are calculated in order.

The partial derivative of the range with respect to position:

$$\begin{aligned} \frac{\delta \tilde{\mathbf{z}}_{range}}{\delta \mathbf{p}^{ned}} &= \frac{\delta}{\delta \mathbf{p}^{ned}}(||\mathbf{r} - \mathbf{p}^{ned}|| + b_{range} + n_{range}) \\ &= \frac{\delta}{\delta \mathbf{p}^{ned}}(\sqrt{(\mathbf{r} - \mathbf{p}^{ned})^T(\mathbf{r} - \mathbf{p}^{ned})} + b_{range} + n_{range}) \\ &= \left(\frac{1/2}{\sqrt{(\mathbf{r} - \mathbf{p}^{ned})^T(\mathbf{r} - \mathbf{p}^{ned})}}\right)(-2(\mathbf{r} - \mathbf{p}^{ned})^T) \\ &= \frac{-(\mathbf{r} - \mathbf{p}^{ned})^T}{||\mathbf{r} - \mathbf{p}^{ned}||} \end{aligned} \tag{B.20}$$

The partial derivative of the range rate with respect to position:

$$\begin{aligned}
\frac{\delta \tilde{\mathbf{z}}_{rate}}{\delta \mathbf{p}^{ned}} &= \frac{\delta}{\delta \mathbf{p}^{ned}}(-(\mathbf{v}^{ned})^T \frac{\mathbf{r}-\mathbf{p}^{ned}}{||\mathbf{r}-\mathbf{p}^{ned}||} + b_{rate} + n_{rate}) \\
&= \frac{\delta}{\delta \mathbf{p}^{ned}}(-(\mathbf{v}^{ned})^T \frac{\mathbf{r}-\mathbf{p}^{ned}}{\sqrt{(\mathbf{r}-\mathbf{p}^{ned})^T(\mathbf{r}-\mathbf{p}^{ned})}}) \\
&= \frac{\sqrt{(\mathbf{r}-\mathbf{p}^{ned})^T(\mathbf{r}-\mathbf{p}^{ned})}(\mathbf{v}^{ned})^T}{(\mathbf{r}-\mathbf{p}^{ned})^T(\mathbf{r}-\mathbf{p}^{ned})} \\
&\quad - \frac{(-\mathbf{v}^{ned})^T(\mathbf{r}-\mathbf{p}^{ned})\left(\frac{1/2}{\sqrt{(\mathbf{r}-\mathbf{p}^{ned})^T(\mathbf{r}-\mathbf{p}^{ned})}}\right)(-2(\mathbf{r}-\mathbf{p}^{ned})^T)}{(\mathbf{r}-\mathbf{p}^{ned})^T(\mathbf{r}-\mathbf{p}^{ned})} \\
&= \frac{||\mathbf{r}-\mathbf{p}^{ned}||(\mathbf{v}^{ned})^T - (\mathbf{v}^{ned})^T(\mathbf{r}-\mathbf{p}^{ned})\left(\frac{(\mathbf{r}-\mathbf{p}^{ned})^T}{||\mathbf{r}-\mathbf{p}^{ned}||}\right)}{||\mathbf{r}-\mathbf{p}^{ned}||^2} \\
&= \frac{(\mathbf{v}^{ned})^T}{||(\mathbf{r}-\mathbf{p}^{ned})||} - \frac{(\mathbf{v}^{ned})^T(\mathbf{r}-\mathbf{p}^{ned})(\mathbf{r}-\mathbf{p}^{ned})^T}{||(\mathbf{r}-\mathbf{p}^{ned})||^3}
\end{aligned} \tag{B.21}$$

The partial derivative of the range rate with respect to velocity:

$$\begin{aligned}
\frac{\delta \tilde{\mathbf{z}}_{rate}}{\delta \mathbf{v}^{ned}} &= \frac{\delta}{\delta \mathbf{v}^{ned}}(-(\mathbf{v}^{ned})^T \frac{\mathbf{r}-\mathbf{p}^{ned}}{||\mathbf{r}-\mathbf{p}^{ned}||} + b_{rate} + n_{rate}) \\
&= \frac{\delta}{\delta \mathbf{v}^{ned}}(-(\mathbf{v}^{ned})^T \frac{\mathbf{r}-\mathbf{p}^{ned}}{||\mathbf{r}-\mathbf{p}^{ned}||}) \\
&= \frac{-(\mathbf{r}-\mathbf{p}^{ned})^T}{||\mathbf{r}-\mathbf{p}^{ned}||}
\end{aligned} \tag{B.22}$$

The partial derivative of the altitude with respect to the position:

$$\begin{aligned}
\frac{\delta \tilde{\mathbf{z}}_{alt}}{\delta \mathbf{p}^{ned}} &= \frac{\delta}{\delta \mathbf{p}^{ned}}(-p_z + b_{alt} + n_{alt}) \\
&= \frac{\delta}{\delta \mathbf{p}^{ned}}(-p_z) \\
&= [0, 0, -1]
\end{aligned} \tag{B.23}$$

The partial derivative of the range with respect to the radar range bias:

$$\begin{aligned}\frac{\delta\tilde{\mathbf{z}}_{range}}{\delta b_{range}} &= \frac{\delta}{\delta b_{range}}(||\mathbf{r}-\mathbf{p}^{ned}|| + b_{range} + n_{range}) \\ &= \frac{\delta}{\delta b_{range}}(b_{range}) \\ &= 1\end{aligned} \tag{B.24}$$

The partial derivative of the range rate with respect to the range-rate bias:

$$\begin{aligned}\frac{\delta\tilde{\mathbf{z}}_{rate}}{\delta b_{rate}} &= \frac{\delta}{\delta b_{rate}}(-(\mathbf{v}^{ned})^T\frac{\mathbf{r}-\mathbf{p}^{ned}}{||\mathbf{r}-\mathbf{p}^{ned}||} + b_{rate} + n_{rate}) \\ &= \frac{\delta}{\delta b_{rate}}(b_{rate}) \\ &= 1\end{aligned} \tag{B.25}$$

The partial derivative of the altitude with respect to the altimeter bias:

$$\begin{aligned}\frac{\delta\tilde{\mathbf{z}}_{alt}}{\delta b_{alt}} &= \frac{\delta}{\delta b_{alt}}(-p_z + b_{alt} + n_{alt}) \\ &= \frac{\delta}{\delta b_{alt}}(b_{alt}) \\ &= 1\end{aligned} \tag{B.26}$$

Populating the Jacobian with the above partial derivatives and evaluating at $\mathbf{x} = \hat{\mathbf{x}}$ yields

$$H = \begin{bmatrix} \frac{-(\mathbf{r}-\hat{\mathbf{p}}^{ned})^T}{||\mathbf{r}-\hat{\mathbf{p}}^{ned}||} & 0_{1x3} & 0_{1x3} & 0_{1x3} & 0 & 1 & 0 \\ \frac{(\hat{\mathbf{v}}^{ned})^T}{||(\mathbf{r}-\hat{\mathbf{p}}^{ned})||} - \frac{(\hat{\mathbf{v}}^{ned})^T(\mathbf{r}-\hat{\mathbf{p}}^{ned})(\mathbf{r}-\hat{\mathbf{p}}^{ned})^T}{||(\mathbf{r}-\hat{\mathbf{p}}^{ned})||^3} & \frac{-(\mathbf{r}-\hat{\mathbf{p}}^{ned})^T}{||(\mathbf{r}-\hat{\mathbf{p}}^{ned})||} & 0_{1x3} & 0_{1x3} & 0 & 0 & 1 \\ [0,0,-1] & 0_{1x3} & 0_{1x3} & 0_{1x3} & 1 & 0 & 0 \end{bmatrix} \tag{B.27}$$

Let $\mathbf{d} = \mathbf{r} - \mathbf{p}^{ned}$ to obtain the H matrix from Chapters 3 and 5.

$$H = \begin{bmatrix} \frac{-\mathbf{d}^T}{||\mathbf{d}||} & 0_{1x3} & 0_{1x3} & 0_{1x3} & 0_{1x3} & 0 & 1 & 0 \\ \frac{(\hat{\mathbf{v}}^{ned})^T}{||\mathbf{d}||} - \frac{(\hat{\mathbf{v}}^{ned})^T \mathbf{d}\mathbf{d}^T}{||\mathbf{d}||^3} & \frac{-\mathbf{d}^T}{||\mathbf{d}||} & 0_{1x3} & 0_{1x3} & 0_{1x3} & 0 & 0 & 1 \\ [0, 0, -1] & 0_{1x3} & 0_{1x3} & 0_{1x3} & 0_{1x3} & 1 & 0 & 0 \end{bmatrix} \tag{B.28}$$

APPENDIX C

Pulse Compression Derivation

This appendix derives the expression used for a pulse compressed signal after matched filtering. A commonly used signal for pulse compression in radar is a linear frequency modulated (LFM) pulse, or a chirp pulse. This pulse signal is sinusoid like with a phase component that is quadratic in time. The LFM pulse is denoted $s(t)$ and is of the form

$$s(t) = \begin{cases} \exp(j2\pi f_0 t + j\alpha t^2), & 0 \leq t \leq T \\ 0, & \text{otherwise} \end{cases} \tag{C.1}$$

where f_0 is the initial frequency, α is related to the linear FM rate, [1] and T is the pulse duration. Figure C.1 shows the real and imaginary parts of a chirp signal generated in MATLAB. Notice in Figure C.2 that the phase of the signal is quadratic, and the instantaneous frequency of the signal is linear with slope α/π.

To compress the linear FM pulse, a matched filter is used, which is a time reversed, conjugate version of $s(t)$. The matched filter result is denoted $p(t)$ and is defined as the convolution of $s(t)$ with the matched filter $s^*(T-t)$.

$$\begin{aligned} p(t) &= s(t) * s^*(T-t) \\ &= \begin{cases} \int_0^t s(\lambda)s^*(T-(t-\lambda))d\lambda, & 0 \leq t \leq T \\ \int_{t-T}^T s(\lambda)s^*(T-(t-\lambda))d\lambda, & T \leq t \leq 2T \end{cases} \end{aligned} \tag{C.2}$$

The convolution is split into two integrals. The first of the two integrals is solved as

[1] In other places in this thesis, K is used to denote the FM rate. The conversion between K and α is $\alpha = \pi K$

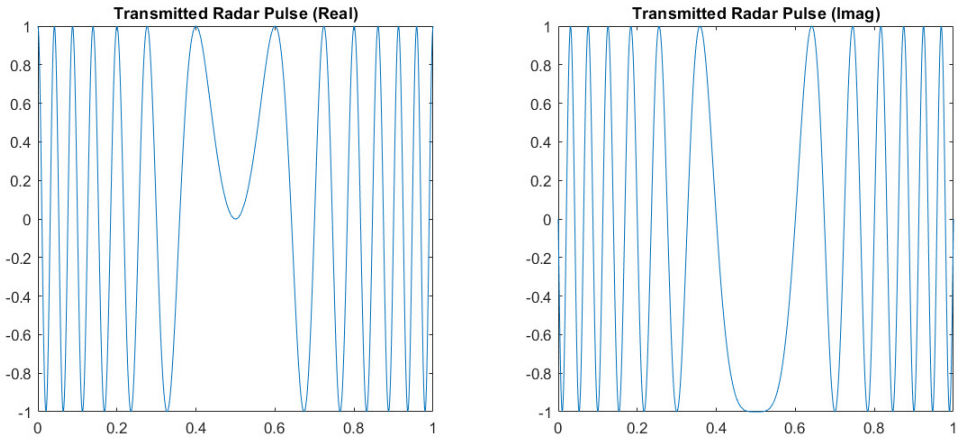

Fig. C.1: Real (left) and imaginary (right) transmission of pulse $s(t)$.

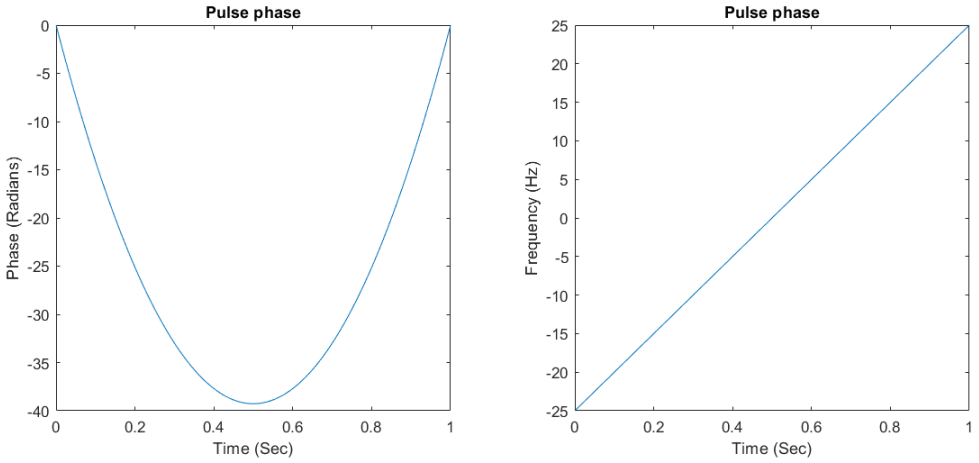

Fig. C.2: Phase (left) and instantaneous frequency (right) of $s(t)$.

$$\begin{aligned}\int_0^t s(\lambda)s^*(T-(t-\lambda))d\lambda &= \int_0^t s(\lambda)s^*(\lambda+T-t)d\lambda \\ &= \int_0^t e^{j(2\pi f_0 t+\alpha t^2)}e^{-j(2\pi f_0(\lambda+T-t)+\alpha(\lambda+T-t)^2)}d\lambda \\ &= \int_0^t e^{-j(2\pi f_0(T-t)+\alpha(T-t)^2+2\alpha\lambda(T-t))}d\lambda \\ &= e^{-j(2\pi f_0(T-t)+\alpha(T-t)^2)}\int_0^t e^{-j2\alpha\lambda(T-t)}d\lambda \end{aligned} \tag{C.3}$$

Ignoring the constant exponential out front, and by letting $\rho = T - t$,

$$\begin{aligned}\int_0^t e^{-j2\alpha\lambda\rho}d\lambda &= \left.\frac{e^{-j2\alpha\lambda\rho}}{-j2\alpha\rho}\right|_0^t \\ &= \frac{1}{-j2\alpha\rho}\left[e^{-j2\alpha t\rho}-1\right] \\ &= \frac{e^{-j\alpha t\rho}}{-j2\alpha\rho}\left[e^{-j\alpha t\rho}-e^{j\alpha t\rho}\right] \end{aligned} \tag{C.4}$$

Recall the identity $\sin\theta = \frac{e^{j\theta}-e^{-j\theta}}{2j}$. Using this identity,

$$\frac{e^{-j\alpha t\rho}}{-j2\alpha\rho}\left[e^{-j\alpha t\rho}-e^{j\alpha t\rho}\right] = e^{-j\alpha t\rho}\frac{\sin(\alpha t\rho)}{\alpha\rho} \tag{C.5}$$

Returning the constant out front, the expression for the first integral for matched filtering is,

$$p(t) = \quad e^{-j(2\pi f_0\rho+\alpha\rho^2+\alpha t\rho)}\frac{\sin(\alpha t\rho)}{\alpha\rho} \;\; 0 \le t < T \tag{C.6}$$

The second integral in the convolution is identical to the first up to the point of evaluating the integrated function at the limits of integration. Once again, the constant out front is ignored until the end of the derivation.

$$\begin{aligned}\int_{t-T}^{T} e^{-j2\alpha\lambda\rho} d\lambda &= \frac{e^{-j2\alpha\lambda\rho}}{-j2\alpha\rho}\Big|_{t-T}^{T} \\ &= \frac{1}{-j2\alpha\rho}\left[e^{-j2\alpha t\rho} - e^{-j2\alpha t\rho} e^{j2\alpha T\rho}\right] \\ &= \frac{e^{-j\alpha t\rho}}{-j2\alpha\rho}\left[e^{-j(\alpha t\rho - 2\alpha T\rho)} - e^{j(\alpha t\rho - 2\alpha T\rho)}\right] \\ &= e^{-j\alpha t\rho}\frac{\sin(\alpha\rho(2T-t))}{\alpha\rho}\end{aligned} \tag{C.7}$$

Replacing the constant out front, the expression for the second stage of the convolution is,

$$p(t) = \quad e^{-j(2\pi f_0\rho + \alpha\rho^2 + \alpha t\rho)}\frac{\sin(\alpha\rho(2T-t))}{\alpha\rho} \quad T < t < 2T \tag{C.8}$$

Taking a limit at $t = T$, $p(t)$ can be written as the following piecewise function.

$$p(t) = e^{-j(2\pi f_0\rho + \alpha\rho^2 + \alpha t\rho)}\begin{cases} \frac{\sin(\alpha\rho t)}{\alpha\rho}, & 0 \le t < T \\ T, & t = T \\ \frac{\sin(\alpha\rho(2T-t))}{\alpha\rho}, & T < t \le 2T \end{cases} \tag{C.9}$$

This expression can be written in a closed form using the triangle function $\text{tri}(x) = \text{rect}(x/2)(1 - |x|)$ and the sinc function $\text{sinc}(x) = \sin(\pi x)/\pi x$.

$$p(t) = e^{-j(2\pi f_0\rho + \alpha\rho^2 + \alpha t\rho)}(T - |t - T|)\text{sinc}(\frac{\alpha\rho}{\pi}(T - |t - T|)) \tag{C.10}$$

Figure C.3 shows the matched return signal $p(t)$. As a side note, matched filtering produces good results in the presence of noise. Figure C.4 shows the result of pulse compression on a signal with an SNR or -15dB.

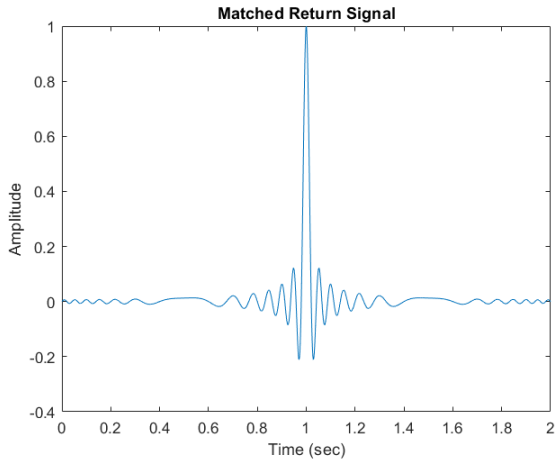

Fig. C.3: Matched return signal $p(t)$.

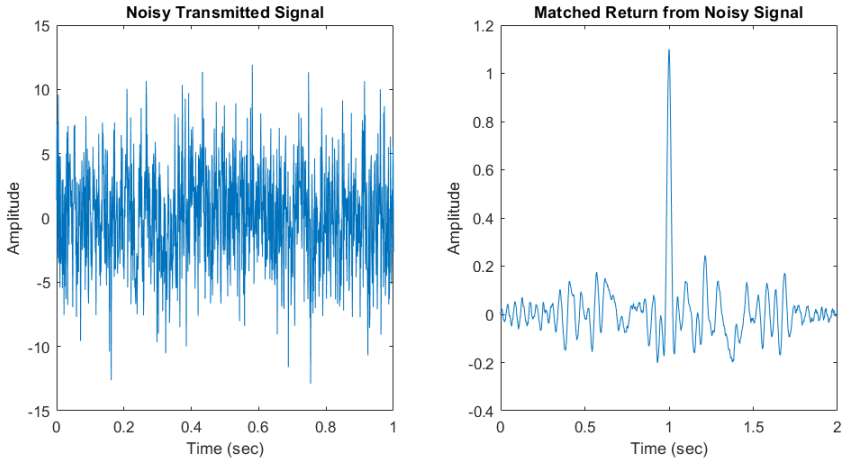

Fig. C.4: Transmitted pulse with SNR of -15dB and the matched return signal

APPENDIX D

Autofocus

This appendix is meant to give details on autofocusing algorithms explored through the course of this thesis. The material here is very loosely based on material from [3].

D.1 Range and Range Rate Measurements

In Chapter 3, it was shown that GPS denied navigation was feasible when provided with range and range rate measurements from a radar system. Later in Chapter 5, it was stated that these measurements could not be accurately extracted from SAR images. As a result, range and range rate measurements were replaced with range and cross range measurements. This section documents the reasoning behind that choice.

The method explored to extract range and range rate measurements from SAR images hinges on the hyperbolic range equation and its involvement in the backprojection summation. The hyperbolic range equation is defined as,

$$R(\eta) = \sqrt{R_0^2 + V_r^2 \eta^2} \tag{D.1}$$

where R_0 is the range of closest approach between the ground target and the radar platform, V_r is the forward velocity of the radar platform (r subscript refers to rectilinear coordinate frame), and η is azimuth time. The target on the ground is used as a reference point from which measurements are taken. The location of the target is assumed to be known. Furthermore, the backprojection equation is defined as,

$$A(\mathbf{x}_{pix}) = \sum_n s_{out}(t_{pix,n}) \exp\{j4\pi \frac{R(\eta)}{\lambda}\} \tag{D.2}$$

where $\mathbf{x_{pix}}$ is the location of an image pixel on the ground, n is used to denote the n^{th} range compressed signal, λ is the center frequency of the radar's chirp signal, and $s_{out}(t_{pix,n})$ is a

sample of range compressed data at time $t_{pix,n}$.

Note that the hyperbolic range equation is expressed as $R(\eta)$. The range equation as defined is not explicitly a function of $\mathbf{x_{pix}}$ but does depend implicitly on the pixel location. Both the time of closest approach, η_0, and range of closest approach, R_0, will change when $\mathbf{x_{pix}}$ changes.

Measuring the range and range rate is a matter of accurately estimating the range of closest approach, the time of closest approach, and the forward velocity from the SAR data. After obtaining estimates for each of those parameters, the range is found using the hyperbolic range equation. The range rate is found using the derivative of the hyperbolic range equation, which is equal to

$$\begin{aligned}\frac{dR(\eta)}{d(\eta)} &= \frac{d(\sqrt{R_0^2 + V_r^2\eta^2})}{d(\eta)} \\ &= 2V_r^2\eta\frac{1}{2\sqrt{R_0^2 + V_r^2\eta^2}} \\ &= \frac{V_r^2\eta}{R(\eta)}\end{aligned} \tag{D.3}$$

By convention, η is centered around the time of closest approach η_0. If η_0 is known, extrapolating to other times is simple. Assuming the SAR image is time-stamped and that the location of the radar ground target is known, R_0 and η_0 is simple to find by comparing the true target location to the target location on the SAR image.

This can be done using a cross correlation between a reference image and the resulting image. The peak of the cross correlation shows how much the target has shifted from the reference, which can be translated into range of closest approach and time of closest approach via the range resolution and pulse repetition frequency.

Estimating the range and time of closest approach using the cross correlation was found to be very accurate. However, estimations of the forward velocity, V_r, proved to be inaccurate. The method to estimate forward velocity from the SAR image depends on the phase component of the backprojection equation. This phase component represents the matched filter portion of azimuth compression. If there are errors in the matched filter

phase, blurring will occur in the final image. Recall the phase as

$$\exp\{j4\pi\frac{R(\eta)}{\lambda}\} = \exp\{j4\pi\frac{\sqrt{R_0^2+V_r^2\eta^2}}{\lambda}\} \tag{D.4}$$

Assuming zero squint, a Taylor series approximation of the range equation centered around the time of closest approach is performed. This approximation is given by

$$R(\eta) = \sqrt{R_0^2+V_r^2\eta^2} \approx \hat{R}(\eta) = R_0 + \frac{1}{2}\frac{V_r^2\eta^2}{R_0} \tag{D.5}$$

This approximation is accurate for short synthetic apertures and is used frequently in literature.

Combining the Taylor series approximation with the backprojection phase results in the following.

$$\exp\{j4\pi\frac{\sqrt{R_0^2+V_r^2\eta^2}}{\lambda}\} \approx \exp\{j4\pi\frac{R_0+\frac{1}{2}\frac{V_r^2\eta^2}{R_0}}{\lambda}\} \tag{D.6}$$

Using the Taylor series approximation, an error is introduced into V_r, which is denoted $\hat{V_r}$. This error is assumed to be additive as $\hat{V_r} = V_r + e_{V_r}$

The backprojection phase with errors is then written as

$$\begin{aligned}
\exp\{j4\pi\frac{R_0+\frac{1}{2}\frac{\hat{V_r}^2\eta^2}{R_0}}{\lambda}\} &= \exp\{j4\pi\frac{R_0+\frac{1}{2}\frac{(V_r+e_{V_r})^2\eta^2}{R_0}}{\lambda}\} \\
&= \exp\{j4\pi\frac{R_0+\frac{1}{2}\frac{(V_r^2+2V_re_{V_r}+e_{V_r}^2)\eta^2}{R_0}}{\lambda}\} \\
&= \exp\{j4\pi\frac{R_0+\frac{1}{2}\frac{(V_r^2\eta^2)}{R_0}+\frac{1}{2}\frac{(2V_re_{V_r}+e_{V_r}^2)\eta^2}{R_0}}{\lambda}\} \\
&= \exp\{j4\pi(\frac{\hat{R}(\eta)}{\lambda}+\frac{(2V_re_{V_r}+e_{V_r}^2)\eta^2}{2R_0\lambda})\}
\end{aligned} \tag{D.7}$$

Therefore, introducing a forward velocity error will create a phase error equal to

$$\frac{(2V_re_{V_r}+e_{V_r}^2)\eta^2}{2R_0\lambda} \tag{D.8}$$

By solving for the phase error, the forward velocity can be estimated. Autofocusing

techniques are used to correct for the phase errors. If autofocusing is successful, the phase of the matched filter could be adjusted to equal

$$\exp\{j4\pi(\frac{R(\eta)}{\lambda} + (\frac{(2V_r e_{V_r} + e_{V_r}^2)}{2R_0\lambda} + c_{auto})\eta^2)\} \tag{D.9}$$

where c_{auto} is a correction factor resulting from the autofocusing. Assuming an accurate autofocus result, $\frac{(2V_r e_{V_r} + e_{V_r}^2)}{2R_0\lambda} + c_{auto} = 0$ is true and V_R can be solved for.

To simplify the expression, the $e_{V_r}^2$ term is typically small enough to ignore. As such, an expression for a forward velocity estimate is

$$V_r = -\frac{c_{auto} R_0 \lambda}{e_{V_r}} \tag{D.10}$$

The above equation depends on e_{V_r}, which is problematic since the velocity error cannot be exactly known. However, the greater problem of this expression is c_{auto}, which in simulation was never accurate enough to properly estimate V_r even when velocity errors were perfectly known. In most cases, the Kalman filter produces a better estimate of V_r; however, using the Kalman filter's velocity estimate did not produce accurate range rate measurements and led to diverging estimation errors. As a result of these discoveries, the structure of the measurement model was changed to incorporated range and cross range measurements.

D.2 Autofocus

This section provides information on two of the autofocusing methods explored for this thesis. These methods are contrast maximization and azimuth misregistration. Other methods not explored here include phase difference (PD) and phase gradient algorithm (PGA).

Contrast maximization and azimuth misregistration were both implemented in order to compare estimation accuracy of forward velocity. However, as mentioned above, neither algorithm was able to produce accurate estimates of the forward velocity. In comparison

to each other, azimuth misregistration was more accurate than contrast maximization; however, in both cases, the velocity estimate was worse than the estimate provided by the EKF.

Contrast Maximization

Contrast maximization essentially adjusts the phase in the azimuth matched filter until the contrast in the image has been maximized. This is an iterative process, but the iteration number may be cut down through the aid of quadratic approximation. Essentially, measures of contrast are approximately quadratic around the correct answer.

There are several different measures for the contrast of an image. Three have been tested on simulation data. Two of the three metrics seem to yield accurate results.

The first measure is the average pixel intensity to power ratio. It is calculated as

$$C = \frac{E[|I|^2]}{E[|I|]^2} \tag{D.11}$$

where $E[\cdot]$ is the expectation operator and $|I|$ is the pixel magnitude. This metric appeared to yield correct results. This measure was proposed in [3].

The second measure is the standard deviation to average magnitude ratio. It is calculated as

$$C = \frac{\sqrt{E[|I|^2] - E[|I|]^2}}{E[|I|]} \tag{D.12}$$

This metric also appears to give good results. This measure was proposed in [57].

The third measure is the standard deviation to average pixel intensity. It is calculated as

$$C = \frac{\sqrt{E[|I|^2] - E[|I|]^2}}{E[|I|^2]} \tag{D.13}$$

This metric did not seem to give correct results. When the image was correctly focused, this metric yielded a result that was lower than when the image was incorrectly focused. This measure was also proposed in [57].

To solve for the optimal c_{auto} value, a diminishing step size gradient descent optimization structure was implemented. This required the gradient of the Contrast with respect to c_{auto}. This expression is complicated enough that no analytical solution was solved for. Instead, a numerical derivative was used.

Figures D.1 and D.2 are provided as a demonstration of the autofocusing algorithm's effectiveness. In Figure D.1, the left most image is a reference image showing the target formed with the true trajectory. The middle image is the result of forming an image with an along track velocity error. The right most image is result of the autofocusing algorithm that takes the blurred image as input.

Contrast maximization is an iterative algorithm, so Figure D.2 has been provided to show how the values for contrast and c_{auto} change with respect to the iterations of the optimization routine. The left most plot shows the contrast using the intensity over power ratio. The right most image shows the convergence of c_{auto}.

Azimuth Misregistration

Azimuth misregistration is based on multilook processing. The idea is that an error in the azimuth FM rate will cause a ground target to shift in the azimuth direction between two separate looks of the same target.

In this section the azimuth matched filter is expressed in terms of R_0 and V_r.

$$\exp\{j4\pi\frac{R_0+\frac{1}{2}\frac{V_r^2\eta^2}{R_0}}{\lambda}\} \tag{D.14}$$

By neglecting the constant phase term and defining the azimuth FM rate as $K_a=\frac{2V_r^2}{R_0\lambda}$, the azimuth matched filter can be expressed as

$$\exp\{j\pi K_a\eta^2\} \tag{D.15}$$

Let K_{amf} be the azimuth FM rate with an error included such that $K_{amf}=K_a+\Delta K$ where ΔK is the amount of error present in K_{amf}.

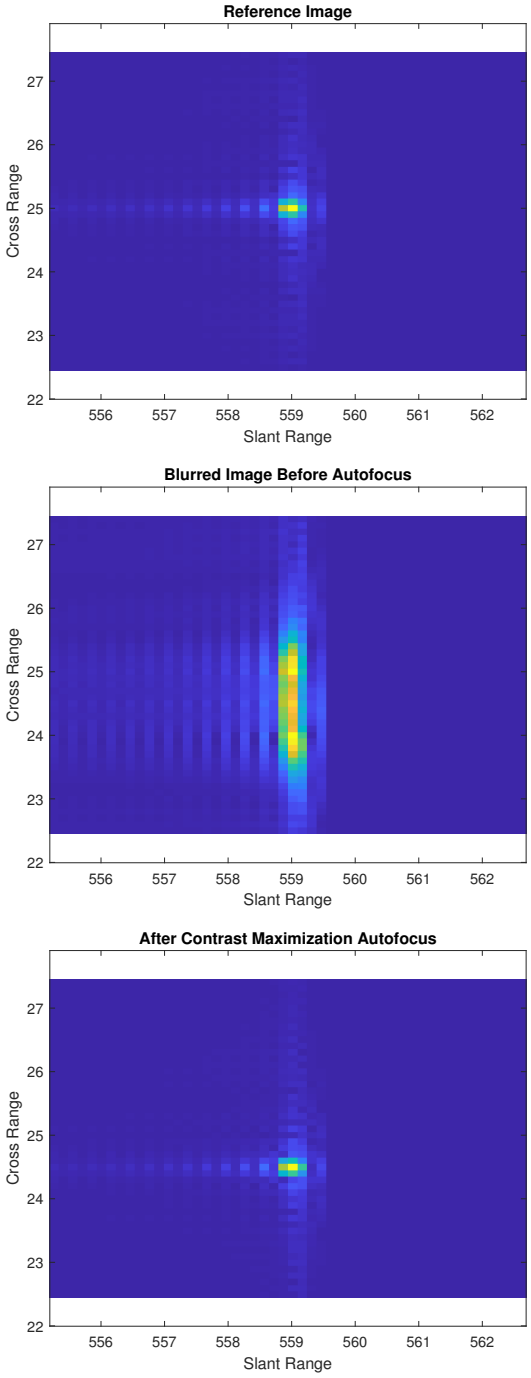

Fig. D.1: Demonstration of contrast maximization. Top, reference image. Center, image before autofocusing. Bottom, image after contrast maximization.

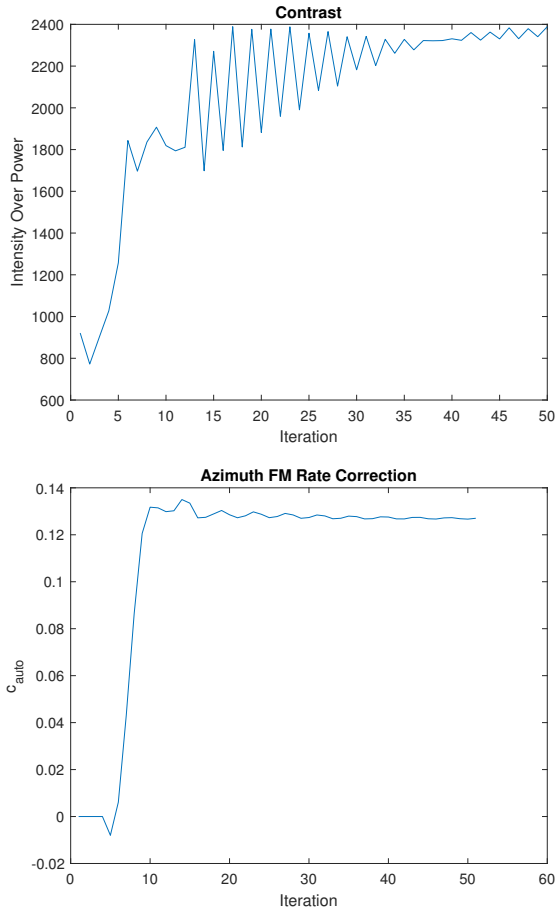

Fig. D.2: Convergence of contrast (top) and c_{auto} (bottom) throughout contrast maximization.

The amount of misregistration between the two separate looks is denoted $\Delta\eta$ and is defined as

$$\Delta\eta = -\Delta f_a \left(\frac{1}{K_a} - \frac{1}{K_{amf}} \right) \tag{D.16}$$

For each of the looks, a different frequency band is used in the matched filter. In general, the frequency used in the matched filter is equal to $f_\eta = -K_a\eta$ where η is centered around the time of closest approach. Each of the two looks will have a different center frequency, denoted $f_{\eta,1}$ and $f_{\eta,2}$. Δf_a is defined as the difference between the center frequencies of the two looks, $\Delta f_a = f_{\eta,2} - f_{\eta,1}$

By rearranging equation (D.16), the azimuth FM rate error can be expressed as

$$\Delta K_a \approx -\frac{K_{amf}^2}{\Delta f_a}\Delta\eta \tag{D.17}$$

$\Delta\eta$ can be solved for numerically by cross correlating Look 1 and Look 2 with each other. the peak of the cross correlation shifts according to the level of misregistration. Interpolating in azimuth may yield a better misregistration result.

With ΔK solved for, the corrected azimuth matched filter is equal to

$$\exp\{j\pi(K_{amf} - \Delta K)\eta^2\} \tag{D.18}$$

At this point, the ΔK term is converted into a c_{auto} type term for estimation of forward velocity.

Figures D.3 and D.4 are provided to demonstrate autofocusing using azimuth misregistration. Figure D.3 shows two different looks of the same target. This demonstrates how the target will shift in azimuth between two looks. The left and center images are the two looks. The right most image is the cross correlation of the two looks. This shows how the shift can be tracked using the peak of the cross correlation.

Figure D.4 demonstrates azimuth misregistration. The left most image is a reference image of the target formed using the true trajectory. The center image an image formed

with an along track velocity error. The right most image is the result of autofocusing using azimuth misregistration.

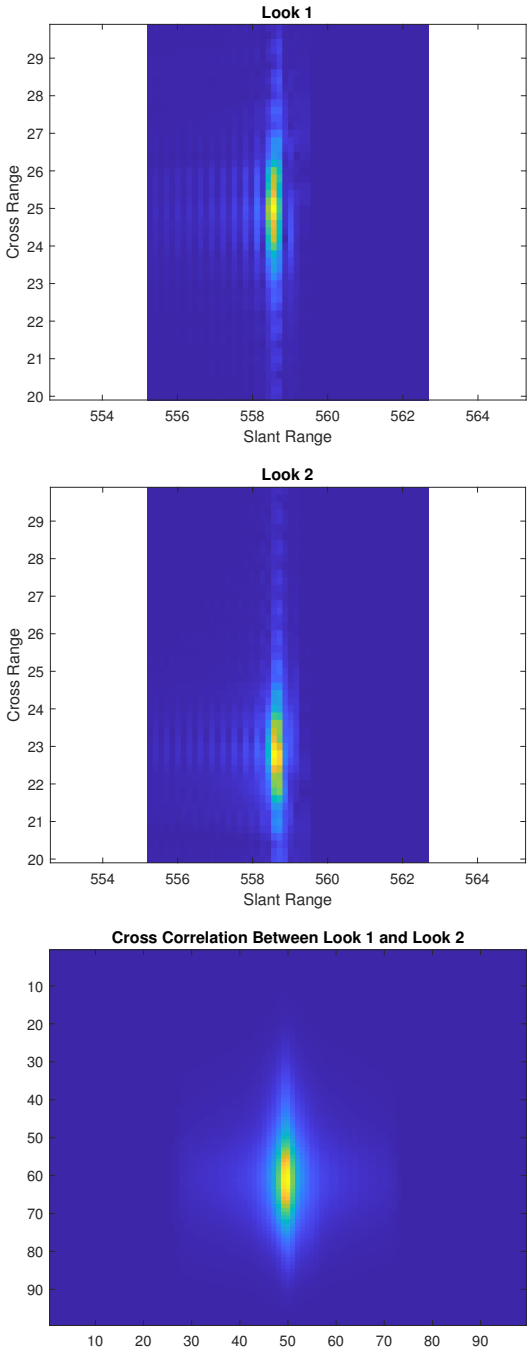

Fig. D.3: Demonstration of misregistration between different looks. Top, look 1. Center, look 2. Bottom, cross correlation between the two looks.

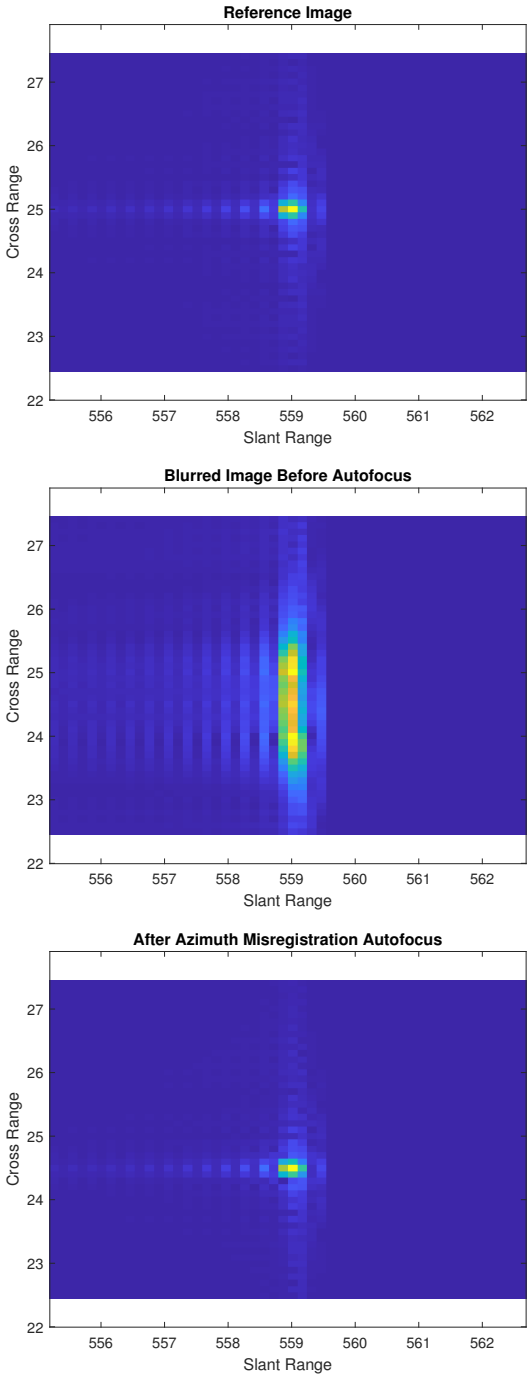

Fig. D.4: Demonstration of autofocusing using azimuth misregistration. Top, reference image. Center, image before autofocusing. Bottom, image after azimuth misregistration autofocusing.

APPENDIX E

Spatial Variance and Ambiguities

This appendix is meant to provide discussion on aspects of SAR that require additional consideration.

Creating images using SAR is not a spatially invariant problem, which poses unique problems for future study. In this thesis, only single point targets have been considered in analysis. While easier to conceptualize, the single target scenario does not account for some behaviors. Errors in image formation or navigation state do not affect each target the same. For example, if the SAR platform has an error in elevation position, closer targets will be affected more dramatically than further targets. This is illustrated by Figure E.1. In this Figure, the solid lines represent the slant range to the targets before error. The dotted lines represent the slant range after an elevation error is introduced. The bold line superimposed on the dotted line shows the difference in slant range between the error free case and the error present case. Notice that the bold line is longer for the closer of the two targets.

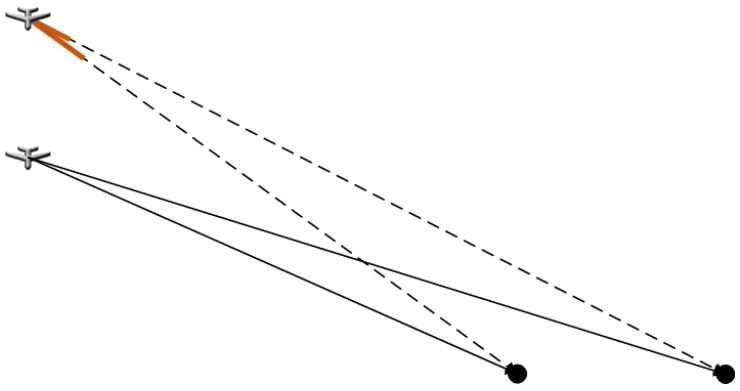

Fig. E.1: Illustration of how an elevation error on the slant range affect two distinct targets differently.

Another example of how errors affect multiple targets differently can be seen in Figure E.2. This figure depicts a velocity error, which appears as a linearly increasing deviation

from the true path. In the figure, two targets are show that originally have equal ranges of closest approach. After a velocity error, the ranges of closest approach change such that the lengths are no longer equal. Each new range of closest approach depends on the time at which the error was introduced and the target's position relative to the radar vehicle's position.

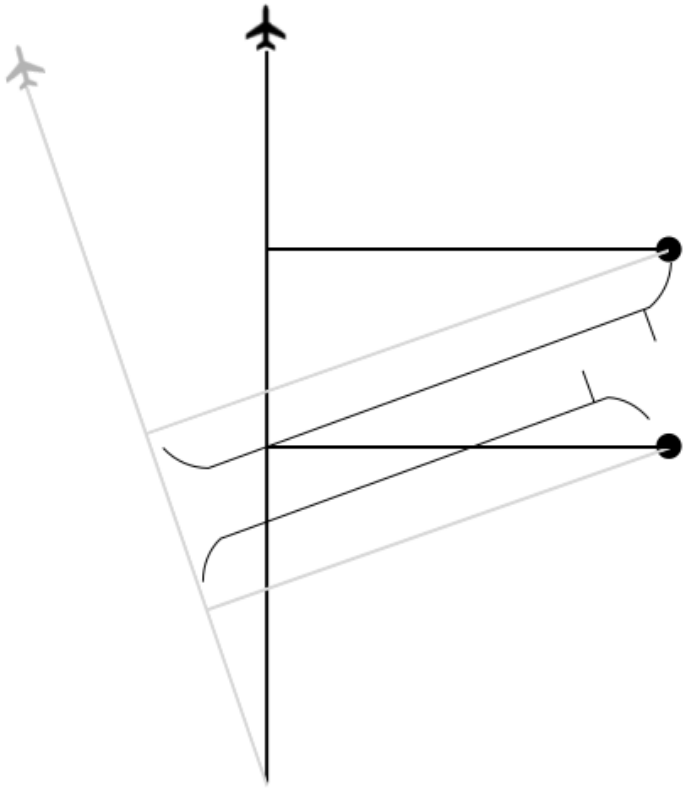

Fig. E.2: Illustration of how a velocity error can affect the range of closest approach for multiple targets. Solid black lines indicate truth. Lighter gray lines indicate errors.

Another consideration to be aware of during SAR imaging is the presence of ambiguity. Ambiguity was discussed in Chapter 3 where it was explained how different combinations of range and elevation values can lead to equal range values. This is once again illustrated in Figure E.3. This type of ambiguity can make it difficult to infer navigation errors from a target's location within an image.

This ambiguity also exists in the reverse direction. For a given radar platform position,

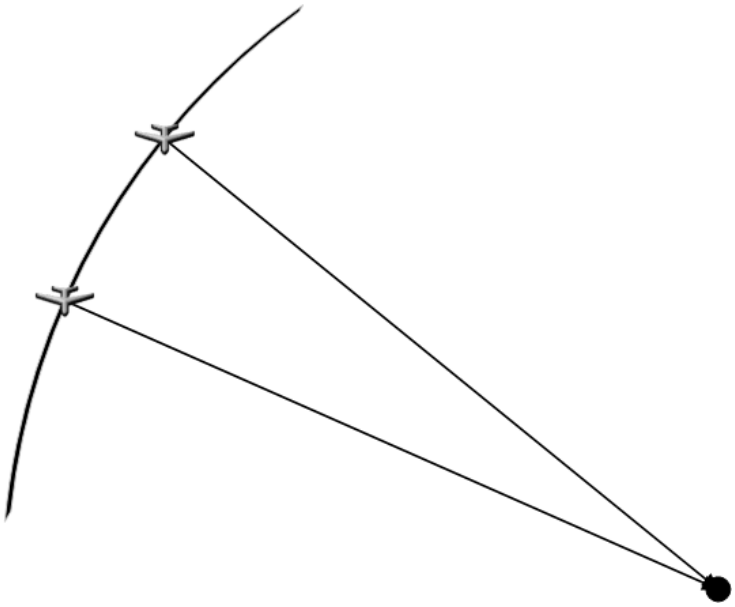

Fig. E.3: Illustration of how combinations of elevation and cross-track errors maintain constant slant range to a target.

there is an entire continuum of elevations at which a target can be imaged in focus. Focusing a target at the wrong elevation will cause a cross track shift in the target's location. This is illustrated in Figure E.4. This type of ambiguity becomes a problem when knowledge of the local terrain map is inaccurate. Therefore, errors in the DTED will result in targets shifted from their true positions.

The goal of the entire thesis is to perform GPS denied navigation using SAR imagery. In Chapter 4 an analysis is performed that explored the relationship of navigation errors to SAR imaging errors. That analysis is a stepping stone to inferring navigation errors from image errors. Another step for future research is to account for the ambiguities explained above. One potential method of resolving ambiguities in the presence of error is to account for multiple targets and track how errors effect each target differently. This may lead to successful navigation error inference using SAR imaging errors.

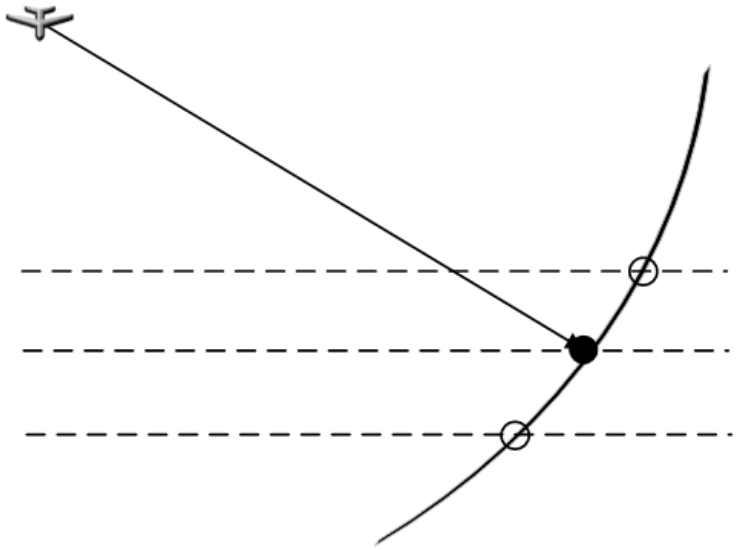

Fig. E.4: Illustration of how a single point target can be focused along a continuum of elevation and cross track locations.

APPENDIX F

Copyright Information

The papers comprising the main body of this thesis have been either published, submitted for publication, or are soon to be submitted for publication. They are therefore subject to special copyright statements, which are provided here in this appendix.

The IEEE does not require individuals working on a thesis to obtain a formal reuse license. In reference to IEEE copyrighted material, which is used with permission in this thesis, the IEEE does not endorse any of Utah State University's products or services. Internal or personal use of this material is permitted. If interested in reprinting/republishing IEEE copyrighted material for advertising or promotional purposes or for creating new collective works for resale or redistribution, please go to http://www.ieee.org/publications_standards/publications/rights/rights_link.html to learn how to obtain a License from RightsLink.

F.1 Published Works

F.2 Works Submitted for Publication

The following work has been submitted to the IEEE for possible publication. Copyright may be transferred without notice. After publication, the afore mentioned terms on reprinting and republishing of IEEE copyrighted material will apply.

C. Lindstrom, R. Christensen, and J. Gunther, "Sensitivity of BPA SAR Image Formation to Initial Position, Velocity, and Attitude Navigation Errors," *arXiv:2009.10210 [eess]*, Sept. 2020. arXiv: 2009.10210.

The material comprising Chapter 5 is currently under revision to be submitted for publication at a future date. Special copywrite permissions may apply.